THE UPGRADE, CALIBRATION AND EVALUATION OF THE MULTI-SLIT OSIRIS-DM FOR STRATOSPHERIC BALLOON FLIGHT

A Thesis Submitted to the College of

Graduate Studies and Research

In Partial Fulfillment of the Requirements

For the Degree of Master of Science

In the Department of Physics and Engineering Physics

University of Saskatchewan

Saskatoon, Saskatchewan

By

BARRETT J. A. TAYLOR

Permission to Use

In presenting this thesis in partial fulfilment of the requirements for a Postgraduate degree from the University of Saskatchewan, I agree that the Libraries of this University may make it freely available for inspection. I further agree that permission for copying of this thesis in any manner, in whole or in part, for scholarly purposes may be granted by the professor or professors who supervised my thesis work or, in their absence, by the Head of the Department or the Dean of the College in which my thesis work was done. It is understood that any copying or publication or use of this thesis or parts thereof for financial gain shall not be allowed without my written permission. It is also understood that due recognition shall be given to me and to the University of Saskatchewan in any scholarly use which may be made of any material in my thesis.

Requests for permission to copy or to make other use of material in this thesis in whole or part should be addressed to:

Head of the Department of Physics and Engineering Physics

116 Science Place

University of Saskatchewan

Saskatoon, Saskatchewan

Canada

S7N 5E2

ABSTRACT

The development of remote sensing satellite-borne instrumentation for the study of the Earth's atmosphere has provided an immense increase in our understanding of atmospheric trends and processes. The Canadian built OSIRIS satellite instrument uses the limb scatter technique to measure scattered sunlight for the retrieval of vertical profiles of atmospheric species such as ozone. Recently, the next generation instrument, CATS, based on the OSIRIS design, is under development to continue OSIRIS measurements into the future. One key optical design change for CATS is the ability to measure simultaneously over multiple fields of view. However, this new optical design concept needs to be tested and evaluated. To achieve this, a prototype slit plate was installed into the preflight developmental version of OSIRIS, called OSIRIS-DM, for testing in the laboratory and on a stratospheric balloon.

In this thesis work, an evaluation of the performance of this multi-slit instrument was undertaken through laboratory calibrations and limb scatter measurement collection. The calibration process includes a wavelength registration, a spectral point spread function analysis, a relative calibration and an absolute calibration, all performed with laboratory equipment.

Along with laboratory calibrations, this thesis work involved preparation for the stratospheric balloon mission including the development of a flight ready electronic control and communication system to operate OSIRIS-DM during the mission. The upgraded instrument was launched on September 19, 2014, and ascended to a stable float altitude of 36.5 km. The collected flight measurements were used to evaluate the calibrations and general instrument performance. Overall, the laboratory calibrations proved to be sufficiently accurate and the measurement collection produced multiple spectra that may be used for atmospheric analysis in the future. These results show that the multi-slit design of the slit plate produces an instrument that can be reliably calibrated and implemented for limb scatter measurement collection.

ACKNOWLEDGMENTS

This work was made possible by the Canadian Space Agency and the Flights for the Advancement of Scientific Technology program by providing funding and the opportunity to participate in the stratospheric balloon mission in collaboration with the Centre National d'Etudes Spatiales. It was also financially supported by the University of Saskatchewan and the Institute of Space and Atmospheric Studies.

Special thanks must be given to Dr. Nick Lloyd for all of his guidance and insights before and during the balloon campaign. The combination of his knowledge, experience, and tireless willingness to help, proved to be invaluable and irreplaceable countless times throughout the project. Special thanks must also be given to Paul Loewen for all of his contributions that were received on an almost daily basis. His calm and reassuring demeanor was always appreciated and proved to be immensely helpful in stressful times and situations.

To my coworker, and friend, Matt Kozun, who I worked with every day, goes a momentous thank you. His work ethic and relaxed attitude was always appreciated during the days that we worked close together on certain project elements and his willingness to aid my work with hands on help in the laboratory or with daily conversations and contemplations was never, and will never be, overlooked or taken for granted.

My deepest gratitude is reserved for my supervisors, Drs. Adam Bourassa and Doug Degenstein, who were never too busy to lend a hand with any issue that I encountered. They provided me with every opportunity that I could have imagined in this project and facilitated the learning and understanding that I have gained through this project. These two continually inspired confidence in my work and I feel I have achieved more than I thought possible due to their contributions.

Finally, thank you to my family, especially my parents, and friends, for their unwavering support and belief in my abilities.

To my parents,
Gordon and Diane Taylor
And
To Danielle

TABLE OF CONTENTS

page

LIST OF TABLES

LIST OF FIGURES

LIST OF ABBREVIATIONS

ADC	Analog to Digital Converter
CATS	Canadian Atmospheric Tomography System
CCD	Charge-Coupled Device
CNES	Centre National d'Etudes Spatiales
CRC	Cyclic Redundancy Check
CSA	Canadian Space Agency
DA	Data Available
DN	Digital Number
DM	Developmental Model
DMA	Direct Memory Access
FAST	Flights for the Advancement of Science and Technology
FIFO	First In First Out
FM	Flight Model
FOP	Field-flattener, Order-sorter filter and Prism element
FPGA	Field Programmable Gate Array
GOMOS	Global Ozone Monitoring by Occultation of Stars
GPIO	General Purpose Input Output
GSE	Ground Support Equipment
HWHM	Half Width at Half Maximum
ISA	Industry Standard Architecture
MOS	Metal-Oxide Semiconductor
MOSFET	Metal-Oxide Semiconductor Field-Effect Transistor
NASA	National Aeronautics and Space Administration
NIST	National Institute of Standards and Technology
OSIRIS	Optical Spectrograph and InfraRed Imaging System
PSF	Point Spread Function
ROE	ReadOut Electronics
SAGE	Stratospheric Aerosol and Gas Experiments
SPI	Serial Peripheral Interface
SSI	Synchronous Serial Interface
SUMIT	Stackable Unified Module Interconnect Technology
TOMS	Total Ozone Mapping Spectrometer
USB	Universal Serial Bus
UV	UltraViolet

CHAPTER 1
INTRODUCTION

The emergence of satellite based remote sensing instruments to collect measurements to study the Earth's atmosphere has provided an unprecedented increase in our knowledge of the atmosphere. These instruments implement a variety of techniques with the common goal of collecting atmospheric measurements that can be analyzed to determine the concentrations of atmospheric species. By creating long term data sets of atmospheric concentrations, information on atmospheric processes, effects on weather and climate, and anthropogenic impact on the atmosphere can all be studied. Even with this expansion of knowledge, our understanding of the atmosphere is not yet complete and continues to grow every day. The Optical Spectrograph and InfraRed Imaging System (OSIRIS) instrument has been, and continues to be, one of these satellite instruments used to collect measurements to aid our understanding. OSIRIS uses the limb scatter technique to measure vertical profiles of scattered sunlight spectra that are used to retrieve profiles of various atmospheric species like ozone, aerosols and nitrogen dioxide. The most popular data products of OSIRIS are ozone and aerosol concentrations.

With the growing need and desire for more and more information, the next generation of instruments is approaching. Due to the success of the OSIRIS mission, a next generation instrument, the Canadian Atmospheric Tomography System (CATS) (*Sioris et al.*, 2014), is under development to continue the OSIRIS legacy. The CATS instrument is based on the OSIRIS instrument design with a few key modifications. One of these modifications is the change in the optical design from a single line of sight instrument to a multiple line of sight instrument with the addition of multiple slits to the instrument slit plate.

Before full implementation of this new slit plate design for a space application, it needs to be tested and evaluated with regard to its effects on the calibration process and instrument

performance. This is the overarching goal of this thesis work. The proposed method for this evaluation is to install a slit plate with the new multi-slit design into the OSIRIS Developmental Model (DM). The DM was built as a precursor to the Flight Model (FM) in the late 1990's as a proof-of-concept engineering model. It is a near exact replica of the FM containing many duplicate components and is now housed in the atmospheric optics laboratory at the University of Saskatchewan. In order to investigate the effects of the new design on calibration and performance, the DM was calibrated using laboratory based experiments and techniques. It was then used to collect atmospheric measurements on board a stratospheric balloon. The calibrations and measurements were then used together to evaluate performance with comparisons to simulated atmospheric spectra using a radiative transfer model known as SASKTRAN. In the future, the balloon data may be used for scientific retrieval of atmospheric species concentration, but this is beyond the scope of the current work.

This thesis work progressed in several stages. In preparation for the balloon flight, the DM was required to undergo an electronic control system upgrade. This involved a full characterization of the original control system including reverse engineering many of the signals and communication protocols. Once the system was completely diagnosed and understood, an evaluation of components that could be flown on a balloon and components that needed replacing was conducted. This resulted in the need for a new power source that could interface to the gondola power system, a new flight computer, and a new set of interface electronics to interface the flight computer and the DM. Along with this electronic upgrade, a new front end optical system, designed and built by *Kozun* (2015), was installed on the front of the DM. This system consists of a front end baffle, a scan mirror, and a shutter system. The purpose of this system is to allow for measurements over a range of tangent altitudes while on the balloon.

Chapter Two of the thesis provides background information on stratospheric remote sensing, the OSIRIS and CATS instruments, facilitating and support programs for this project, and a radiative transfer model, SASKTRAN, used to simulate atmospheric measurements for comparison with balloon measurements. Chapter Two also contains a description of the OSIRIS instrument including the electronics system, the Charge-Coupled Device (CCD) detector, and the optical system as well as a brief introduction to the calibrations that will be performed on the upgraded DM. This chapter concludes with an overview of the upgrade process. Then, in Chapter Three, a detailed description of the electronics and communication system is presented. This chapter includes an introduction to the original DM control system, upgrade requirements, communication protocols, hardware solutions, communication protocol implementation solutions, and software solutions, as well as a description of issues encountered along the path to a fully upgraded and operational system. Chapter Four presents the details of the preflight calibrations performed throughout the optical system upgrade process. This includes a dark current and DC offset removal process, characterization of the image slit(s), wavelength registration, spectral Point Spread Function (PSF) analysis, relative calibration, absolute calibration, and a thermal analysis. Chapter Five details the balloon flight and the instrument performance during the mission along with evaluations of the preflight calibrations. In this chapter, a DC offset removal method and a dark current removal method is applied to flight measurements, the wavelength and PSF calibrations are evaluated by comparisons with a known solar spectrum with its associated Fraunhofer features, and the relative and absolute calibrations are applied to balloon measurements to be evaluated with comparison to SASKTRAN simulated spectra. Finally, Chapter Six provides a summary of the work presented and discusses potential future work and recommendations for the CATS instrument design and calibration process.

CHAPTER 2
BACKGROUND

2.1 Stratospheric Remote Sensing

Stratospheric remote sensing generally refers to a set of techniques employed by a variety of instruments to collect measurements of the Earth's atmosphere with a variety of viewing geometries. Three primary optical stratospheric remote sensing techniques are occultation, nadir mapping, and limb scattering.

The occultation technique requires the instrument to view a celestial body such as the sun, moon, or a star, through the atmosphere and track it throughout the orbit of the instrument. As the image object rises and sets throughout the orbit, the instrument is able to record images through various altitudes and thicknesses of atmosphere thus developing an altitude profile of measurements. At the peak height of the object in relation to the instrument, the instrument is able to measure the incoming light outside of the atmosphere. This provides a measure of the unattenuated light of the object. To perform analysis on the observations, the unattenuated light is used as a reference measurement to determine the amount of absorption that occurred at varying altitudes which in turn is used to measure atmospheric species concentration. Solar occultation was implemented by the productive, and highly successful, National Aeronautics and Space Administration (NASA) Stratospheric Aerosol and Gas Experiments (SAGE) I and II (*McCormick et al.*, 1989). Due to the success of these instruments, they were followed by SAGE III (*Thomason and Taha*, 2003) and a further follow up is proposed to have a SAGE III instrument on the International Space Station (*SAGE III on ISS*, 2014). Stellar occultation was implemented by the Global Ozone Monitoring by Occultation of Stars (GOMOS) instrument (*Nett et al.*, 2001) that was launched on board the European satellite Envisat in 2002.

The nadir mapping technique is often used to measure the total ozone column. This technique uses a nadir, or downward looking, viewing geometry to measure the intensity of two different wavelengths; one wavelength that is strongly absorbed by ozone and one that is weakly absorbed. The measurement acquired from the weakly absorbed wavelength is the reference measurement as it provides a signal that is assumed to be unaltered by ozone absorption. The two measurements are used to develop a ratio that can be used to determine the total ozone column. This technique is used by the Total Ozone Mapping Spectrometer (TOMS) instrument (*Krueger et al.*, 1995).

The limb scattering technique is the technique used by the OSIRIS instrument (*Llewellyn et al.*, 2004). Limb scattering uses measurements acquired by observing the limb of the atmosphere to measure scattered sunlight. It is similar to the occultation technique except that it does not look directly at the sun. Instead, it uses an indirect measurement of the incoming sunlight by viewing the limb at an angle away from the sun to measure scattered sunlight. These measurements are analyzed to determine absorption from ozone and other atmospheric species. The analysis involves a comparison of measured light intensities at various wavelengths to a known solar spectrum and a radiative transfer model that can characterize the light path in order to determine how much light was absorbed by the different atmospheric species.

2.2 OSIRIS, CATS, and the FAST Program

The OSIRIS instrument was launched in February of 2001 on board the Odin satellite (*Murtagh et al.*, 2002) to collect measurements of the Earth's atmosphere used to determine atmospheric species concentrations specifically in the stratosphere and mesosphere (*Llewellyn et al.*, 2004). As previously mentioned, OSIRIS uses the limb scattering technique. OSIRIS uses a single line of sight to acquire spectra of the limb at varying tangent altitudes, one tangent altitude at a time. In order to measure varying altitudes, the Odin satellite nods up and down as it orbits the Earth

which makes the OSIRIS line of sight scan the atmosphere from approximately 10 to 100 km (*Llewellyn et al.*, 2004). Inside the instrument, between two matched parabolic mirrors, is a small rectangular slit that defines the field of view of the instrument and thus defines the tangent altitude being observed at any given time. Figure 2.1 illustrates the limb scattering viewing geometry of the satellite instrument.

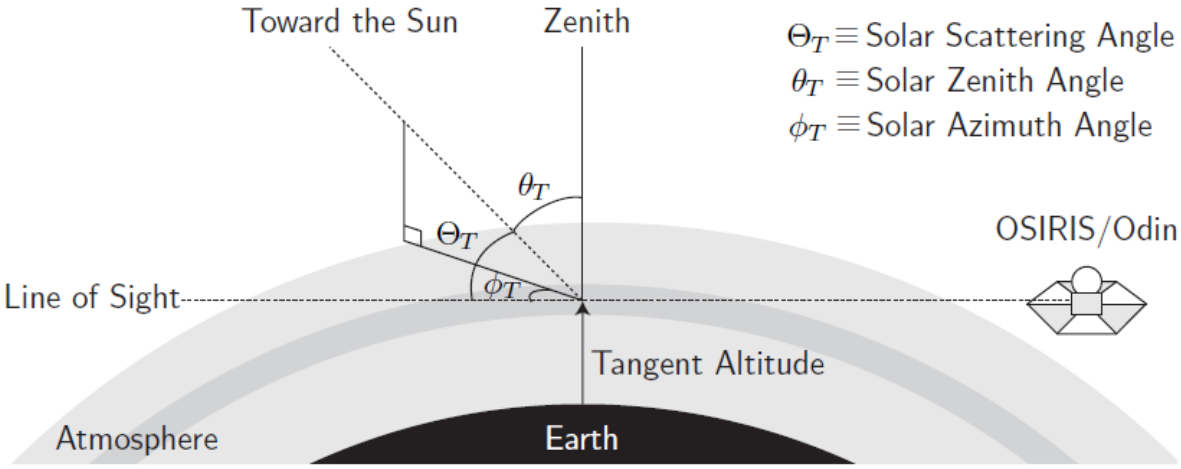

Figure 2.1: Limb scattering viewing geometry of the OSIRIS instrument on Odin. Image obtained from *Bourassa et al.* (2008).

The measured light originates from the sun, scatters from atmospheric species and into the line of sight of OSIRIS. Note that many scattering events can occur before scattering into the instrument line of sight. The OSIRIS measurements are used to retrieve atmospheric species concentrations, such as ozone density, using a method developed by *Degenstein et al.* (2009). Due to the general concern of the depleting ozone layer due to pollution such as chlorofluorocarbons (*Solomon*, 1999), the long term OSIRIS ozone data set has been widely used by researchers to examine trends and changes in the ozone layer. Most recently, the results of OSIRIS have been used together with SAGE results to report a recovery of the ozone layer (*Bourassa et al.*, 2014).

The OSIRIS-DM was built as a proof-of-concept engineering model to be used for testing and development of the FM (*Warshaw et al.*, 1996). In the early 2000s, the DM was set up in a laboratory at the University of Saskatchewan along with a ReadOut Electronics (ROE) module and a host computer referred to as the Ground Support Equipment (GSE). This configuration was used to acquire ground based measurements of the atmosphere to serve as validation of the satellite measurements (*Wilcox*, 2002) and later for automated measurement collection (*Stoicescu*, 2006).

Recently, a follow-on instrument to OSIRIS has been under study by the Canadian Space Agency (CSA) and the Canadian academic community. The CATS instrument is based on the design of OSIRIS with some key modifications. One of these modifications is changing the slit plate from a single slit design to a multi-slit design. This will allow multiple tangent altitudes to be measured simultaneously, which will allow for a higher density of measurements and enable a tomographic inversion (*Degenstein et al.*, 2003).

Testing of the multi-slit design is a critical step in the readiness of CATS for space. In this thesis work, an evaluation of the multi-slit concept is performed using an upgraded OSIRIS-DM on a stratospheric balloon. This included an upgrade on control electronics of the DM as well as a full calibration of the instrument with the new slit plate. In order to achieve this goal, funding and support was obtained from the CSA Flights for the Advancement of Science and Technology (FAST) program. Apart from financial support, this program provided the opportunity to put the upgraded DM system on a stratospheric balloon as a demonstration to simulate the operating conditions of low earth orbit and allow limb scatter measurements to be acquired. The instrument was launched on board the CARMEN gondola from the CSA balloon launch facility in Timmins, Ontario in collaboration with the French space agency, Centre

National d'Etudes Spatiales (CNES). After completion of the balloon mission, the measurements were analyzed to evaluate the performance of the multi-slit design and to provide recommendations for the future CATS instrument.

2.3 SASKTRAN – A Radiative Transfer Model

The analysis of collected measurements using the limb scattering technique requires the implementation of a radiative transfer model. Over the years, radiative transfer models have evolved as necessary to facilitate the analysis of different measurement techniques. One such radiative transfer model was developed at the University of Saskatchewan for implementation specific to OSIRIS measurements. This model is known as SASKTRAN and was developed by *Bourassa et al.* (2008). SASKTRAN is a fully spherical, successive orders, radiative transfer model developed for the specific reason of modelling limb scattered measurements. This model is used along with atmospheric limb measurements in a non-linear inversion to determine the concentrations of atmospheric species. Although SASKTRAN has some systematic error, it has been compared against other radiative transfer models (*Bourassa et al.*, 2008) and the result is an agreement level that verifies the model to the point that it has become a widely accepted and implemented tool in the field of radiative transfer.

SASKTRAN requires basic state parameters, such as a known solar spectrum, sun position, instrument viewing geometry, atmospheric parameters, particle scattering parameters and an initial assumption of the atmospheric state to name a few. The model begins with the radiative transfer equation in integral form. The following equation and description was taken from *Bourassa et al.* (2008).

$$I(\vec{r_0}, \hat{\Omega}) = \int_{s_1}^{0} J(s, \hat{\Omega}) e^{-\tau(s,0)} ds + \tilde{I}(s_1, \hat{\Omega}) e^{-\tau(s_1,0)} \tag{2.1}$$

This states mathematically that the radiance, *I*, observed at a location, $\overrightarrow{r_0}$, in the propagation direction specified by the unit vector $\hat{\Omega}$, along the straight line path, *s*, is the integral sum of the scattered source term, *J*, along the path attenuated to the observer plus the radiance at the end of the path, $\tilde{I}$, also appropriately attenuated back to the observer. $\tau(s_2, s_1)$ is the optical depth from $s = s_2$ to $s = s_1$. In this formulation, the path coordinate, *s*, is zero at observer position, $\overrightarrow{r_0}$, and requires s_1 to be negative at the path end point. The source term from scattering is

$$J(s, \hat{\Omega}) = k_{scat}(s) \int_{4\pi} I(s, \hat{\Omega}') \vec{p}(s, \Theta) d\Omega' \tag{2.1}$$

where k_{scat} is the extinction due to scattering processes only, $\vec{p}$ is the scattering phase function and Θ is the angle between the incoming direction $\hat{\Omega}'$ and the outgoing direction $\hat{\Omega}$.

The SASKTRAN model takes these equations and applies them multiple times in successive orders to calculate the radiance observed by the instrument or observer. The simple version of SASKTRAN is to model only single scattering events. In this case, light from the sun interacts with a single particle in the atmosphere and is scattered into the instrument line of sight. This process does contribute to the full limb radiance but other terms are also significant. These are signal contributions from multiple scattering events. In this case, light comes from the sun, is scattered from one particle and is then scattered from multiple successive particles, or the ground, before reaching the instrument detector. Multiple scattering events can occur many times. Modelling all possible multiple scattering events is obviously impossible. Generally, multiple scattering up to an order of 30 interactions is sufficient. Every time that a scattering event occurs, the contribution of that specific light to the overall measured signal decreases. This is because every scattering event causes a change in the energy of the incoming radiation by redistributing it in all directions at varying magnitudes depending on the encountered particle. The other effect that a particle can have on the incoming radiation is that it can absorb some of

the energy, again, depending on the particle. Therefore, the energy of the light leaving the scattering event in any one direction will be less than the energy that went into the interaction.

In order to model all of these interactions, Equation 2.1 is implemented with the incoming solar spectrum to determine the radiance produced from a single scattering event. This event creates illumination in all directions that is dependent on the type of particles encountered. Therefore, a varying portion of the incoming radiation is scattered outward in all directions from this first interaction. This outgoing radiation may travel directly into the instrument or it may encounter another particle along the way. If it is scattered again, Equation 2.1 is applied again with the incoming radiation that was calculated as the outgoing radiation from the first scattering event. Again, radiation is scattered in all directions at varying magnitudes. This method of successive application of the radiative transfer equation happens over and over again until the desired scattering order level is reached. The desired level is dependent on the user and specific application. The model then calculates a radiance spectrum based on contributions from all radiation that reaches the instrument detector and produces a final answer for expected radiance.

SASKTRAN is used along with measurements from the OSIRIS instrument to calculate the concentration of atmospheric species by comparing the above described simulated spectra with measured spectra. By changing atmospheric state parameters in SASKTRAN, the best fit of a simulated spectrum to a measured spectrum is determined. The concentrations of atmospheric species that were used to determine this best fit become the resultant retrieved atmospheric concentrations at the given position, look direction, etc. In the current work, SASKTRAN will be used to produce simulated radiance spectra to compare to the calibrated balloon measurements acquired with the upgraded OSIRIS-DM. This will provide a way to evaluate the performance of

all of the instrument calibrations as well as the performance of the multi-slit instrument during flight.

2.4 OSIRIS Instrument Description

2.4.1 General Description

The OSIRIS-FM and OSIRIS-DM instruments are both spectrometers that use a CCD detector along with a grating and optical system to measure the intensities of spectrally dispersed light. They also both use similar electronic interfaces to convert and store the accumulated signal measurement. The DM was built as a fully functional proof-of-concept engineering model. The intended use of the DM was to demonstrate the proposed satellite instrument through ground based measurements and hardware demonstration of the optical and electronics systems. Once the FM was put into orbit, the DM was used to collect ground based measurements that could be used to validate the flight measurements. Due to the fact that both instruments are essentially copies of each other, their operation is also almost identical. Now, fourteen years into the flight mission of OSIRIS, much of the knowledge gained from the satellite mission can be used to understand the DM and its operation.

2.4.2 Electronics System

The electronics system is comprised of three primary modules – the GSE, or control computer, the ROE, or communication module, and the CCD detector. The primary function of the GSE is to be the interface to the ROE and thus the DM itself. This begins with the GSE defining the image acquisition parameters which includes the operation mode and exposure time. The exposure time is the parameter that defines how long the CCD is exposed to incoming light. The GSE then sends these commands to the DM and waits for the return of a full image. Once a full image is received back from the ROE, the GSE stores the information for later processing or analysis. The second module is the ROE or communication module. The function of this module

is to communicate between the GSE and the detector and back again. To do this, it must take inputs from both sides and convert these to the output formats that each side requires. This entails taking the initiation commands from the GSE and sending them to the CCD, reading out the image data from the CCD, and finally converting this data into a format that can be read and stored by the GSE. The ROE is a single circuit board with two primary components. The first is a Field Programmable Gate Array (FPGA) that is the central processing unit of the board. The job of the FPGA is to read in and send out data to the different components on the board. The second primary component is the Analog to Digital Converter (ADC). This component is used to read the accumulated charge from the CCD. It generates values for each of the CCD pixels as a Digital Number (DN) that can be sent to the computer and stored. DN is a representation of the number of photons that are measured by the CCD. The final component is the CCD and the electronics that operate it. The job of this module is to take the commands from the GSE, program the CCD for the required exposure, and start the exposure. Once the exposure is complete, the electronics must readout the rows of the CCD and send the data to the ROE for processing.

2.4.3 The Charge-Coupled Device

The information on general CCD operation presented in this section is taken from a combination of *Janesick* (2001), *Holst* (1998) and *Lamb et al.* (1980). A CCD is an imaging device used to measure the intensity of light in a given amount of time by recording the number of photons that interact with the CCD surface during that time. The surface of a CCD is made up of many tiny squares called pixels that are arranged in columns and rows to create a larger square, or rectangular, array. Pixels are usually p-doped Metal-Oxide Semiconductor (MOS) capacitors and are primarily silicon based. These capacitors not only store the accumulated charge but also create the generation of charge by interacting with incoming photons. To achieve this, the gate of

the MOS, or pixel, is held at a positive biased potential that is above the threshold voltage. This creates a bias in the depletion region which causes the creation of an inversion layer at the semiconductor-oxide interface where an n-channel can form like in a Metal-Oxide Semiconductor Field-Effect Transistor (MOSFET). Due to the initial positive voltage applied at the gate, the holes are pushed into the substrate leaving no mobile electrons at the surface causing the CCD to operate in the non-equilibrium deep depletion state. When electron-hole pairs are generated by incoming photon collisions, they are separated by the electric field created by the positive gate voltage. This causes the holes to go into the substrate and causes the electrons to rise up to the surface (towards the positive gate) thus creating measureable surface charge. This enables the interaction of a single photon with a pixel to excite an electron from the valence band into the conduction band due to the energy transfer from the incoming photon to the MOS substrate. This excited electron can then be stored in the capacitor as electrical charge and recorded as one count. This setup allows for a direct one-to-one ratio of accumulated charge to incoming photons to be measured in an ideal system. However, a perfectly ideal CCD does not exist as all CCDs have a characteristic called quantum efficiency. Quantum efficiency describes the rate at which incoming photons generate charge, i.e. the number of photon interactions that are required to generate one count of charge. An ideal CCD would have a quantum efficiency of 1 but all real CCDs have a value that is less than 1. This means that not all photon-pixel interactions will result in the generation of countable charge. Quantum efficiency is also dependent on wavelength and is therefore different for all pixels. This effect is accounted for in the relative calibration which is covered in Section 4.5.

Apart from electron-hole pair generation due to an incoming photon interaction, there are three other ways that electron-hole pairs can be generated. These three methods are generation in

the depletion region, generation at the surface, and generation in the neutral bulk of the MOS. All three of these methods contribute to what is called dark current generation because they do not require an incoming photon to occur. Because they do not measure incoming photons, these processes are unwanted and add noise to the measured signal. These processes are caused by thermal energy exciting electrons in the different regions causing them to become free electrons and travel towards the positive gate and into the n-channel which generates additional signal. Dark current signal is always present in images and has to be calibrated out to permit proper analysis of measurements. This is achieved with a dark current removal method as described in Sections 4.1 and 5.1.

At the end of the imaging process, the charge that was accumulated in each pixel needs to be read out to external electronics. In order for this to occur, each row of the CCD needs to be shifted down vertically through the CCD and into the readout row. This shifting process through the CCD is achievable because each pixel can act as a capacitive bin and the accumulated surface electrons can be manipulated by the shift register operation of the CCD. This process is performed by control circuits manipulating the voltages applied to the gates of the pixels and forcing the accumulated electron charge to move to the next bin because of the higher positive voltage applied. Therefore, the shifting process is to shift the bottom row vertically down one row to free up its original row and then the rest of the rows above it shift down in a similar matter. When a row of charge enters the readout row, it is shifted out horizontally. This shift sends each pixel to an external ADC where the accumulated charge is converted to a voltage and recorded as a DN. This process of vertically shifting the rows down by one followed by a horizontal shifting of the pixels out of the readout row repeats until all rows have been shifted into, and out of, the readout row.

The OSIRIS instrument uses an EEV Model CCD26 CCD with a frame transfer architecture whose active area pixels are arranged into 286 rows and 1353 columns. In this type of CCD, half of the active area (the area comprised of pixels that can generate and hold charge) of the CCD is exposed to the incoming light while the other half of the active area is masked and used as a storage area. Therefore, the active imaging area and storage area are each 143 rows by 1353 columns. This creates two areas identified as the image area and the storage area respectively. Figure 2.2 shows a diagram of the CCD structure along with a block diagram of the components involved in the readout operation.

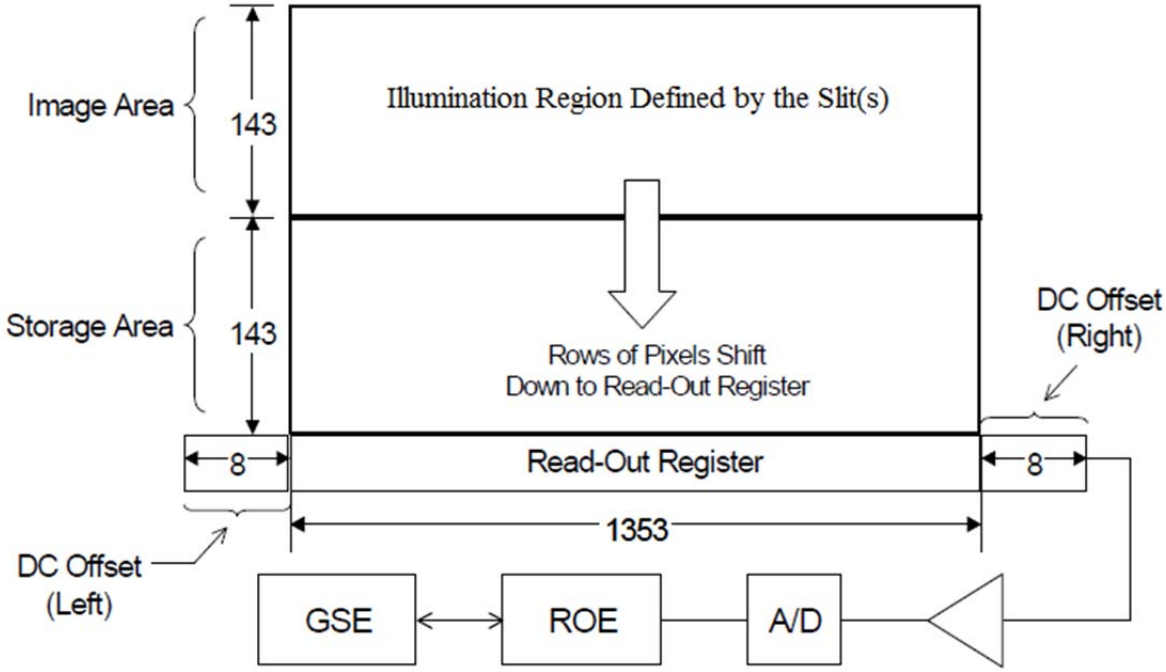

Figure 2.2: CCD architecture illustrating the two primary pixel areas (image area and storage area), the readout row, the DC offset pixels, and the readout chain. Image adapted from *Wilcox* (2002).

This figure shows the two different regions of the CCD (image area and storage area) as well as the DC offset that is measured by the first and last eight pixels of the readout row. The DC offset voltage is a voltage applied to the pixels as they are read out and before they are sent to the

ADC. This occurs in the DM to ensure proper operation of the ADC. The DC offset pixels are there to measure the amount of DC offset voltage applied to the readout row to allow for removal of the offset from the final data product as this is unwanted signal. They contain a reading of only the DC offset because they are continuously flushed until readout and are never exposed to illumination as they are masked. Therefore they do not accumulate any photo-charge or dark current during image acquisition or during the shift to the storage area. However, they can accumulate a small amount of dark current during the readout of the readout register as this takes a finite amount of time where these pixels do not get flushed.

In the frame transfer architecture, the entire CCD is continuously flushed while an image is not being acquired to eliminate any dark current that would otherwise be accumulated in between image acquisitions. This ensures that when an image is acquired, all of the CCD pixels will start with a count of 0. Once an image is acquired, the entire top half of the CCD is quickly shifted down into the storage area to wait to be shifted into the readout row. This is done to limit the time that the imaged rows remain in the image area and thus limit the amount of smearing incurred on the image. Smearing is a term used to describe the signal across the CCD that is generated by incoming light after the defined exposure time is complete while the rows are being moved through the image area. This provides undesired signal that increases in significance the longer it takes the CCD to move these rows through this area. Therefore, if all the rows are shifted to a storage area quickly without having to wait for readout in the image area, the amount of smearing signal is reduced. The accumulated charge then sits in the storage region and is allowed to accumulate dark current contributions while waiting to be read out. However, this contribution is significantly less than the contamination that would be encountered if the charge

had to stay in the image area during readout and is easily characterized and removed with a dark current calibration as will be explained in Section 5.1.

2.4.4 Optical System Description

The optical design of the OSIRIS instrument is based on a primarily reflective folded optics design. A schematic of the instrument is shown in Figure 2.3. Further details of the design can be found in *Warshaw et al.*, 1996.

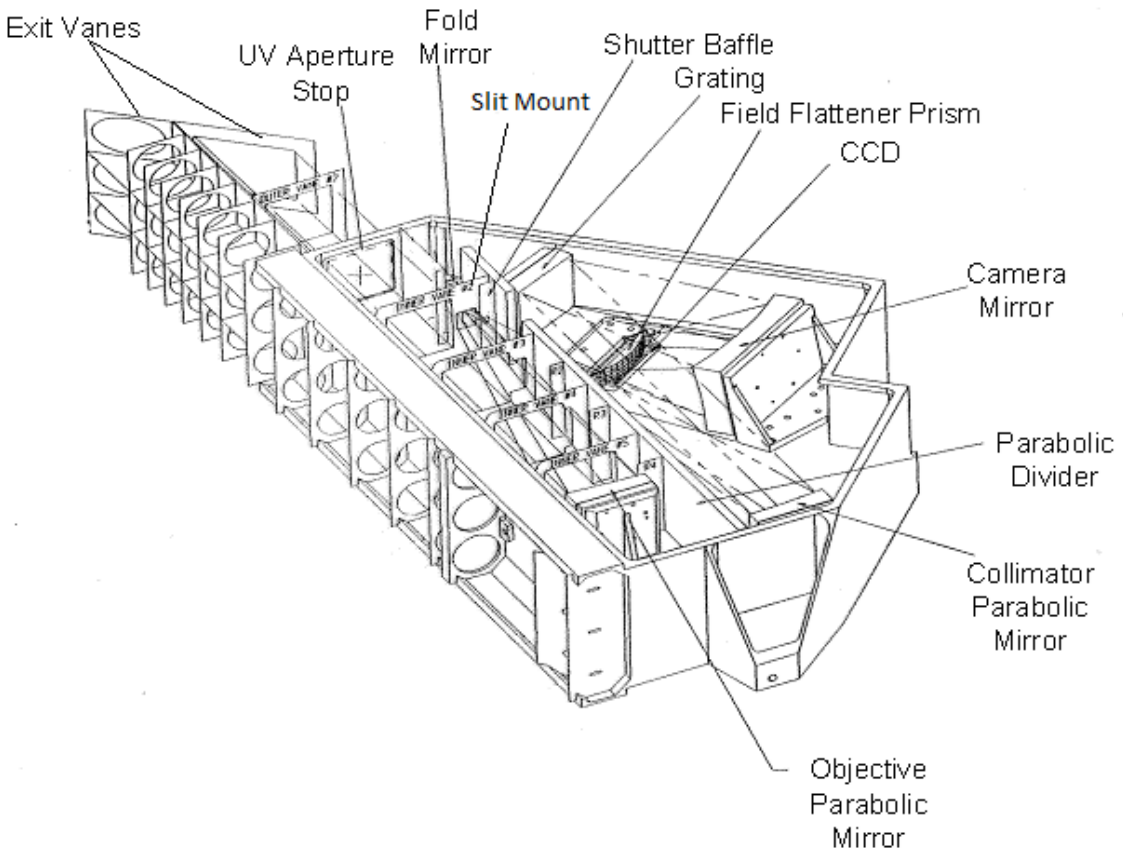

Figure 2.3: Schematic of the OSIRIS-DM instrument illustrating the primary optical elements contained in the optical chain. Image adapted from *Llewellyn et al.* (2004).

The following is a description of the UltraViolet (UV)/visible spectrograph and not the infrared imager channels as they are not used in this work. Light first enters the system through a 36x36 mm square aperture, labelled exit vanes, with truncated corners. This light is incident on

an off-axis parabolic objective mirror that reflects the light onto a flat folding mirror. Next, the light strikes the slit plate which is placed at the mirror focus. After passing through the slit, the light is incident on a second off-axis parabolic mirror that collimates the light and illuminates a blazed aspheric reflective grating. The grating spectrally disperses the light and projects the first and higher order diffracted light onto a spherical camera mirror that reflects the light onto a combination Field-flattener, Order-sorter filter, and Prism element (FOP). Finally, the dispersed light is imaged onto the CCD with an image area of 143x1353 pixels. The FOP is placed directly in front of the CCD to increase optical performance and to filter out light from second and higher order maxima of the diffraction grating thus not allowing this light to interact with the CCD and be measured. This is required due to the large spectral range measured by the CCD. When short wavelength light is diffracted, the second order maxima are projected onto CCD pixels corresponding to longer wavelength first order maxima. Therefore, this higher order shorter wavelength light is blocked by the FOP. This is achieved by physically contacting a filter onto the FOP for wavelengths starting at around 550 nm. This filters out all light that has a wavelength less than 550nm.

The CCD is illuminated in such a way that the 143 row pixels in every column map to the horizontal field of view of the instrument and 1353 column pixels in every row map to the dispersion, or spectral, dimension. Therefore, every one of the 1353 column pixels corresponds to a specific wavelength range. The final result is a spectrally dispersed image of the illuminated slit on the CCD. An example of the resultant image of a Tungsten bulb is shown in Figure 2.4.

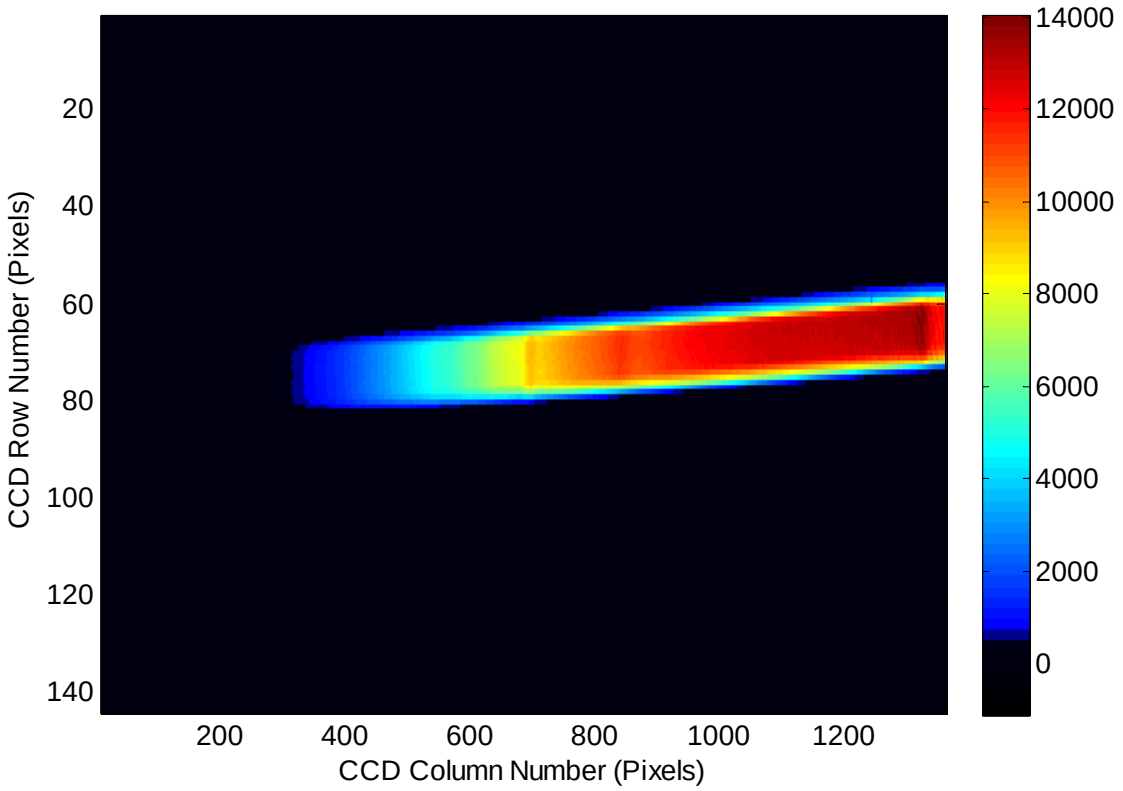

Figure 2.4: CCD image of a Tungsten bulb with the single slit system. Background is not constant but is blacked out below 80 counts to highlight the illuminated slit. These counts are negligible in comparison to the overall strength of the illuminated pixels.

In October of 2013, the OSIRIS-DM instrument was delivered to an engineering firm in Ottawa, called COM DEV, to replace the existing slit plate containing one slit with a new slit plate containing multiple slits. Details of the new multi-slit design and installation can be found in *Kozun* (2015). The addition of the new slit plate does not change any of the other optics as previously described. The resulting image now contains three spectra, one corresponding to each slit, as shown in Figure 2.5.

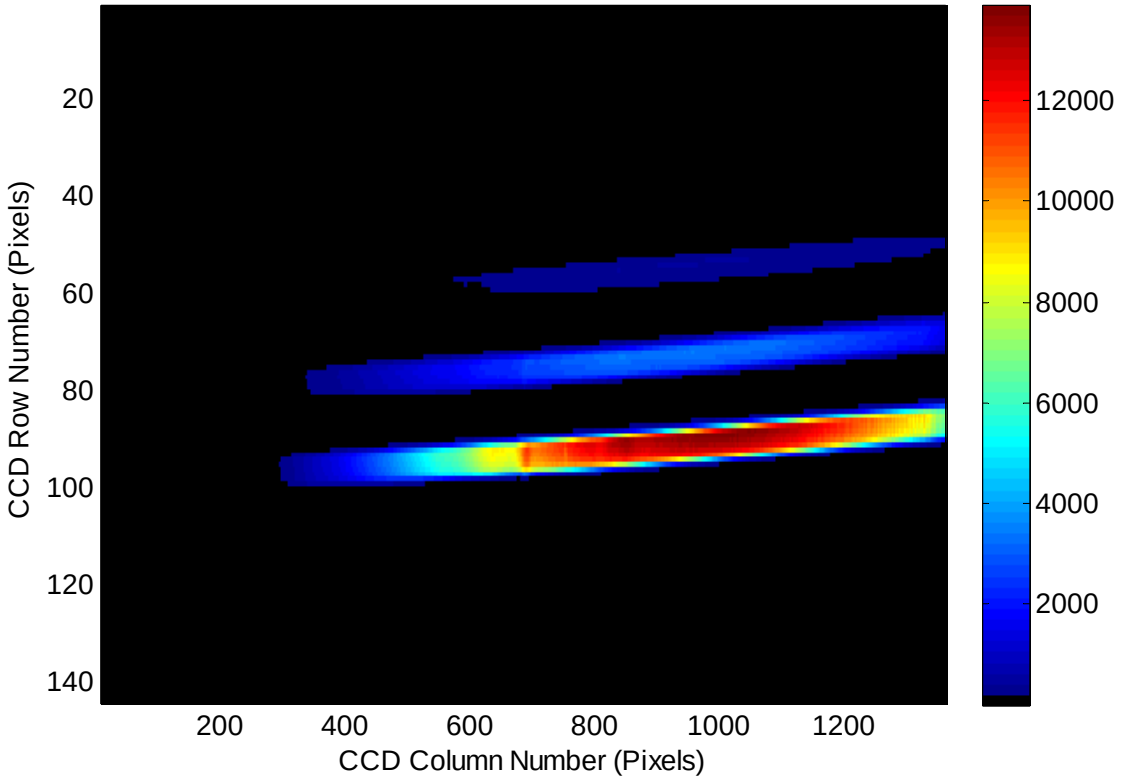

Figure 2.5: CCD image of a Tungsten bulb with the multi-slit system. Background is blacked out below 80 counts to highlight the existence of the three slits. These counts are negligible in comparison to the overall strength of the illuminated pixels.

The top slit in this image appears much dimmer than the other two because of the low number of photons measured due to the small size of the slit. This image also displays the relative sizing of the three slits: there is a big slit, a small slit and a medium sized, or middle, slit. The three slits are sized differently to account for the different radiance magnitude that each will measure in the atmosphere from a satellite platform. The big slit will view the highest altitude and thus the lowest signal and the small slit will view the lowest altitude and thus the highest signal. Therefore, the different slit sizes are an attempt to make the measured counts on the CCD equal for all three slits. The background is not a constant value of zero but has been blacked out below 80 counts to highlight the existence of the three slits, their positioning and relative strengths.

2.5 Introduction to Required Calibrations

Part of the evaluation process of the new multi-slit design is the calibration of the multi-slit instrument. A performance evaluation is achieved by performing calibrations and evaluating their performance with laboratory verification tests and atmospheric measurement verification. A brief outline of the calibrations performed on the DM is presented here, a detailed description of theory and application is presented in Chapter Four, and results are presented in Chapter Five.

2.5.1 Dark Current Calibration Introduction

Dark current is the term used to describe the constant generation of electrical signal in the absence of light that is found in all CCDs. It is created by thermal and vibrational energy in the silicon lattice structure of each pixel (semiconductor) that can supply enough energy to a valence electron to excite it into the conduction band. Once in the conduction band, the electron is drawn towards the positive gate and the n-channel region where it supplies measured signal. Therefore, the amount of dark current generated in an image is highly dependent on temperature. The measured count generated by dark current is a combination of the actual amount of dark current generated and the associated noise or error generated. The error portion of the measurement is random error and follows a Poisson distribution making the contribution equal to the square root of the counts. Therefore, as the amount of dark current generated increases, so does the noise, or error, in the measurement. Obviously, dark current is unwanted signal as it is not generated by the incoming light which is the desired signal to be measured. Therefore, a calibration technique for how to remove dark current signal must be developed.

2.5.2 Slit Image Characterization Introduction

The overall goal of the calibration process is to determine a set of calibrations that can take a raw image like that shown in Figures 2.4 and 2.5 in Section 2.4.4 and produce a single spectrum (or three single spectra) in absolute units as a function of wavelength. The straightforward method to

achieving a single spectrum is to bin or average the illuminated rows into a single spectrum right from the start and then perform all calibrations on this single spectrum. In order to produce this averaged spectrum, a selection of which pixels to average must be made. The easiest method to do this is to select a number of rows for the slit and simply average them together. The problem with this method is that the image of the slit(s) on the CCD is not a perfect rectangle like the slit(s) itself but is instead a curved, or slanted, rectangle. This can be seen in Figures 2.4 and 2.5. This curve is a result of non-idealities in the optics. This means that taking whole rows would result in taking pixels outside of the primary illuminated region as the image curves up or down from the selected row. The solution to this problem is to come up with a criterion for required relative signal strength to exist in any pixel that is used in the averaging of each column. This will result in a smaller deviation in the signal strengths that are being averaged together and will define the slit for all future calibrations and analysis. The criterion that is chosen can be relatively arbitrary as any unwanted effects that this method produces can be calibrated out as long as it is used consistently for all calibrations.

2.5.3 Wavelength Registration Introduction

The wavelength registration is the calibration performed to map each pixel on the instrument CCD to a specific wavelength of light. Due to the resolution of the grating and finite size of the CCD pixels, a single pixel will contain a range of wavelengths that interact with it. However, each pixel is only assigned a central wavelength. In order to perform this calibration, a variety of spectral line sources are measured by the CCD. Then, the pixel location of the center of the spectral line is measured and stored with the known wavelength value of the spectral line used. This creates a set of ordered pairs of wavelength and pixel number that is then fit with a smooth function to generate the wavelength registration.

2.5.4 Spectral Point Spread Function Introduction

The PSF is the calibration used to determine the spectral resolution of the instrument, i.e. the measured width of a spectral line. Monochromatic light, like a spectral emission line, enters the system as an infinitesimally narrow line. As it travels through the optical chain it broadens due to non-idealities in the optics and the resolution of the grating. By the time it interacts with the CCD, its shape can be approximated by a Gaussian curve with the mean value being the location of where the spectrally infinitesimally narrow line would land if it was not broadened. The PSF characterizes the width of this Gaussian shape for all wavelengths. This is done by measuring multiple spectral lines and calculating the spectral width of the measured lines to create a set of ordered pairs for each emission line. Again, these are fit across all pixels with a smooth function as with the wavelength registration. The value of the PSF describes how to lower high resolution spectra down to instrument resolution spectra.

2.5.5 Relative Calibration Introduction

The relative, or flat-field, calibration is the method used to determine the proportional charge accumulation rate of each pixel to every other pixel. This includes the difference in the quantum efficiency of each pixel as well as differences in spectral response of the instrument to different wavelengths of light. The primary goal of the relative calibration is to ensure that the measured signal has the same spectral response as the incoming signal. To perform this calibration, a broadband source of known spectral response, like Tungsten, is measured with the CCD. Then, the known spectrum and the measured spectrum are both normalized to the same wavelength to determine how the rest of the pixels accumulate charge relative to the normalized point. Finally, the ratio of the known spectrum to the measured spectrum is taken to produce the relative calibration curve. This is used as a multiplicative factor for every measurement. By performing this procedure, it ensures that the measured spectrum has the same response as the known

spectrum relative to one pixel or wavelength. This calibration can be renormalized to any desired pixel to make application of the calibration easier.

2.5.6 Absolute Calibration Introduction

The absolute calibration is used to determine the actual brightness, or radiance, of the incoming signal from the measured DN of counts obtained from the CCD. Like the relative calibration, the absolute calibration requires a broadband source of known spectral response, like Tungsten. However, it also requires that the values of the spectral curve be known absolutely in units of radiance (typically photons/s/cm^2/nm/sr). To perform the absolute calibration, a calibrated Tungsten bulb is used to illuminate the CCD. This is done for a variety of exposure times so that a value of DN/s for each pixel can be determined. Then, the rate of DN/s measured is divided by the known spectral radiance at that pixel's wavelength. This produces an absolute calibration value for all pixels.

2.6 Evolution of the OSIRIS-DM Instrument

When the DM was first turned on and operated at the start of this project in 2012, it was a single slit, single line of sight, instrument connected to a ROE box and a GSE computer built in 1994 to operate it. Apart from upgrades to the electronics and operating system of the GSE and ROE that will be discussed in Chapter Three, the DM itself underwent changes as well. As changes to the optical system of the instrument were introduced, calibrations were performed at all major steps. This started with calibrations of the original single slit instrument. The following are the major optical modifications encountered by the instrument along the way to a final instrument.

- Installation of the new slit plate design containing three slits as a prototype for the CATS instrument.

- Installation of the front end optical system consisting of an additional baffle system, a scan mirror, and a shutter system built by *Kozun* (2015). The bulk of the calibration measurements were acquired in this configuration.
- Installation of a new smaller aperture stop designed by *Kozun* (2015). This modification was required to limit the amount of incoming light during the balloon mission that would otherwise saturate the CCD in the allowed exposure times as defined by the shutter system.

By the end of the optical modification, the OSIRIS-DM had evolved to an instrument with three lines of sight, the ability to scan over different look angles and thus tangent altitudes while on the balloon, and was interfaced to a modern set of operating electronics capable of collecting measurements on board a stratospheric balloon. Figure 2.6 shows a picture of the final instrument and control system that flew on the balloon.

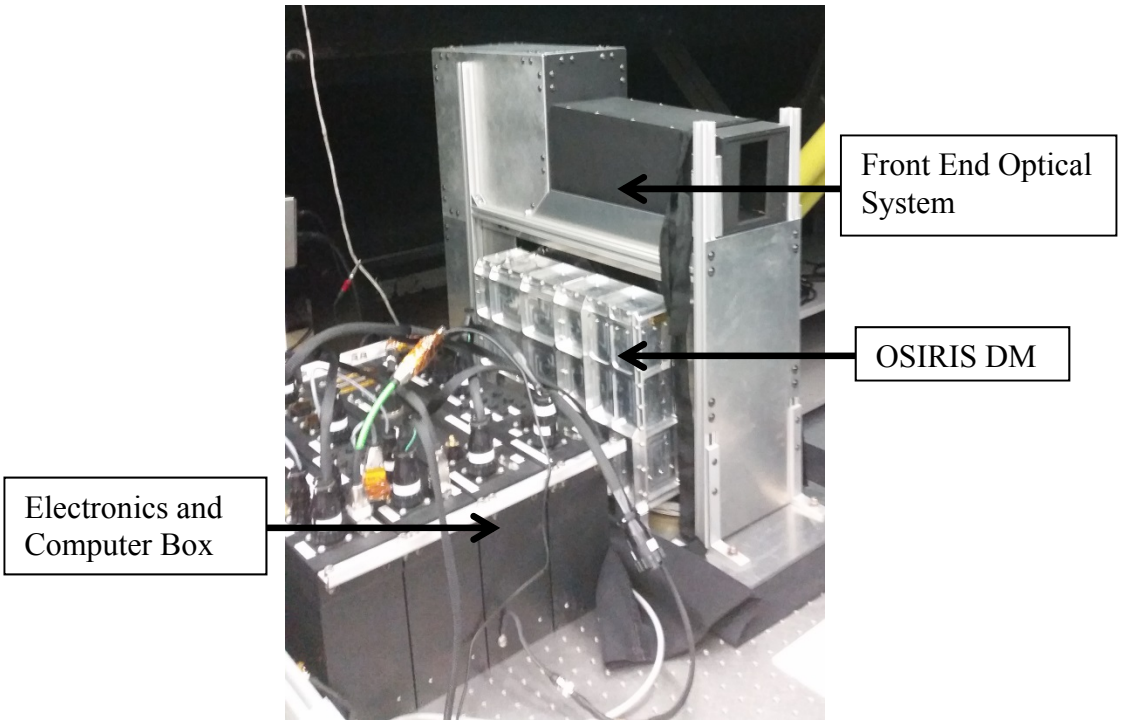

Figure 2.6: Picture of final flight instrument and control system. This includes the OSIRIS-DM, the front end optical system and the flight computer and electronics box.

CHAPTER 3
OSIRIS-DM ELECTRONICS AND COMMUNICATION SYSTEM UPGRADE

The OSIRIS-DM and its support control system were designed to be implemented primarily for laboratory based measurements. This unit served as a proof-of-concept and development testing system for the FM instrument. This means that the system was not meant to be portable and was definitely not meant to be flown on a stratospheric balloon as is proposed for this work. Therefore, the original system needed upgrades for balloon flight. The first step to achieve this was to fully understand the original system and all of its components. A key part of this step was to identify components that could fly in their current state and components that needed replacing.

3.1 Introduction to the Original OSIRIS-DM Electronics and Readout System

The OSIRIS-DM electronics system was comprised of three main units: the GSE control computer, the ROE box, and the CCD electronics. Figure 3.1 shows a schematic of the system.

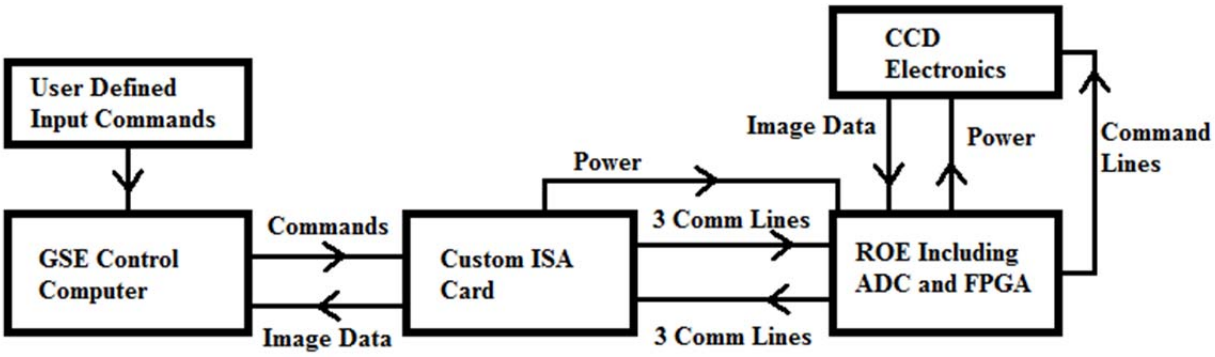

Figure 3.1: Block diagram schematic of original DM electronics system.

The GSE was a standard Windows 95 computer with the modification of a built in custom Industry Standard Architecture (ISA) card. This card was implemented to be the communication interface between the GSE and the ROE. The GSE also served as the power source for both the ROE and the CCD electronics. The ROE box consisted of one circuit board and a sample and hold circuit external to the board. The ROE board contains two FPGAs as the primary processing

units, an ADC that converts accumulated charge from the CCD to DN, and a host of other interface electronics. For this project, only one FPGA is used as the other FPGA controls the infrared channels of OSIRIS which are not used in this work. Finally, the CCD electronics consists of the CCD itself and the electronics used to program it, run it, and clock out the acquired charge. These electronics are internal to the DM and were never considered for modification or replacement as they were deemed to be flight ready in their original state.

The control, or signal flow, starts and ends with the GSE as shown previously in Figure 3.1. The GSE runs a user interface program that takes either automated, or direct, user inputs and converts them into required signals through the ISA card to send to the ROE. The connection between the ISA card and the ROE contained both power and communication lines. The details of the purpose and functionality of these lines had to be discovered primarily by reverse engineering the system as documentation was sparse or non-existent. To achieve this, commands from the GSE were entered and the connection lines were monitored with a logic analyzer to determine signals, timing, and function. The power lines were all determined to be supply lines and contained +5V, -5V, +12V, -12V, +24V, and +36V. The communication lines are both input and output lines; there are three input lines to the ROE and three output lines returning from the ROE. The input lines to the ROE are a clock line, a data line, and a data transfer enable or Data Available (DA) line. The clock line is a 2 MHz square wave that is always supplied to the ROE from power on and does not stop regardless of whether transfers are occurring or not. The purpose of this clock is to be the driving input clock to the ROE for the clocking in, or reading, of the commands. It is also potentially used as the driving clock of the CCD which allows continuous flushing of the CCD while not taking an image and clocking out once an image is acquired, although this could not be confirmed. The data line carries the 16 bit commands

serially into the ROE. Lastly, the DA line is nominally high and goes low to initiate all data transfers. It then stays low throughout the transfer and goes high at the end of the transfer to stop data transfer and signal that the transfer is complete. The output lines from the ROE are very similar to the input lines as they are also a clock line, a data line, and a DA line. The data and DA lines are the same as the input lines except that the data coming back are 16 bit words containing the DN representing the charge read from the CCD pixels. The clock line that returns is a 2 MHz clock as well but with a reduced duty cycle. The purpose of this clock is to read in the serial data stream from the ROE on falling edges of this clock.

In order for an image to be acquired, a variety of commands must be received by the CCD at some point before an image is acquired. First, on every power up, the CCD must be programmed with a 4100 word long sequence of 16 bit commands to configure the system. Once these commands are completed, the CCD is ready to be programmed for image acquisition by receiving commands that describe the mode of operation, the exposure time, and finally a start command to stop the flushing of the CCD and start the exposure. Once an image has been completed, the charge in the image area of the CCD is quickly shifted vertically down into the storage region. From the storage region, each row of the CCD is vertically shifted into a readout row where the pixels are clocked out horizontally in a serial fashion into the 14 bit ADC on the ROE board. The ADC reads in the voltage produced by the charge in each pixel and converts it to a DN. This number is then sent to the FPGA on the ROE board, put onto the data line as a 16 bit word and sent out to the GSE as previously described. This process continues until all of the pixels have gone through the ADC and then the CCD resumes its continuous flushing mode awaiting the command to acquire another image.

3.2 Description of Upgrade Requirements

The primary upgrade requirement that needs to be met for preparing the OSIRIS-DM for the balloon flight is to upgrade the electronics system to a modern, flight ready, and flight compatible version. The most obvious upgrade here is the replacement of the Windows 95 desktop GSE with a computer that can be flown on a balloon. This includes the replacement of the custom ISA card to communicate with the ROE and a new, independent power supply to power the ROE, the DM, and any other necessary flight electronics. This power supply needs to be able to interface to the gondola power source and distribute the gondola power to the voltages and currents required by the entire system. A requirement of all of the new electronics is operation in a near space environment. This means the electronics will need to be near-vacuum compatible and have operating temperature ranges that go down to at least -40 °C. The most challenging aspect to this upgrade is the reverse engineering of the electronics system and communication protocols, especially the custom ISA card as documentation is very limited.

3.3 Details of Communication Protocols

The communication protocols for inputs and outputs of the ROE were determined by reverse engineering the system with a logic analyzer to monitor signals as they travelled through the system after a user interface control program was executed on the GSE. With the logic analyzer and a set of documented commands shown in Figure 3.2, the protocols were determined.

Information on 16 bit instructions from OSIRIS UVIS/IR ROE Manual.

ROE FPGA Design Description July 6, 1995 Version

16 Bit Instruction:	Function:
0000_0000_0000_0000	Reset Command
0000_0000_0000_0001	Set to Load mode command
0000_0000_0000_0010	Set to Run mode command
0000_0000_0000_0011	Start exposure
0000_1ttt_tttt_tttt	Set exposure time register 1 to 0ttt_tttt_tttt
0001_0ttt_tttt_tttt	Set exposure time register 2 to 0ttt_tttt_tttt
0001_1ttt_tttt_tttt	Set exposure time register 3 to 0ttt_tttt_tttt
0010_0xxx_xxxx_xnnn	Set timer clock period to 10^nnn microseconds (us)
0010_1xxx_xxxx_xxx0	Set TDI/Stare mode to Stare (normal mode)
0010_1xxx_xxxx_xxx1	Set TDI/Stare mode to TDI (test mode)
01xx_xaaa_aaaa_aaaa	Set RAM load word address to 0aaa_aaaa_aaaa
10xx_xxxx_dddd_dddd	Load RAM byte with dat dddd_dddd (and inc adr)
11xx_xxxx_xxxx_xxxx	Reserved

Figure 3.2: Copy of a list of documented 16 bit instruction commands that are sent to the ROE to program the DM for image acquisition.

Figure 3.3 shows a representative measured timing diagram of both the input (bottom three lines) and output (top three lines) communication to and from the ROE. This figure should be referred to when reading the following explanation of the communication protocol.

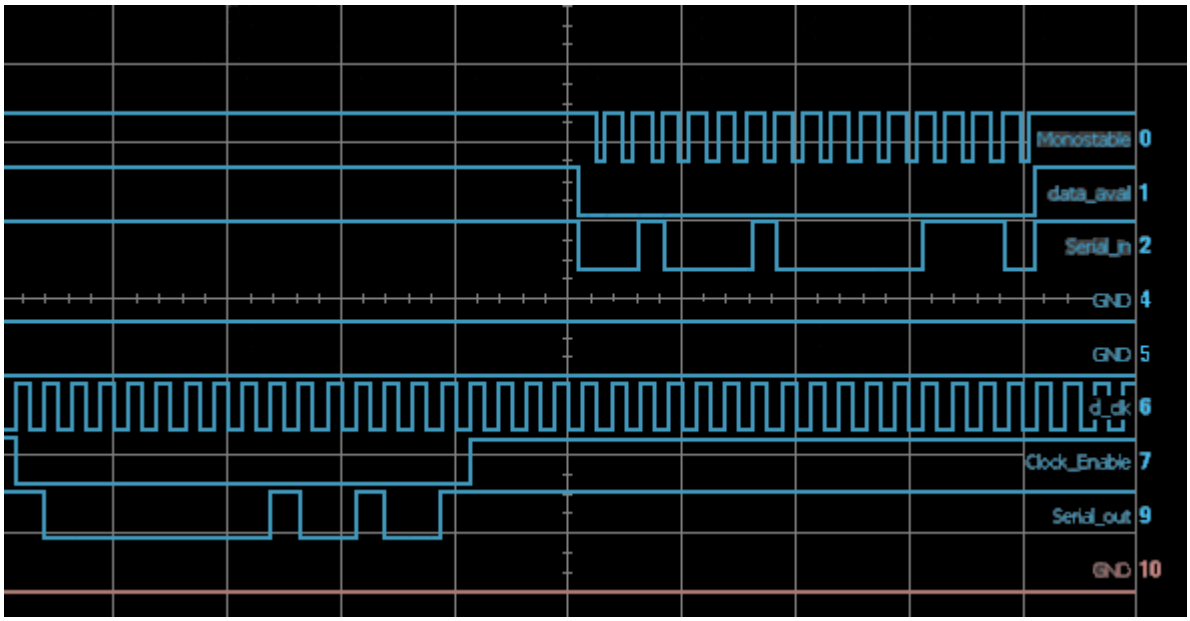

Figure 3.3: Timing diagram output from logic analyzer that shows the input lines labelled 6, 7, and 9 which correspond to clock, DA and data lines respectively as well as the output lines labelled 0, 1, 2 which correspond to clock, DA, and data lines respectively.

As previously mentioned, the input clock line is a 2 MHz square wave with a 50% duty cycle. In terms of communication protocol, the job of this line is to clock the serial data into the ROE on falling edges of the clock. The DA line starts and stops all data transfers; it is the enable line. This line is nominally high which stops data from being transferred. Once data is ready to be transferred, the DA line drops low on a rising edge of the clock and stays low for 16 clock cycles before going high again on the 16^{th} rising edge. This makes the line be low for 16 falling edges which is the required time to read in a 16 bit word on falling edges. This also provides a small gap between the DA line dropping low and the first bit read as well as between the last bit read and the DA line returning high to ensure these bits are read correctly. Lastly, the data line carries the serially shifted data. This line keeps the value of the last transferred bit when no transfers are being executed. Therefore, if the last transferred bit is a 1 as in Figure 3.3, then the line will stay high until the next transferred bit is a 0.

Once an image has been acquired and begins to be shifted out to the ADC, the receive side of the communication for the GSE begins and is depicted by lines 0, 1, and 2 in Figure 3.3 which are the clock, DA, and data lines respectively. On this side of communication, the clock line is only enabled during data transfer and is therefore enabled by the DA line. When the clock is not enabled, the line is nominally high. Once enabled, the clock supplied is a 2 MHz clock but with a reduced duty cycle. The high time is 2-3 times longer than the low time as can be seen in Figure 3.3. The reason for this was never determined as this clock line is only used to read in the data on falling edges just like the input clock. The DA line has almost the exact same function as on the sending side; it stays high until a data transfer is required and then drops low to enable both the clock and the data transfer. The small difference is that it does not need to go low on the rising edge of the clock as the clock does not exist until the DA line goes low. Therefore, a data

transfer can be initiated at any time with no constraints. The DA line will stay low for 16 falling edges of the clock and return high on a rising edge for the same reason as described above for the input DA line. The data line is the same as on the send side except that it is nominally high when no data is being transferred. Even if the last bit is low, it will return high when the DA line goes high as displayed in Figure 3.3.

3.4 Hardware Approach to Solution

The first step to upgrading the electronics system is to find suitable replacements for the Windows 95 computer and custom built ISA card. The obvious replacements for these are a new computer that is flight compatible and a piece of interface electronics to communicate between the new computer and the ROE. This interface hardware needs to allow full control and manipulation of the signals on both sides of the interface so that the custom protocols described previously in Section 3.3 can be reproduced. It also needs to be able to produce a constant 2 MHz clock at all times and run other signals off of this clock in synchronization with clock edges. The first choice for this interface was to use an FPGA. This worked very well for having full control of timing of the signals especially in regard to the constant clock and synchronizing clock edges with other signals. Unfortunately, this solution, which used Universal Serial Bus (USB) communication protocols, ended up being very challenging to interface to the flight computer reliably and eventually proved to be too unreliable for flight. Instead, a microcontroller was chosen for this task in the system. The microcontroller used was a LM4F120H5QR microcontroller contained on a Stellaris Launchpad Evaluation Board. The Launchpad Board supplied easy access input and output pins as well as a built in USB interface to power and program the microcontroller. The Launchpad was chosen for three main reasons. First, it offered a very easy and reliable way to produce a 2 MHz clock that would always be output and a way to run this clock line back into the microcontroller to internally synchronize other signals. The

second reason is that it had a variety of built in options for serial communication that allowed different options to create the required communication protocol. Finally, the Launchpad met all of the requirements for flight; it is near-vacuum compatible and operates down to -40 °C.

Once the Launchpad was chosen as the solution for the interface electronics, the flight computer, the Ocelot, was chosen. The Ocelot is a computer built by VersaLogic. It is a single board computer with an Intel 45 nm Atom Z5 processor featuring the Stackable Unified Module Interconnect Technology (SUMIT) and PC/104 expansion interfaces. The Ocelot was chosen for three main reasons. First, it supports the same serial communication protocols as the Launchpad which made interfacing of these components simple. Second, as a Linux machine, the Ocelot provided control at the base levels which allowed it to run simple programs designed for the OSIRIS-DM system hardware without requiring a lot of overhead. Finally, as with the Launchpad, the Ocelot met all environmental requirements of the flight: near-vacuum compatibility and an operating temperature down to -40 °C. While the flight computer and interface electronics were being developed, the development of the DC/DC power supply was happening in parallel. The development of this system was conducted by Paul Loewen, a research assistant in the project research group. This system was built on requirements provided by the CSA for interfacing to the gondola power system and based on the DM and flight electronics requirements for interfacing to the instrument and electronics system.

The final electronics upgrade completed on the hardware of the system was removal of the ROE box. This was achieved in two steps. First, the sample and hold circuit inside the ROE box was determined to be obsolete as its only function was determined to be a test circuit for the ROE board. Therefore, this component was removed from the system without affecting operation. The second step was moving the ROE board out of the ROE box and into the DM.

This was possible because the DM has card slots that the ROE board could plug into. Once inside the DM, the final modification was developing a method to distribute power and signals to the ROE card in its new configuration. This was achieved by building a custom power card and signal interface card that could plug into other, unused, card slots in the DM. With this final upgrade complete, the flight system hardware was complete. A schematic of the final system is shown in Figure 3.4.

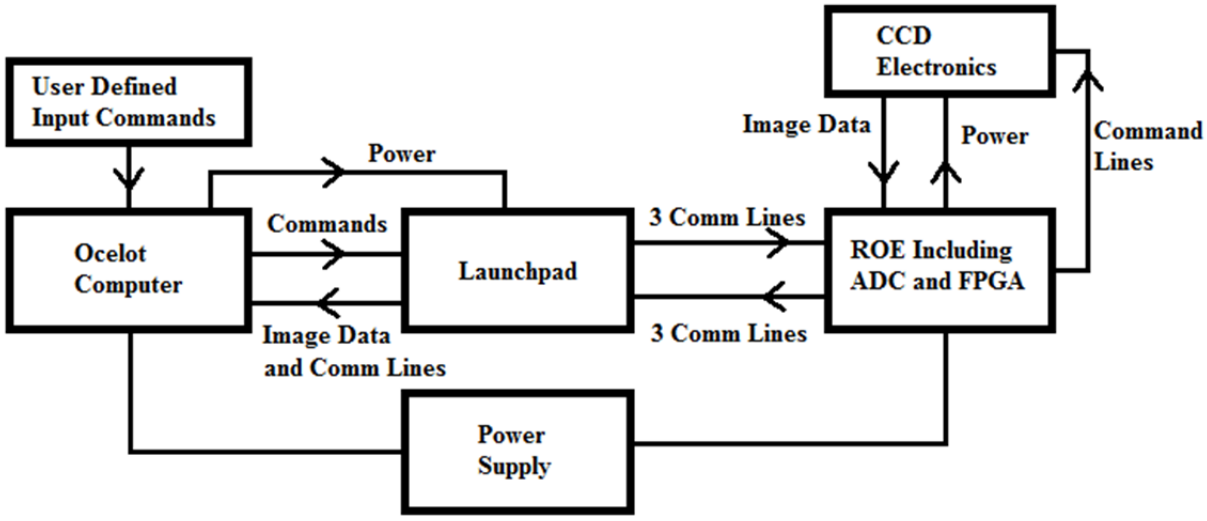

Figure 3.4: Block diagram schematic of upgraded electronics system.

3.5 Communication Protocol Modification for Solution

The first step in preparing the previously described components for operation in a standalone flight system was to program the Launchpad to communicate with the DM using the protocol described earlier. Generation of the 2 MHz clock was achieved with the use of a General Purpose Input Output (GPIO) pin that could be configured as a square wave generator. The true frequency of the generated wave is not a perfect 2 MHz as it carries an error of +/- 0.1 Mhz. This range is accurate enough to allow proper operation of the DM. Next, the Launchpad was required to be able to send a 16 bit command to the DM with the proper protocol and synchronization.

The first effort at a solution was to find a standard serial protocol that was supported by the Launchpad that could perform these functions automatically. The Launchpad supports a variety of Synchronous Serial Interface (SSI) protocols that use a data line, a clock line, and a frame, or DA, line which is exactly what was required. The problem was that none of these standard protocols performed exactly the functions and timing required to communicate properly with the DM. Some of the protocols were close but the main difference in the standard protocols versus the DM protocol is the existence of parity or synchronization bits that could not be sent to the DM as they would be interpreted as new commands. A second issue with the standard protocols was that they did not have the required timing or synchronization.

A solution was designed by using the SSI protocol that was closest to the required protocol and manually manipulating it to meet requirements. The closest standard protocol had everything that was required except that after a transfer was complete as signaled by the frame line returning high from low, it would not remain high. Instead, the line would stay high for only one clock cycle and then return to low. A timing diagram of this protocol is shown in Figure 3.5.

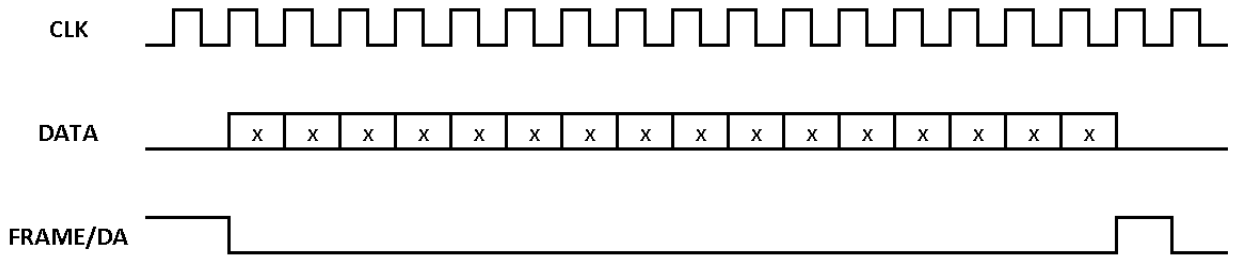

Figure 3.5: Timing diagram of closest standard SSI protocol supported by the Launchpad.

This protocol will not send data on this drop back to low but if this signal is sent to the DM, it would incorrectly interpret this drop as a new data transfer. Therefore, the protocol was modified to a usable configuration.

The SSI protocol can be operated in master or slave mode. If it is operated in master mode, the SSI module produces the clock and data enable signals automatically when data to transfer is sent to the module. However, if it is operated as a slave, these signals need to be provided from an outside source. The solution to creating the custom protocol requires the module to operate in slave mode. The protocol in slave mode takes a 16 bit command word and stores it in a First In First Out (FIFO) module that can hold up to 8 words. It is from this FIFO that the data is put onto the data line when it is time to send it. The next step is to provide a clock line to time the serial transfer. This clock line can be supplied at all times or only during the transfer. The protocol only needs it during transfers; outside of transfers, the line has no effect on the module. Therefore, for the DM application, this line can be tied to the constant 2 MHz clock being sent to the DM and properly time the protocol. The last step to completing a transfer is to provide a frame line to the SSI module that initiates a transfer with a change from high to low. Data will transfer continuously until the frame line returns high. The standard frame line used returns high for only one cycle before going low again. This is where the modification to the protocol comes into play; it is in how this frame line is provided.

The modified operation of the SSI module is to send a 16 bit command to the SSI FIFO that will eventually go onto the data line. Then, a synchronization timer is started that will count a few clock cycles of the 2 MHz clock and trigger an interrupt on a falling edge. When this interrupt is triggered, a GPIO line that goes to the frame line of the SSI, and in turn to the DM, is dropped from high to low in synchronization with the clock edge. This starts the data transfer. Also in this interrupt, a second timer is started that counts rising edges of the clock and triggers another interrupt after 16 rising edges. In this final interrupt, the frame line is set high again on the rising clock edge to stop the data transfer and all of the interrupts and timers are reset to their

normal idle state to await the next data transfer. In this setup, the SSI module is a slave to the rest of the microcontroller. The 2 MHz clock line and the frame line are generated by the microcontroller and are sent to the SSI module which in turn sends them to the DM along with the transfer data. This sequence results in a proper transfer protocol that the DM can interpret correctly without fail. In the end, the timing diagram looks identical to Figure 3.5 except that at the end of a transfer, the frame line stays high until the next transfer is ready to be initiated.

3.6 Software Implementation for Communication System

The previous section covered how the Launchpad sends information to the DM. The rest of the communication system including receiving from the DM and the communication between the Launchpad and the Ocelot is now considered. When receiving data from the DM, the same SSI protocol is used again in slave mode and is controlled by the DM. In this slave mode setting, the module can receive the data line, the clock line, and the frame line as they are produced by the DM without any modification and read the data correctly. The only issue with the receive side is that the DM is the master and is driving all of the transfers. Due to the fact that there is no feedback to the DM from the Launchpad, the DM sends out data at a constant rate regardless of what happens in the microcontroller. This means that the data transfers from the DM need to be serviced fast enough so that data is not lost. If the Launchpad misses a data transfer, there is no way to resend or retrieve the missed data. The limitation to this timing comes from the SSI module operation. The SSI module has a receive FIFO buffer, similar to the sending FIFO, that can only hold eight 16 bit words. In order to service the FIFO fast enough, the SSI module supports internal interfacing to Direct Memory Access (DMA). DMA works by receiving an interrupt request once the receive buffer is filled up with eight words and when this interrupt is serviced, the buffer is shifted out in parallel to a previously allocated memory location. This operation is very fast and allows for the buffer to be transferred out before a new word is

received from the DM. This handles servicing the DM fast enough. However, the next issue encountered is that the Launchpad does not have enough internal memory to store an entire CCD image and then send it to the Ocelot once it is all received. This means that as the image is being read in from the DM, it also needs to be actively sent out to the Ocelot. This was achieved by using a method called ping pong DMA. In this method, at the start of data acquisition, buffer A is set up as the storage location for the DMA to send data to. Once buffer A is full, the storage location is switched to buffer B and while buffer B is being filled, the rest of the microcontroller has full access to buffer A. This means that buffer A can be sent out to the Ocelot while buffer B is being filled by the DM. In this system, the only requirement needed to not lose data from the DM is that buffer A has to be empty and ready to be filled again before buffer B is finished being filled. If this requirement fails, the microcontroller will have memory access issues and won't service the DM properly.

On the first implementation of this design, this was the exact problem that was encountered; buffer A was not empty by the time buffer B was full and thus data from the DM was lost. To alleviate the problem, two more buffers were added in to the system. With this new, four buffer system, first buffer A was set up as the primary buffer and buffer B as the secondary. When buffer A became full, buffer B became the primary buffer and buffer C was set up as the secondary. Then, when buffer B is full, buffer C becomes primary and buffer D becomes the secondary buffer. This process then loops back to the top and repeats. The requirement for this implementation is that the most recently filled buffer needs to be emptied in less time than it takes to fill three more buffers and that any delays in the system do not back up the system so much that memory access becomes an issue. This method worked reliably for the DM image sizes and was implemented in the flight version software.

With communication between the Launchpad and the DM completed and implemented, the next step was the communication with the Ocelot computer. The communication between these two devices was significantly easier to implement as both modules supported a serial protocol called Serial Peripheral Interface (SPI) that could be implemented. The only challenge came in determining which machine would be the master and which would be the slave. The Launchpad needed to be in control of initiating transfers because if the Ocelot was in control, it could request data when no data was available which would result in synchronization issues. However, the Ocelot needed to be the one that supplied the clock and frame signals to the Launchpad SSI module to initiate data transfers which meant that it needed to be the master. The implemented solution was to make the Ocelot the master and the Launchpad the slave in terms of the protocol but with the addition of an independent GPIO line that allowed the Launchpad to tell the Ocelot when it was allowed to request data. The operation of this implemented design starts when the Launchpad has data to send to the Ocelot. The Launchpad first sets a GPIO pin high which is read by the Ocelot. This signals the Ocelot to enter a receiving state and initiate the serial transfer by providing a clock and frame line. When the Launchpad receives these lines, it starts to send out the data in synchronization with the clock. Finally, the Ocelot receives this data, clocks it in and stores it. Full details on the software design can be found in Appendix A.

3.7 Hardware and Software Issues and Resolutions

Throughout the development process of the flight hardware upgrades and software implementation, some issues were encountered along the way and were resolved to create the final product. The first major issue was with the use of interrupts on the microcontroller to time the frame pulse low time. The job of this interrupt was to drop a GPIO pin low when triggered on a rising edge of the 2 MHz clock and start a counter to count rising edges of the clock line. The original configuration was to have the counter count 16 rising edges before triggering another

interrupt to set the line back high. The problem that arose with this configuration was that the latency in servicing of the interrupt would keep the pulse low longer than desired thus telling the DM to read extra bits in this time. Upon investigation, the interrupt latency was found to be exactly two clock cycles at the 2 MHz frequency. Therefore, the easy solution to the problem was to make the interrupt counter count only 14 rising edges of the clock and then trigger the interrupt. The time that it took for the microcontroller to service the interrupt request and set the frame line high again was perfect timing for the DM to read the 16 bit command properly. However, there are reliability issues with this solution as it relies on the latency of the microcontroller to function properly. Therefore, if this latency time changes due to operating conditions such as temperature, the timing will be incorrect and the command sending code could fail. With this in mind a new solution to provide the frame line using external hardware components was designed. The idea was that a hardware solution should be more robust and have less latency. The attempted solution was to build a circuit board with external timers and counters that would read in signals from the microcontroller and create the frame line external to the microcontroller when prompted. Then, the board would be able to count the proper clock pulses, set the frame line to the DM high to stop data transfer, and send a signal to the microcontroller to tell it that the send process is over. With this design, any major latency would be in the send between the external board and the microcontroller when the send process is to end. This is acceptable because as long as the DM knows the transfer is over on time, it will not read again even if the microcontroller is still sending. The microcontroller can sit in a sending/waiting state until it gets the end transfer signal from the board and not negatively affect operation other than a slight overall delay that makes the whole process slower. Unfortunately, the implementation of this solution failed and the cause of the failure could not be diagnosed

before the balloon launch time. Therefore, this solution had to be discarded and the flight version solution implemented was the software driven interrupt design. Fortunately, this design worked perfectly during flight. The last major issue that was encountered arose with the changing of communication cables from laboratory cables to balloon flight cables. The primary difference in these cables was that the balloon cables were required to be 4 m long while all laboratory cables were less than 1 m. When the 4 m cables were put into the system, the signals being sent through the system became attenuated and noisy to the point that they were unreadable by system components. The solution to this issue was to build interface circuit boards with differential line drivers on all of the signal lines going through the 4 m cables. This solution alleviated the problem and provided successful operation with the flight configuration system.

With all of the hardware upgrades completed, the software solutions implemented, and the few issues resolved, the final upgraded version of the electronics was fully operational for flight. With a working instrument, the next step was to complete the calibrations of the flight instrument.

CHAPTER 4
PREFLIGHT CALIBRATION OF THE INSTRUMENT

4.1 Dark Current Calibration

4.1.1 Origins and Dependencies

A dark current calibration is dependent on two factors: temperature and exposure time. Temperature alters the amount of dark current measured by changing the rate at which it is generated. The higher the temperature, the more thermal energy there is available in the silicon lattice to excite electrons and create signal. The dark current generation rate (DN/s) is proportional to the carrier concentration (n_e) in the semiconductor which, according to *Grahn* (1999), in an intrinsic semiconductor, is given by Equation 4.1.

$$n_e = \sqrt{N_C N_V} exp(-E_G/2kT) \tag{4.1}$$

In this equation, N_C and N_V are the effective density of states in the conduction and valence bands respectively, E_G is the band gap energy (in eV) for the material, k is the Boltzmann constant and T is the CCD temperature (in Kelvin). The exponential term in this equation is the dominating factor and thus a plot of the log of DN/s versus $1/T$ should be linear with a slope of $-E_G/2k$.

The second factor, exposure time, changes the amount of dark current measured by changing the amount of time it has to accumulate. If the CCD is kept at a constant temperature, and thus a constant dark current generation rate, then a plot of the amount of dark current measured versus exposure time should be linear. Therefore, the slope of this line will give a value in units of dark current per second which is the generation rate for that specific temperature. The y-intercept of this linear equation should be 0 because at a time of 0s there is no time for dark current to be accumulated. However, due to the DC offset applied to the DM

readout, the value of the y-intercept should be equal to the DC offset prior to removal. Both of these factors and their expected trends will be examined in more detail in Chapter Five when the theory is applied to the flight measurements.

4.1.2 Preflight Dark Current Removal Process

Instead of determining the dark current calibration as a function of exposure time and temperature for laboratory measurements and calibrations, a simpler technique was developed. This simpler technique involves always acquiring a 'dark image' (an image acquired with no illumination signal) immediately after an illuminated image is acquired. This dark image will be measured at the same exposure time in essentially the same operating conditions as its corresponding illuminated image. Therefore, the dark image will provide a measurement of dark current accumulation, DC offset, and any background signal measured in the illuminated image. This method allows for a direct pixel by pixel subtraction of the dark image from the illuminated image to produce a corrected image that contains only the desired signal used for calibrations. In order to verify this method, two successive dark images were acquired in the laboratory at the same exposure time and subtracted from one another. In theory, this should produce a corrected image of 0 counts in every pixel. However, the resulting corrected image is subject to random changes in the accumulation of charge in every pixel such as noise. For large numbers of electrons, this effect is random and it is expected that a histogram of the corrected image pixel values will be centered on 0 counts with a Gaussian distribution. The Half Width at Half Maximum (HWHM) of this Gaussian will give an estimate of the error in this method. Figure 4.1 shows the resulting histogram of the pixel values normalized in exposure time of ten corrected images sorted into 1 DN/s wide bins. Outside of the displayed range are a few outlier points that can be considered negligible.

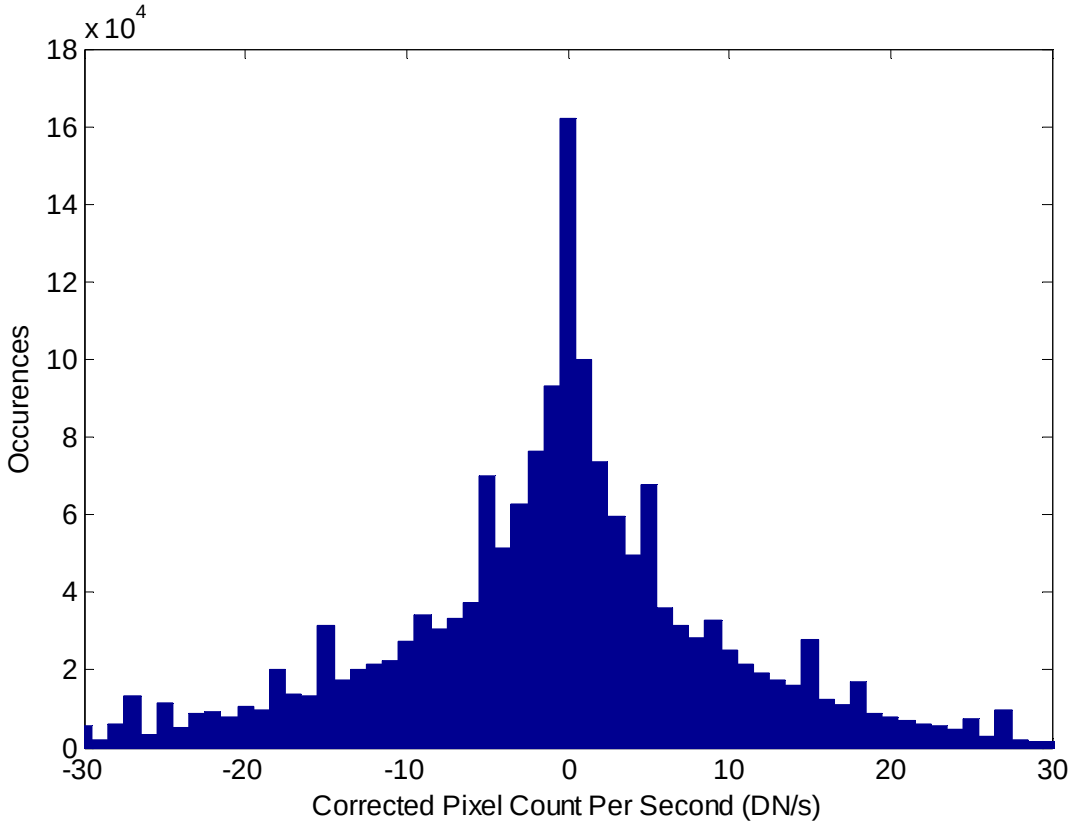

Figure 4.1: A histogram of all of the pixels in ten dark images after subtracting a successive dark image of the same exposure time sorted into 1 DN/s wide bins.

The resulting histogram does not exhibit the expected Gaussian shape, but it does show a distribution that is centered on 0 DN/s as was expected. This plot can still be used to take the HWHM of the distribution to yield an error of +/- 4 DN/s on the dark current removal process which is a very reasonable result. Therefore, it is concluded that the method is valid for all laboratory calibrations for both the single slit and multi-slit systems. This method could be used for flight measurements as well but it would require a dark image to be acquired after every illuminated image which would halve the data acquisition rate. Being that maximum data retrieval is desired from the balloon flight, a calibration method dependent on exposure time and temperature will be developed for the flight measurements.

4.1.3 Collecting the Flight Calibration Measurements

In order to perform a proper dark current calibration, a large number of 'dark images', or images with the shutter closed in this case, need to be collected. These images need to vary in exposure time with constant temperature and vary in temperature with constant exposure time so that both dependencies can be characterized. During the balloon flight, a perfect opportunity to collect these measurements is during the balloon's 2-3 hour ascent. During this time, the balloon will be going through a large temperature change and cooling off as it rises. This will allow dark current measurements to be acquired over a large temperature range. Also, due to the relatively slow ascent, the temperature should be relatively stable for short periods of time. This will allow for multiple sets of varying exposure times to be acquired at relatively constant temperatures.

An image acquisition mode was developed to take continuous sets of dark current images throughout ascent. An image set is comprised of exposure times of 0.11, 0.6, 1.1, 2.1, 4.1 and 8.1 seconds. This set of times was arbitrarily chosen to span the allowed exposure times of the instrument with an emphasis on times around 1 second as this was the expected operating range while on the balloon. The temperature of the CCD is logged by an automated temperature sensor that is attached on the outside of the DM as close to where the CCD sits as possible. It is not possible to attach a sensor to the CCD itself, so it is assumed that the temperature on the outside of the CCD will be a sufficient estimation of the CCD temperature.

4.1.4 Removal of the DC Offset

The readout row of pixels on the CCD of the DM has a circuit connected to it that supplies a DC offset voltage to the gates of each of the pixels in the row as they are read out. This produces an offset signal in the value that is sent to the ADC and thus an offset value in the DN recorded for every pixel. This voltage can be slightly different for each row and varies with temperature but is independent of exposure time. The purpose of this offset is to elevate the baseline signal to a

value above zero, which is required for proper operation of the ADC. The readout row of the CCD contains a front eight pixels and a back eight pixels that are attached on either side of the 1353 CCD pixels as was shown in Figure 2.2 in Section 2.4.3. The purpose of these pixels is to measure the DC offset that is being applied to every row that is read out to allow for removal from the final data product during analysis. These DC offset pixels are masked so that they do not accumulate any photo-charge and are also continuously flushed until they are read out so that they do not accumulate dark current. Figure 4.2 shows one row of the CCD in a dark image taken at 22 °C where the DC offset can be seen in the first and last eight pixels. It also shows how the signal in the pixels in between the first and last eight is always higher than the DC offset value as is expected. This additional signal is the dark current signal.

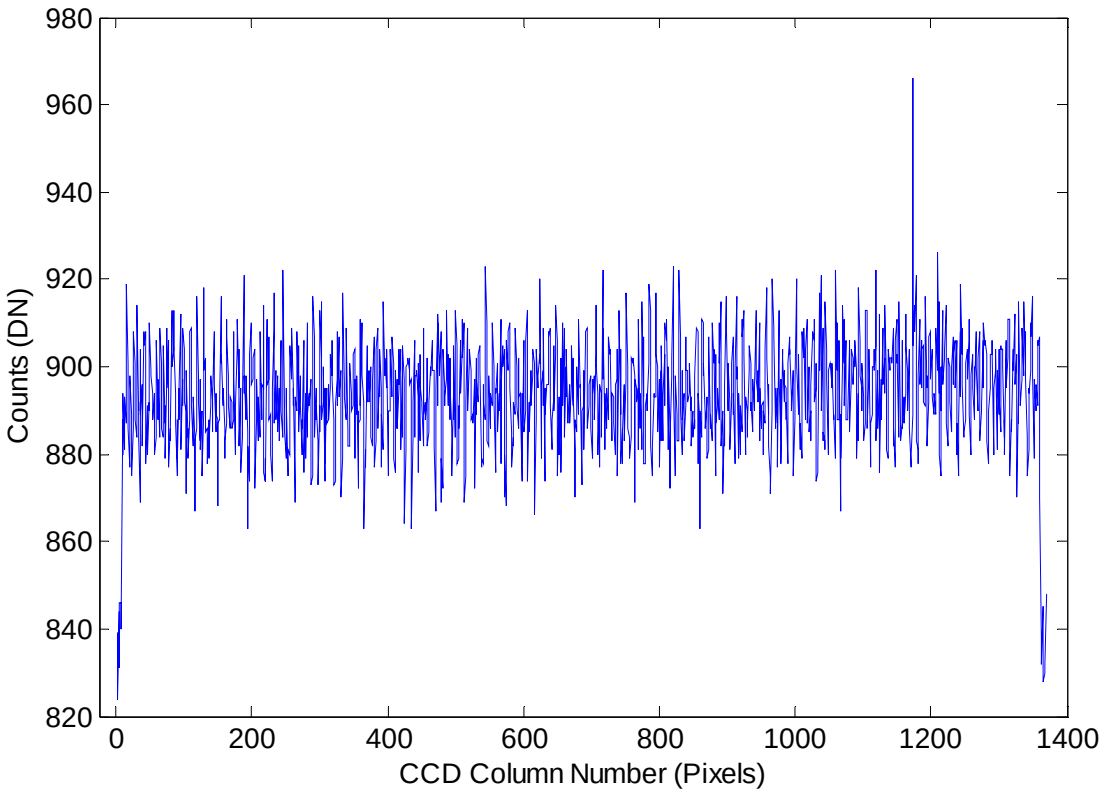

Figure 4.2: Dark current signal with DC offset measured at 22 °C. The DC offset value is measured in the first and last eight pixels and is not subject to dark current accumulation during imaging. This is why the signal in between is at a higher value as these pixels do accumulate dark current during imaging.

In order to obtain a measurement of the magnitude of dark current signal generation for characterization, the DC offset signal must be removed from the final signal value. A measurement of the DC offset can be found from the first and last eight pixel values in every row. If the measured DC offset in these pixels is removed, the remaining signal should only be due to dark current generation. However, it does take a finite amount of time for the 1369 total pixels to be read out one at a time and the last pixels in the row spend more time in the readout row than the first pixels. This means that the last pixels can accumulate some dark current during readout. This signal is accounted for by looking at the signal in the last 8 DC offset pixels which will accumulate the most signal from dark current of any of the readout pixels. In order to remove the DC offset and the small amount of dark current from the readout pixels, the following steps are done. First, the first and last eight DC offset pixels are independently averaged. Then, a linear interpolation is performed between these average two values across the 1353 pixels to scale the dark current accumulation as it is assumed to be linear. Finally, these values are subtracted from the entire row leaving only the dark current signal accumulated prior to readout. This method of removing the DC offset needs to be applied to all images that do not use the dark image removal technique before being used for calibration or analysis. This method will be applied and tested with flight measurements in Chapter Five.

4.1.5 Dark Current Characterization and Removal

Once the DC offset can be removed from the dark images leaving only the dark current signal, it can be characterized into a removal process. To perform the removal, we start with a modified version of Equation 4.1. Remembering that the carrier concentration (n_e) is directly proportional to the rate of dark current generation (DN/s), then the log of Equation 4.1 is taken and rewritten as Equation 4.2.

$$\log([DN/s]) = m/T \tag{4.2}$$

In this equation, m is equal to $-\mathrm{E_G}/2\mathrm{k}$. The slope of this line can be used along with Equation 4.2 to give an equation for finding the dark current per second rate. Finally, this equation can be multiplied by the exposure time of the image to give a value for the amount of dark current accumulated by each pixel.

$$Dark\ Current = \exp(m/T)\ (exposure\ time) \tag{4.3}$$

To verify the accuracy of this equation and removal process, the removal technique will be applied to a dark image taken during flight that is not used to generate the calibration. After the removal process is complete, a histogram of the values of all the pixels in that image will be created. This histogram should have a Gaussian shape centered on 0 DN to show that the removal method works. The width of this histogram will give a value for the error in the dark current removal method. As previously mentioned, application of these methods and evaluation of their performance will be handled in Chapter Five.

4.2 CCD Slit Image Characterization

4.2.1 Definition of Usable Pixels

The primary issue considered when determining the criterion for the usable pixels of each slit when projected onto the CCD is to choose pixels that are far enough away from the slit edges that any edge effects on the incoming light will be avoided. As was mentioned previously in Section 2.5.2, the criterion is somewhat arbitrary due to the fact that any unwanted effects from this method can be calibrated out. With this in mind, the following criterion was set. A usable pixel is defined to be a pixel that contains a signal of at least 90% of the maximum signal for a given column in a given slit. In order to find these pixels, an image of a Tungsten bulb is acquired and analyzed using the usable pixel definition. Figure 4.3 shows a vertical cross section of the CCD for one column to illustrate this criterion for the single slit instrument. The criterion

for the multi-slit instrument is the same but applied on a slit by slit basis. The verification of these usable pixels is to plot them over top of a Tungsten image and visibly check for issues. In this example, 8 pixels are selected as usable pixels. This is not always the case as the usable pixels chosen are dependent on the column and slit in the multi-slit case.

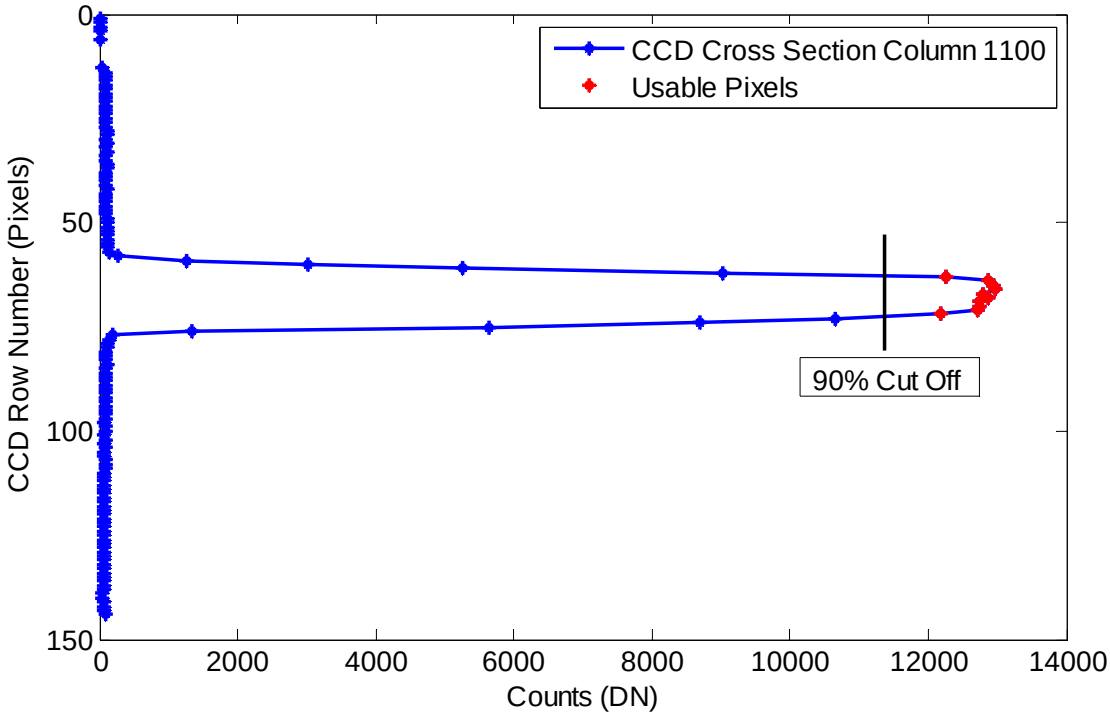

Figure 4.3: Cross section of CCD for a single slit system image at Column 1100. This displays the criterion used to select the usable pixels.

4.2.2 Single Slit Characterization Results

With the above criterion determined, the method to determine usable pixels was implemented on the original single slit system. This was done by applying the criterion to a Tungsten measurement. Figure 4.4 shows a plot of a Tungsten image with the single slit system usable pixels plotted over top in white.

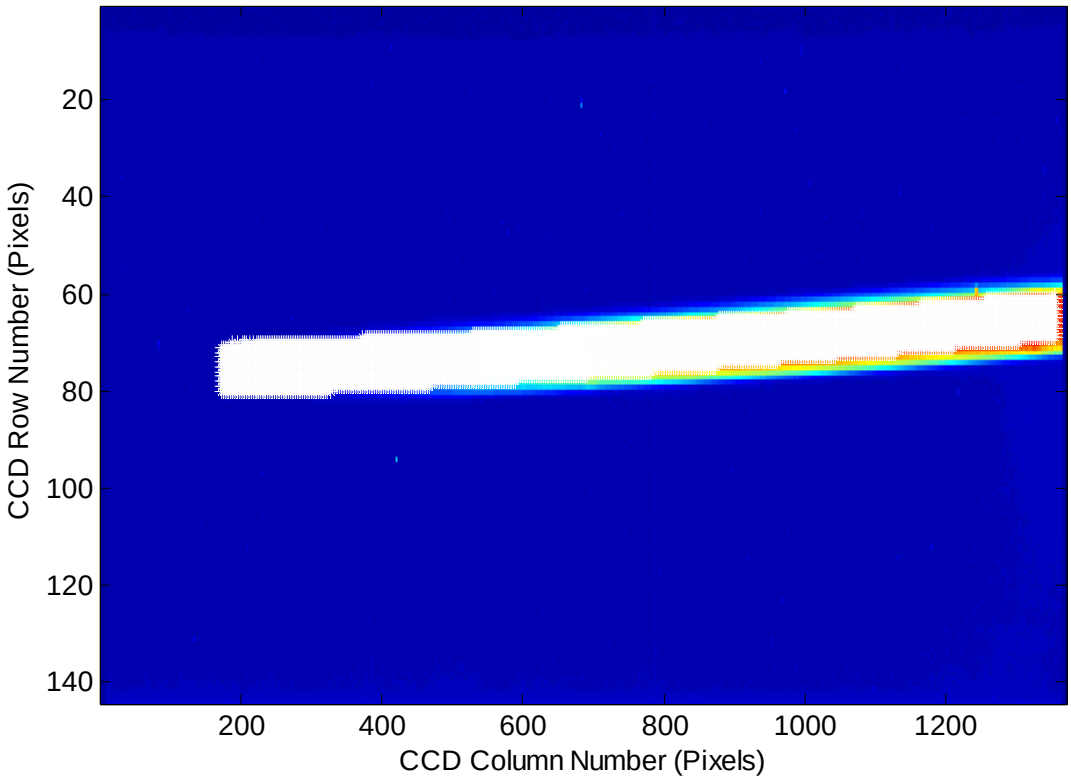

Figure 4.4: Original single slit system Tungsten image with the usable pixels plotted over top in white. The outline of the measured spectrum can be seen around the edges of the white usable pixels showing that the usable pixels are contained within the illuminated region.

As can be seen, the usable pixels span the central area of the illuminated region on the CCD as was desired. This also shows that an average taken over these pixels appears to be a good representation of the spectrum. The usable pixels do not extend all the way down to pixel 1 because this region is hard to characterize due to low signal levels. Also, this spectral region was not required for the calibration performed on the single slit system.

4.2.3 Multi-Slit Characterization Results

After the new slit plate was installed into the DM, the slit characterization method was reapplied to the CCD for all three individual slits. The same method was used except that the maximum signal value in a given column became localized to each individual slit. Figure 4.5 shows a

Tungsten image acquired with the new multi-slit plate with the usable pixels for each slit plotted on top in white.

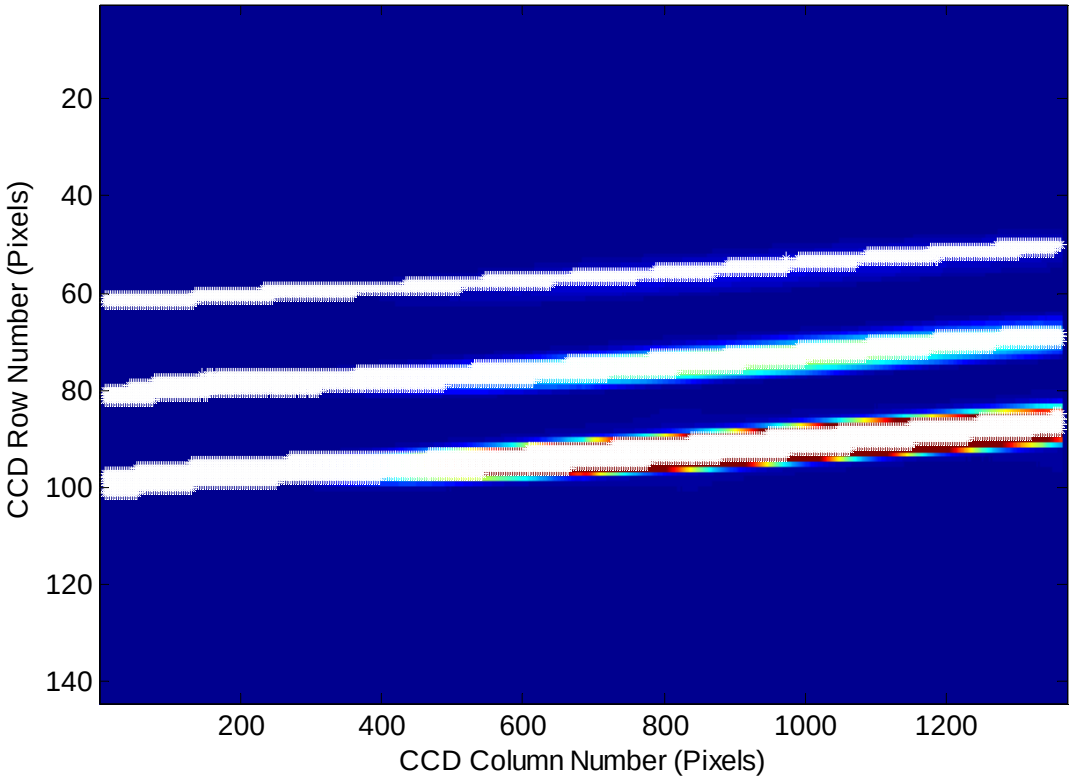

Figure 4.5: A multi-slit Tungsten image with the usable pixels plotted on top in white. The outline of the Tungsten spectrum can be seen outside of the usable region which demonstrates that the usable pixels are inside of the illuminated region for each slit.

As with the single slit characterization, Figure 4.5 shows how the usable pixels populate the middle of the illuminated region for each slit and appear to be a good representation of each slit. This time, the usable pixels span across all pixels because it was required for the remainder of the calibrations of the multi-slit system. Getting the usable pixels below Column 200 is challenging to achieve as signal levels in this range are very low with the calibration sources available in the lab. Therefore, the linear trend of the usable pixels above Column 200 was extrapolated down to Column 1.

4.3 Wavelength Registration

4.3.1 Development of Wavelength Registration Technique

To perform a wavelength registration, a series of spectral emission lines are measured by the CCD. It is assumed that the images of these infinitesimally narrow lines are ideal Gaussian curves on the CCD in terms of number of counts in the illuminated pixels. This assumption holds in theory, but in practice is subject to non-idealities of the CCD. The primary effect that alters the curve shape is the fact that not every pixel is identical to one another in how it accumulates and registers charge, i.e. the gain and quantum efficiency varies across the pixels. This effect can be characterized with a relative calibration, but to perform a relative calibration, a wavelength registration is required. This creates an iterative process that must be done to achieve accurate wavelength and relative calibrations. With this effect characterized and the Gaussian assumption in place, the wavelength registration relies on the fact that the center of the Gaussian peak, or mean value, is the place on the CCD where the spectral line would land if it could remain infinitesimally narrow when it reaches the CCD. This allows a Gaussian fit to be performed to the measurement and the mean value to be extracted as the pixel location for each spectral line. When this method is performed on a variety of spectral lines, it produces a set of ordered pairs of the form (wavelength, CCD pixel position) that can be used to create a fitted function describing all pixels and wavelengths of the CCD. The reason that the mean must be extracted from a fitted equation rather than just taken as the peak value on the CCD is that the true peak value will most likely not hit the exact center of a pixel, but rather somewhere in between the centers of two pixels. Therefore, the fitted peak will be a fraction of a pixel and using these fitted peaks to develop an equation for whole pixels will produce the wavelength registration for the pixel centers of the CCD.

To find the mean peak position of each spectral line, the Gaussian assumption and equation is employed and manipulated as follows. First, start with the equation of a Gaussian.

$$f(x) = a \exp\left(-\frac{(x-b)^2}{2\sigma^2}\right) \tag{4.4}$$

In this equation, a is the amplitude, which can be set to 1 without loss of generality, b is the mean or peak value, x is the pixel range that the Gaussian spans, and σ is the standard deviation. From this equation, the mean is the desired parameter to extract. In order to extract the mean, the log of both sides of Equation 4.4 is taken and expanded into a quadratic equation.

$$log\big(f(x)\big) = -\frac{(x-b)^2}{2\sigma^2} \quad = \quad -\frac{(x^2 - 2bx + b^2)}{2\sigma^2} \tag{4.5}$$

From examining the coefficients of the quadratic, it is seen that the quadratic coefficient contains only the standard deviation term and the linear coefficient contains both the standard deviation and the mean. Therefore, if the coefficients can be found, the standard deviation can be found which will allow the mean to be found as shown.

$$\sigma = \sqrt{\frac{1}{(-2) * quadratic\ coefficient}} \tag{4.6}$$

$$b = \sigma^2 * linear\ coefficient \tag{4.7}$$

In order to get these coefficients, the spectral line image is acquired and each peak is isolated as shown in Figure 4.6 (left). Then, the log of this isolated peak measurement is taken and a quadratic function is fit to the resulting points using the method of least squares to find the best fit as shown in Figure 4.6 (right).

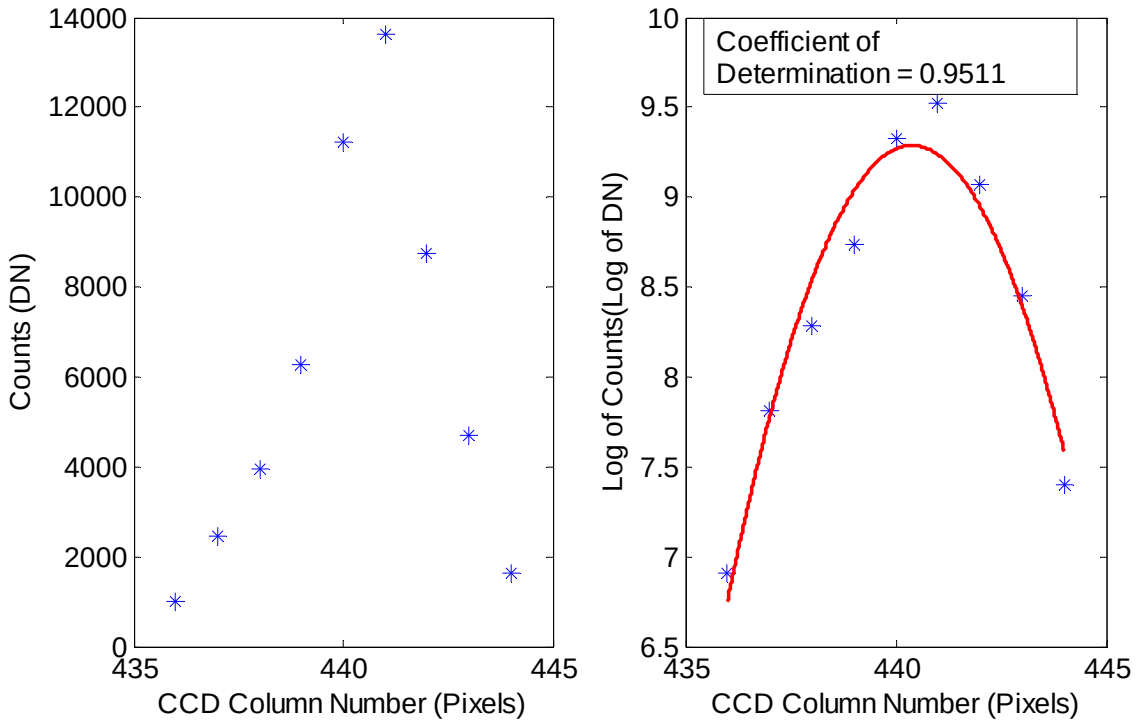

Figure 4.6: Raw image measurement minus background image of 435.84 nm Mercury emission line (left) and the resulting quadratic fit to the log of the peak data (right).

By using this curve fitting method, the coefficient of determination (R^2) can be calculated for all fits. This number shows how well the calculated curve fits the data used to generate the fit on a scale of 0 to 1 with 1 being a perfect fit. This value was calculated using Equations 4.8 – 4.10 and all fits gave a coefficient of 0.9500 or better which implies high confidence in the model.

$$R^2 = 1 - \frac{SS_{res}}{SS_{tot}} \tag{4.8}$$

$$SS_{tot} = \sum_i (y_i - \bar{y})^2 \tag{4.9}$$

$$SS_{res} = \sum_i (y_i - f_i)^2 \tag{4.10}$$

In these above equations, SS_{tot} is the total summation of squares where y_i is each data point and $\bar{y}$ is the mean value of the data points. SS_{res} is the residual summation of squares where f_i is the calculated or fitted value of each data point.

4.3.2 Measurement Collection Technique

In order to produce a large set of spectral emission lines that spans across most of the CCD, five different spectral bulbs were used. Table 4-1 shows the five different bulbs used along with the known wavelengths of the analyzed lines. Note that in the middle and small slit some of these lines are too weak to be used due to low signal in these slits in the allowed exposure times but all lines listed are used in the big slit.

Table 4-1: Spectral bulbs and emission line wavelengths used for calibrations.

Emission Bulb	Analyzed Line Wavelengths (nm)[a]
Cadmium	467.815
	479.912
	508.582
	643.847
Mercury	365.02
	404.66
	435.84
	546.07
Neon	614.306
	633.443
	650.653
	659.895
	667.83
	671.704
	692.947
	703.241
	724.517
Rubidium	780.027
	794.760
Zinc	481.053
	468.014
	472.215
	636.234

[a] Wavelengths listed are from the 85th edition of the Handbook of Chemistry and Physics (*Lide*, 2004).

A standard measurement technique was developed to use for the collection of all wavelength registration measurements. For the original single slit system, and the multi-slit system prior to the installation of the front end optical system, the technique was to take ten successive illuminated images of the emission bulb followed by ten dark images. These ten images are averaged into one image each and then the resulting dark image is subtracted from the resulting illuminated image. This produces one averaged image that has the dark current and DC offset removed. For the multi-slit system registration after the front end optical system installation, a similar technique is used except that with this system in place a shutter exists. This means that instead of having to take ten illuminated images followed by 10 dark images, a sequence of an illuminated image followed by a dark image repeated ten times can be used. Then, each image can be corrected for dark current and DC offset on an image by image basis and then all ten corrected images are averaged together. The validity of this subtraction of a successive dark image was shown in Section 4.1.2. The difference in these two methods is small, and in most cases, produces no difference in the result. However, the use of the shutter reduces error in the removal process as the dark image is taken right after the illuminated image in as close to the same conditions as possible. For both techniques, the emission bulb is measured through a diffusing plate in front of the DM to ensure that the light entering the system will fill the aperture and be uniform across all entrance angles. Once a final corrected image is obtained from the averaging, the fitting of Gaussians to individual peaks begins.

4.3.3 Curve Fitting Technique Criteria and Error Estimation

During the curve fitting process, it became apparent that the maximum signal in the measured emission line peak has an undesired effect on the results of the mean and standard deviation of the fitted Gaussian. Even after a relative calibration is performed, the larger that a peak is allowed to grow on the CCD, the smaller the fitted standard deviation becomes. The reason for

this effect is unknown but is possibly due to differences in pixel sensitivity that cannot be accounted for in a relative calibration. In order to limit the effects of this issue on the results, each peak is measured such that the maximum peak value is the same in every measurement. This maximum value was arbitrarily chosen to be ¾ full well or 12000 DN counts. This value also provides enough signal that the signal-to-noise ratio is not a concern. A second issue that arose while using the curve fitting process is that choosing different points, or pixels, on the measured peak changes the results of the fitted Gaussian parameters. This means that a criterion needs to be developed for how to select points on the peak to be fitted. The developed method is to choose the points that yield the best fit (highest R^2 value) regardless of how many points are incorporated as long as the highest value pixel and the two adjacent pixels to it are included. This means that for some of the fits, only three pixels are used, while for other fits, up to 9 pixels are used.

Using this criterion for the fitting process also introduces a method for determining the error on the mean value of the Gaussian. To get an error value, more, or less points are chosen to perform the fitting method on and the resulting mean is calculated for all combinations chosen. Then, the highest and lowest values for the mean peak value are recorded. The difference of these values from the mean value determined with the highest R^2 value is taken. The larger of the two differences is the estimated error in the fitting method for the peak being examined.

4.3.4 Single Slit Wavelength Registration Results

The above described measurements were acquired and curves were fit for the original single slit system. The results of the fitting technique for the usable emission lines previously listed are shown in Figure 4.7 in red. The blue line is the function fitted to these data points that is then applied to the CCD pixels to provide a wavelength registration.

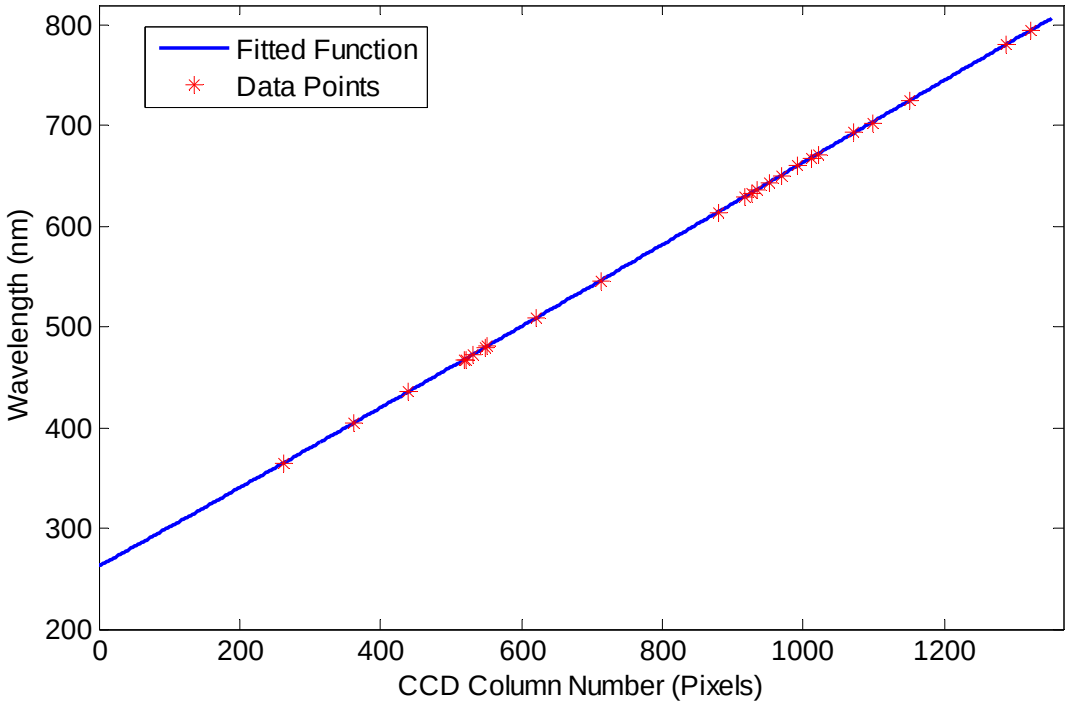

Figure 4.7: Wavelength registration fitted peak positions and cubic fit for the single slit system. The x-value is the fitted peak position and the y-value is the known wavelength. Error bars on the peak position are too small to see and range from 0.2 to 0.4 nm.

The fitted line agrees very well with the fitted peak position points. Although the fit is quite linear, a cubic function was used to capture small variations across the spectral range. The fit result is given in Equation 4.11 where x is the CCD column pixel number and λ is the wavelength in nanometers.

$$\lambda = -8.698\text{x}10^{-9}x^3 + 2.433\text{x}10^{-5}x^2 + 0.3857x + 262.0 \quad (4.11)$$

4.3.5 Multi-Slit Wavelength Registration Results

After the installation of the new multi-slit design into the DM, the wavelength registration was repeated. The same methods and emission lines used for the single slit registration were applied again for the multi-slit system on each slit individually. This results in three different wavelength registrations. The primary reason for three separate registrations is that the slits on the slit plate

are designed to be separated on the CCD in the vertical (spatial) dimension but are also designed to be offset from one another in the horizontal (spectral) dimension. For a description of the multi-slit design, see *Kozun* (2015). This means that each slit will illuminate different column pixels on the CCD with different wavelengths and will thus cover a slightly different wavelength range. Therefore, each column pixel in each slit will have a different wavelength and the difference may or may not be a simple constant offset amount which is why each slit must have its own wavelength registration. Figure 4.8 shows the resulting pixel positions for the measured lines for all three slits and the associated fitted functions.

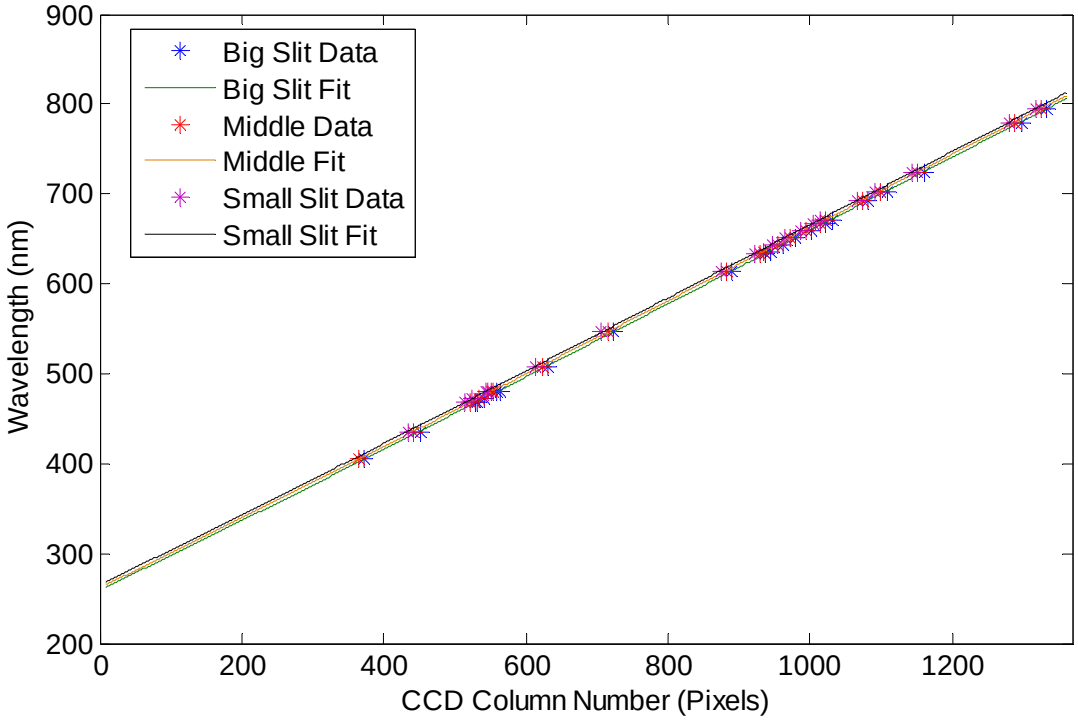

Figure 4.8: Wavelength registration fitted peak positions and fitted curves for all three slits. Error bars on the fitted peak position are too small to see as they range from 0.2 to 0.4 nm. Errors on the peak wavelengths are negligible.

As with the single slit results, the fitted functions agree well with the fitted peak positions and all fitted lines appear to be close to linear. The error range listed for the peak positions were

calculated using the maximum and minimum Gaussian fit method described previously in Section 4.3.3. The fitted functions are again cubic functions.

$$\lambda\_big = -10.46\text{x}10^{-9}x^3 + 2.888\text{x}10^{-5}x^2 + 0.3862 + 258.8 \quad (4.12)$$

$$\lambda\_mid = -9.606\text{x}10^{-9}x^3 + 2.662\text{x}10^{-5}x^2 + 0.3838x + 261.7 \quad (4.13)$$

$$\lambda\_small = -7.614\text{x}10^{-9}x^3 + 2.720\text{x}10^{-5}x^2 + 0.3868x + 264.5 \quad (4.14)$$

Again, as in the single slit case, the cubic and quadratic terms are very small and the fitted equations are almost linear. In comparing these three results to the result of the single slit, two key similarities are noticed. First, the coefficients of the lines are all very similar except for the constant term. This is to be expected as changing the width and position of the slits should not change the relative distribution, or rate of change, of wavelengths on the CCD. Secondly, it is clear in the constant term that each slit will have a different wavelength range and from Figure 4.8, the offset of the slits can be seen in the separation of the fitted lines. The wavelength shift between the fitted functions is shown in Figure 4.9. These curves show that there is not a simple constant offset between the fitted wavelength registrations for each slit. These curves are also subject to error in the fitting method and thus the true offset may be much closer to or farther from a single constant offset value. The maximum error, reported previously, of the peak position results was +/- 0.4 nm. With an error of this size, it can be seen in Figure 4.9 that the true offset value could be a constant value within error. The true offset value will be a result of the slit plate manufacturing and the accuracy and precision to which the slits were cut. The important conclusion to draw here is that the slits are spectrally separated as was expected from the design.

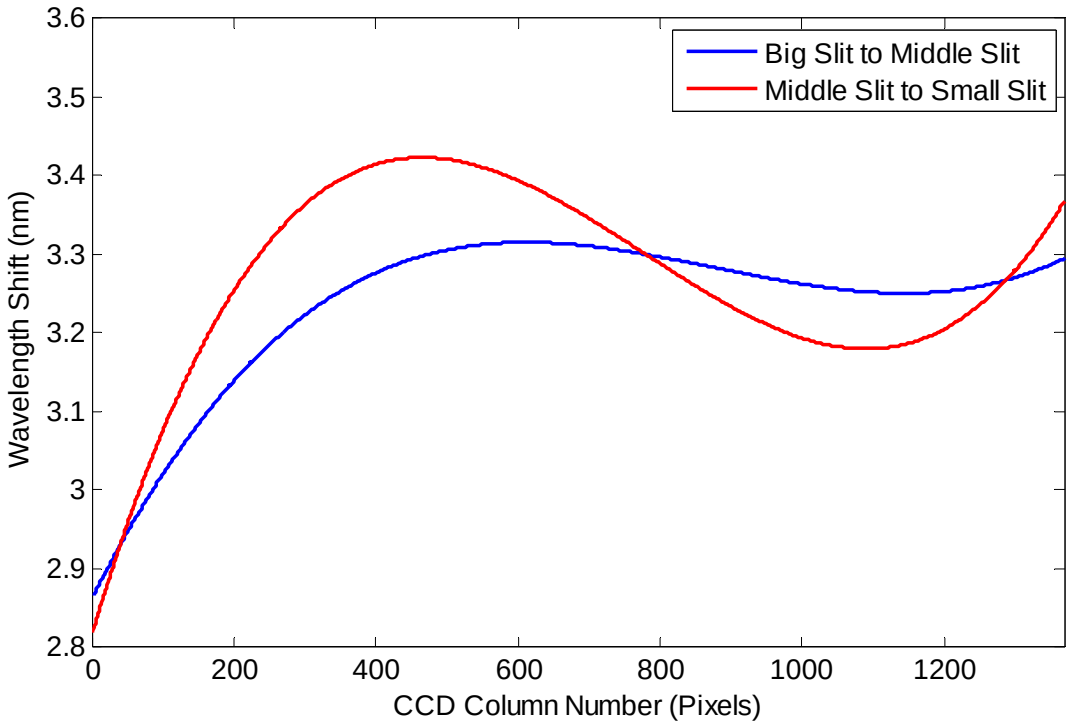

Figure 4.9: Wavelength shift between fitted functions for the transition from big slit to middle slit and from middle slit to small slit.

In order to check the validity of the wavelength registration, a residual analysis on the fitted functions is performed. This involves using the fitted equations to predict the peak wavelength at every fitted peak pixel location. Then, the predicted peak value is subtracted from the known peak value to produce a residual value. The results of this analysis are plotted in Figure 4.10 for all three slits. The residual values are centered on a difference of 0 nm and the maximum difference is around 0.2 nm which is within the maximum error of 0.4 nm reported previously. Thus the wavelength registration is verified.

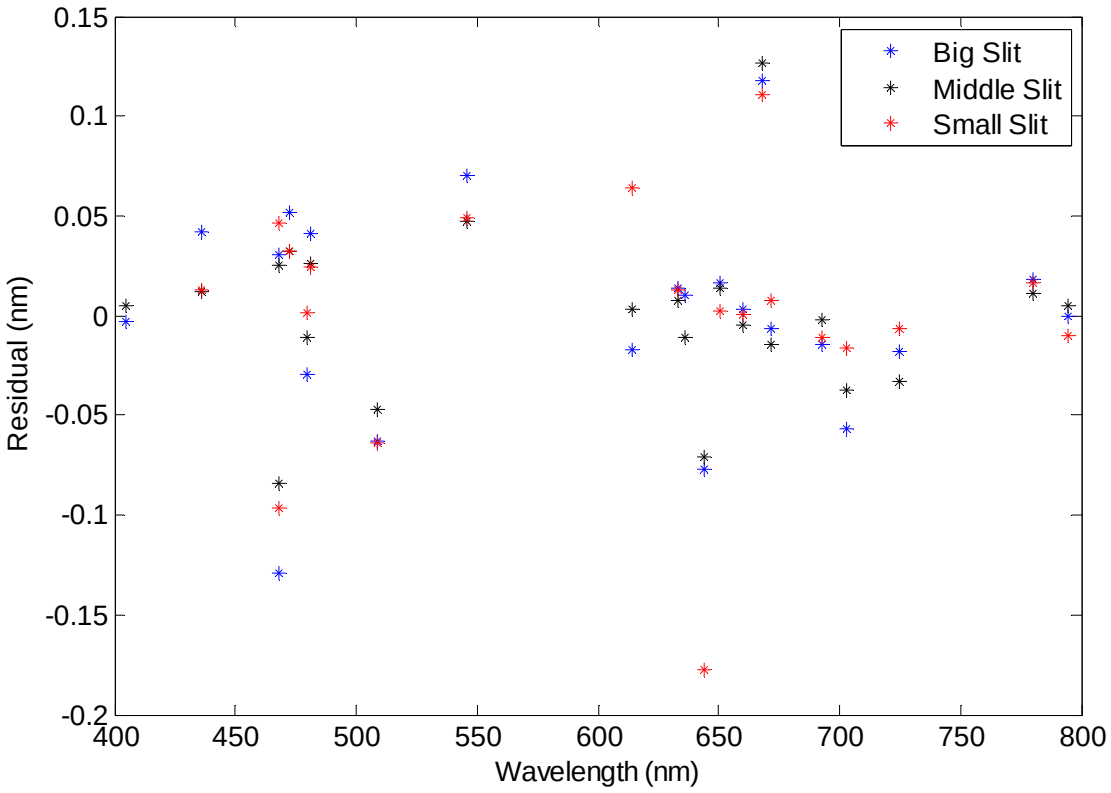

Figure 4.10: Residual analysis of known wavelengths minus fitted wavelengths for all three slits for the pre front end optical system wavelength registration.

4.3.6 Addition of Front End Optical System

The next step in the development of the instrument is the installation of the front end optical system that was built by, and is discussed in, *Kozun* (2015). This system consists of a front end baffle system, a scan mirror and a shutter in front of the DM aperture. With the introduction of new optical elements to the system, the calibrations need to be performed again to check for any changes these new elements may introduce. In terms of the wavelength registration, it is expected that this new system will have essentially no effect. However, the shutter eliminates any blurring of the signal on the CCD when the rows are clocked through the CCD as they are now clocked through in darkness (shutter closed). Figure 4.11 shows the difference between the previous registration and the new registration measured with the full system instrument.

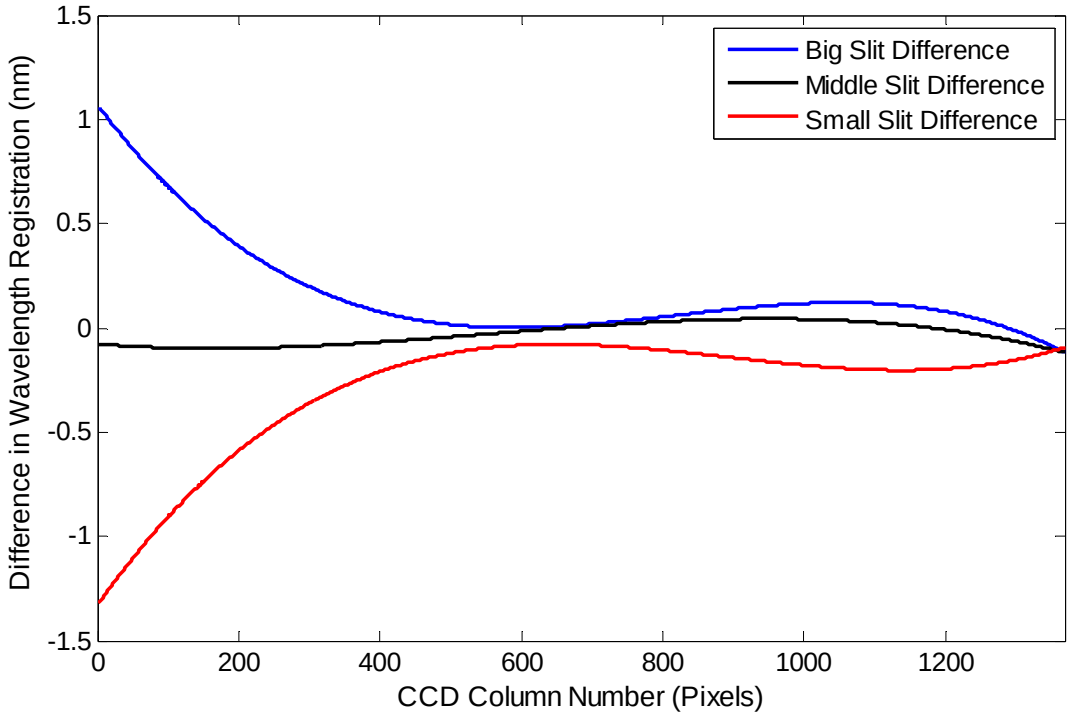

Figure 4.11: Difference in wavelength registrations for each slit (pre scan mirror and baffle system integration – post scan mirror and baffle system integration).

The differences in the registrations are small but substantial enough that they warrant the implementation of a new registration. The larger differences of around 1 nm are in an area of the CCD that is challenging to properly calibrate and later on, only calibrations and measurements above 300 nm will be used. Details and justification of this will be discussed in Chapter Five, but for now, these larger differences below column pixel 200 are irrelevant. The new wavelength registration is found using the same method described previously in Section 4.3.1 and is characterized by the following equations.

$$\lambda\_big = -8.079\text{x}10^{-9}x^3 + 2.300\text{x}10^{-5}x^2 + 0.3864x + 257.7 \quad (4.15)$$

$$\lambda\_mid = -9.026\text{x}10^{-9}x^3 + 2.565\text{x}10^{-5}x^2 + 0.3840x + 261.7 \quad (4.16)$$

$$\lambda\_small = -9.748\text{x}10^{-9}x^3 + 2.770\text{x}10^{-5}x^2 + 0.3821x + 265.8 \quad (4.17)$$

In order to verify the accuracy of the new registration, a residual analysis is performed and the results are shown for all three slit in Figure 4.12. This figure shows that the residual values are centered on 0 which is expected and desired. It also shows that the maximum difference of 0.2 nm is well within the maximum error tolerance value of 0.4 nm which remained unchanged in the new analysis. Therefore, the new registration is valid within experimental error for the measured emission wavelengths.

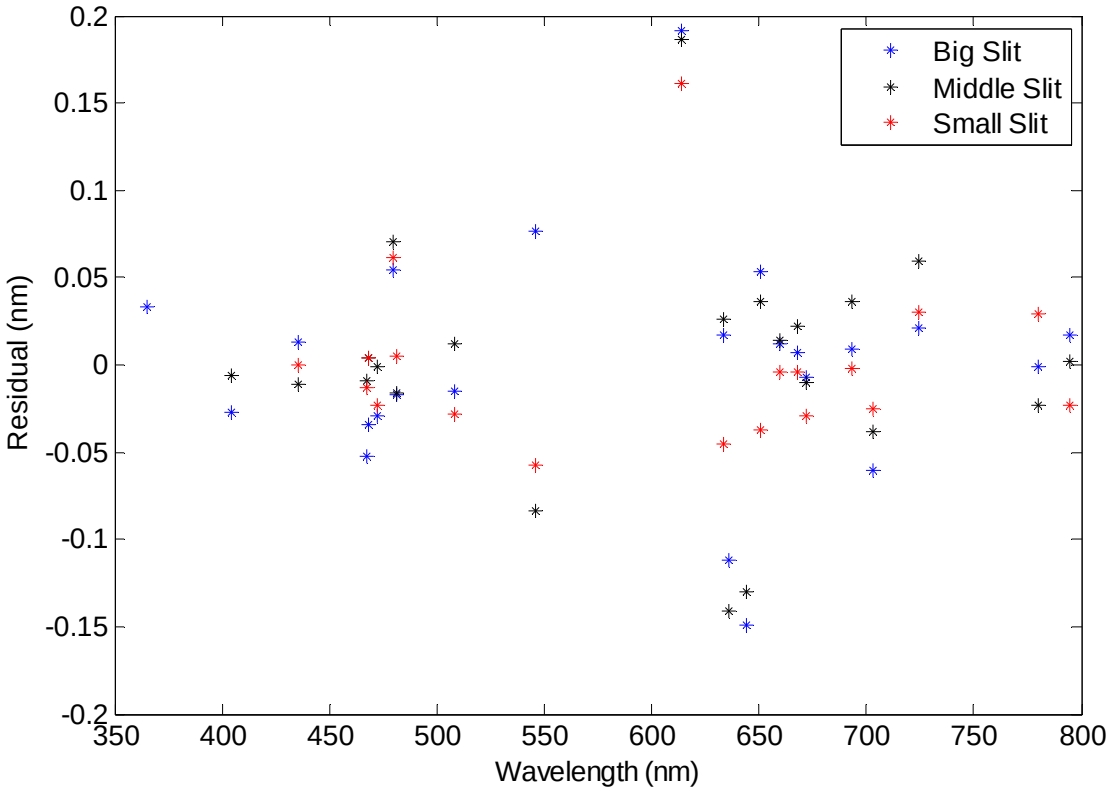

Figure 4.12: Residual analysis of known wavelengths minus fitted wavelengths for all three slits for the post front end optical system wavelength registration.

4.3.7 Addition of New Aperture Stop

Prior to the balloon launch, it was discovered by *Kozun* (2015), that the entrance aperture of the DM would allow too much light to enter the system for the exposure times that could be implemented with the new shutter system. This meant that the amount of incoming light needed

to be reduced for flight. In order to achieve this, a new and smaller aperture stop was designed and installed. The design of this modification can be found in *Kozun* (2015). Thus the optical system was changed again and needed to be recalibrated or verified that the new addition did not change the current calibrations. Due to the reduced amount of light entering the system, not all of the emission lines were strong enough to be used in the new registration especially in the small slit. Even with this new constraint it is expected that the wavelength registration will be unaffected by the new aperture stop. Therefore, instead of performing another registration with less data points in the small slit, a verification of the existing registration will be attempted. To verify the registration, the images from the new aperture stop will be analyzed using the same method for all wavelengths strong enough to be used. Then, the new fitted peaks will be subtracted from the old fitted peaks and if the differences are centered on 0 nm within error, the current registration will be verified. Figure 4.13 shows the results of the verification difference for all three slits. The differences above 600 nm are close to what was expected as they are centered on a difference of 0 nm within error with the exception of a few points. However, the differences below 600 nm are up to 1 pixel. These results suggest that the new aperture stop did in fact change the wavelength registration and a recalibration is required.

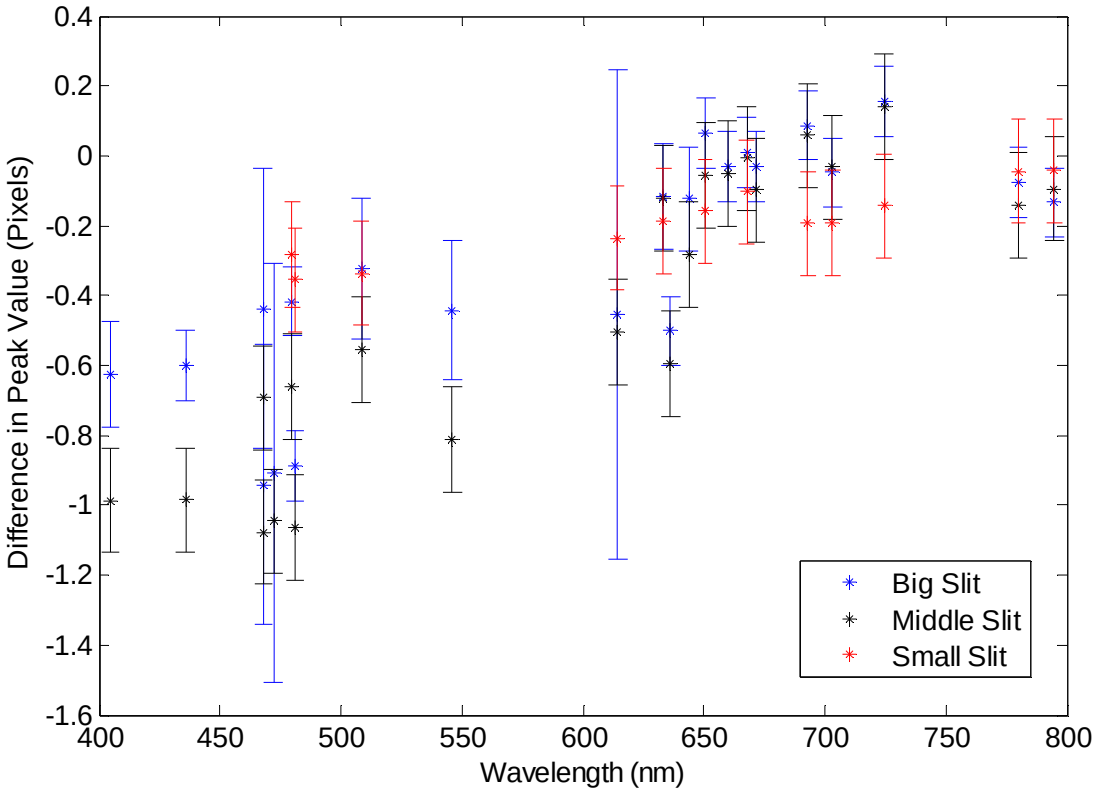

Figure 4.13: Fitted peak position verification results (pre aperture stop peaks – post aperture stop peaks).

Before performing the new wavelength registration, a comparison of the emission bulb measurements pre and post aperture stop installation was performed to see how the peaks changed or were shifted. Figure 4.14 shows this comparison for one spectral line measured peak. This plot shows no evidence of a shift in the peak position as predicted. However, due to the new peak being much narrower, the Gaussian fitting technique may predict different peak positions for the two images. The curve fits for these two measured peaks is shown in Figure 4.15.

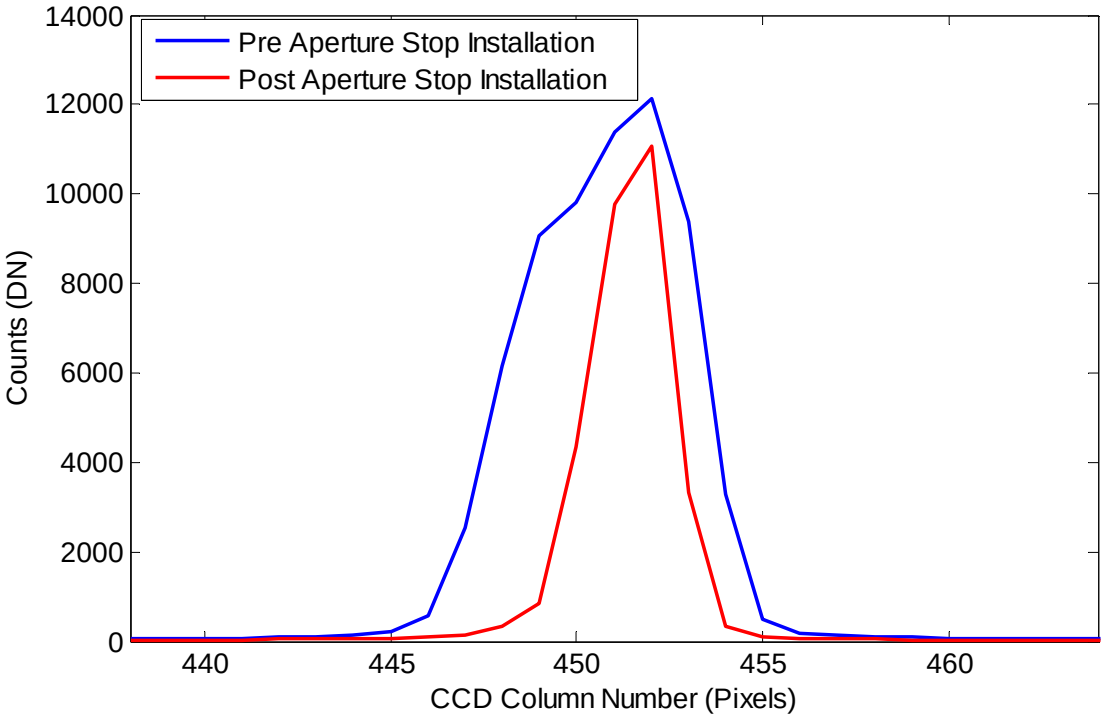

Figure 4.14: 435.84 nm Mercury emission line before (blue) and after (red) installation of the new aperture stop in the big slit.

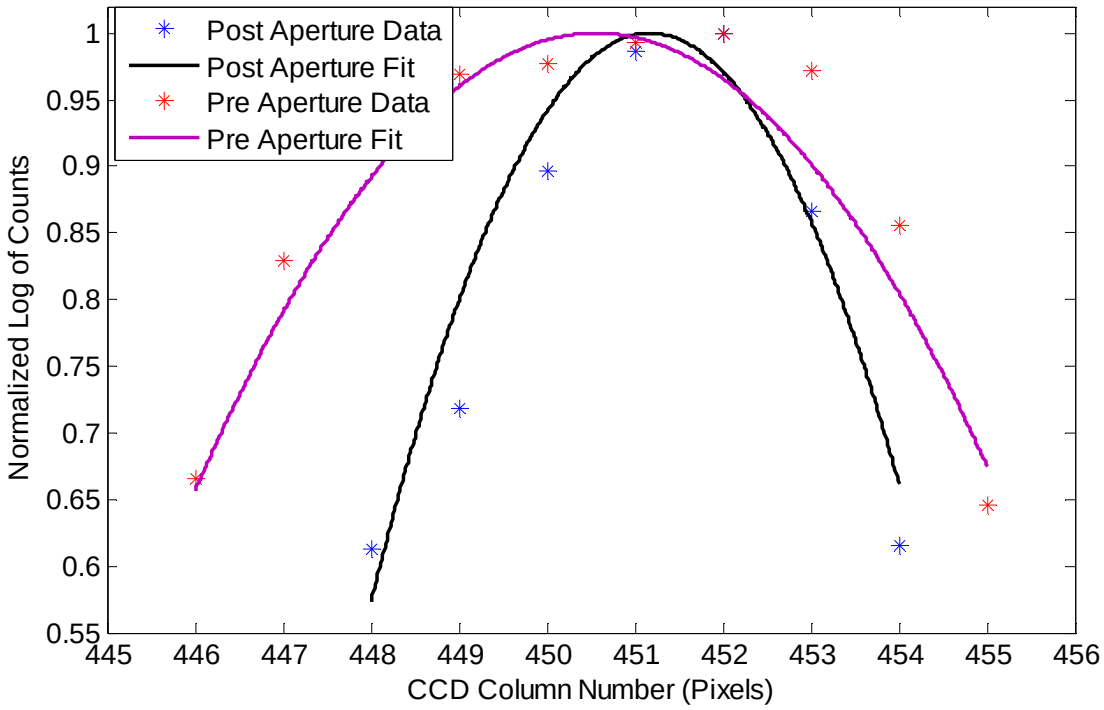

Figure 4.15: Quadratic fits to the log of 435.84 nm Mercury emission line measurements normalized to 1 pre (blue) and post (red) aperture stop.

A new wavelength registration was performed using images acquired with the new aperture stop. As before, a plot of the difference between the existing wavelength registration and the new wavelength registration is shown in Figure 4.16. Note that for the small slit, many of the emission lines were not strong enough to be accurately measured and fitted due to the low measured signal as a result of the small slit size. This resulted in a smaller measurement set to perform the registration. Because of this and the fact that the small width of the small slit made the original measurements have narrower width already, it was decided to simply leave the wavelength registration of the small slit unchanged. The difference analysis (Figure 4.13) also supports this choice as the differences in the small slit were the smallest and closest to a difference of 0. Therefore the original fit is accurate enough to keep the registration unchanged.

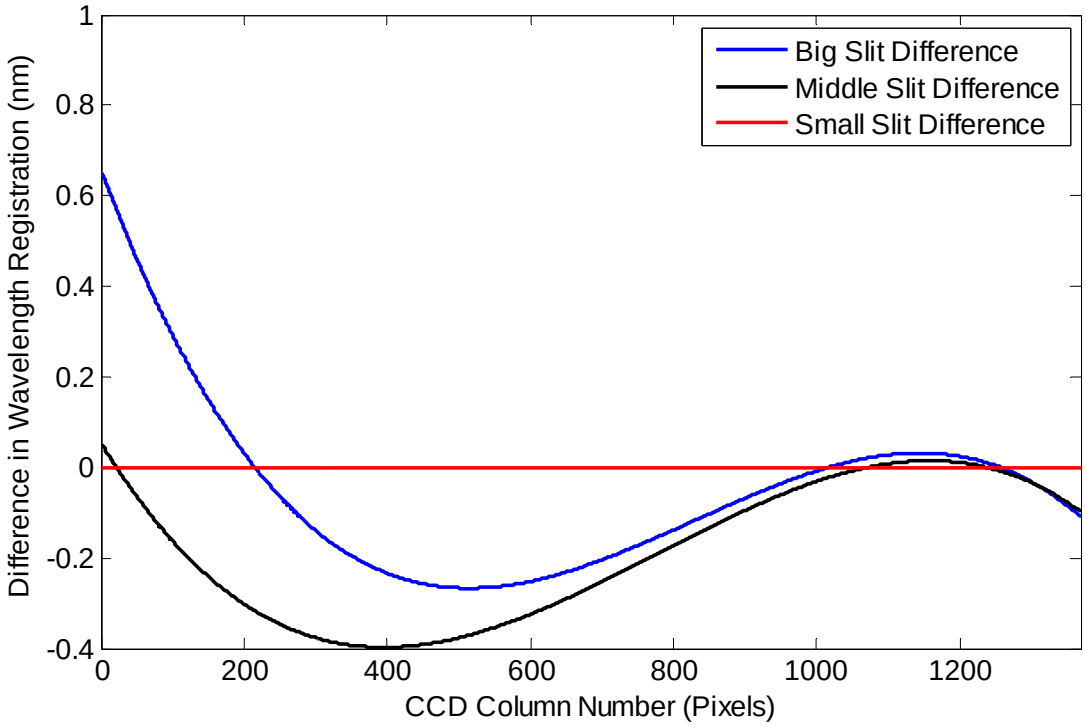

Figure 4.16: Difference in wavelength registration for all slits (post aperture – pre aperture). Small slit difference is zero because the registration was not changed.

These difference curves for the big and middle slit show that the wavelength registration has not drastically changed in majority of the pixels. The new wavelength registration is given by the following equations, where the small slit is the same as before the aperture stop was installed.

$$\lambda\_big = -10.47\text{x}10^{-9}x^3 + 2.895\text{x}10^{-5}x^2 + 0.3822x + 258.4 \quad (4.18)$$

$$\lambda\_mid = -10.89\text{x}10^{-9}x^3 + 3.000\text{x}10^{-5}x^2 + 0.3815x + 261.8 \quad (4.19)$$

$$\lambda\_small = -9.748\text{x}10^{-9}x^3 + 2.770\text{x}10^{-5}x^2 + 0.3821x + 265.8 \quad (4.20)$$

As with previous wavelength registrations, a residual analysis of the predicted peak positions was performed. The results again agreed within maximum error tolerance and look very similar to Figure 4.12. Therefore a figure of this residual analysis is omitted as results are unchanged.

4.4 Point Spread Function Calibration

4.4.1 Development of the Point Spread Function

The determination of the PSF relies on many of the same assumptions and techniques as the wavelength registration except that it focuses on different parameters. The need for a PSF comes from the assumption that when an infinitesimally narrow spectral line travels through the optical system and hits the CCD, it forms an ideal Gaussian and illuminates a range of pixels. A range of pixels is illuminated because the shape projected onto the CCD is a convolution of the incoming light wave with the square slit. This produces a Gaussian shape whose width is proportional to the slit width i.e. the smaller the slit, the smaller the PSF. The PSF describes the range of pixels that are illuminated by a single wavelength. Due to the Gaussian shape, the PSF value at any wavelength is characterized by the HWHM of a Gaussian curve at that wavelength. The HWHM of a Gaussian can be determined from the standard deviation, σ, using Equation 4.21.

$$HWHM = \sqrt{2\ln(2)}\sigma \quad (4.21)$$

The method for how to determine the standard deviation was discussed in Section 4.3.1. As with the wavelength registration, once a set of HWHM values at different wavelengths have been determined, the values can be used to calculate a fitted equation to describe the point spread at all CCD pixels or wavelengths. The error estimation used for the wavelength registration is also used to estimate the error of the HWHM values.

The measurement sets used to determine the HWHM values are the same sets used for the wavelength registration as both parameters can be extracted from the same Gaussian fits. The PSF requires one more step after retrieving the HWHM value using this method. The method described returns the HWHM values in terms of pixels. However, it is desired to have the HWHM values in terms of nanometers (units of the wavelength registration). To produce a conversion factor from pixels to nanometers, it is assumed that the wavelength registration is close enough to a linear relationship that a linear fit to the fitted peak positions can be made. This means that the slope of this line will have units of nm/pixel which can then be used as the conversion factor for a HWHM in pixels to a HWHM in nm.

4.4.2 Single Slit Point Spread Function Results

The above method was first applied to the measurements from the original single slit system and the resulting HWHM values are plotted in Figure 4.17. The error analysis was performed as described in Section 4.3.3. Due to the uncertainty of the HWHM values themselves, the error bar attached to all wavelengths shown was taken to be the maximum error of any wavelength. This was done to illustrate the maximum error in the method.

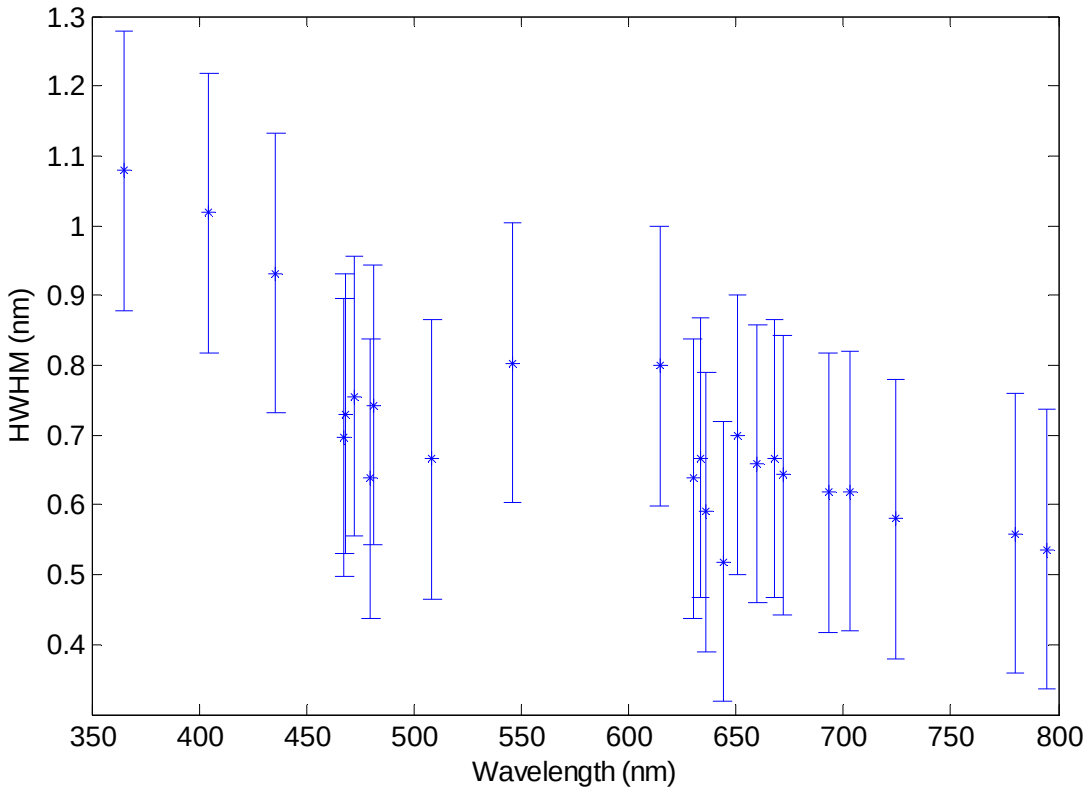

Figure 4.17: HWHM values for original single slit system PSF analysis.

4.4.3 Multi-Slit Point Spread Function Results

After the installation of the new slit plate, the same measurement techniques were employed to measure the same emission lines as with the single slit system. Besides the existence of multiple images, the difference between the expected results for the multi-slit system versus the single slit system is that the multi-slit system should have smaller values for the HWHM at all wavelengths. This is due to the smaller slit sizes used in the multi-slit design. It is also expected that the PSF will change with each of the slits as they are all different sizes. Therefore, when moving from the big slit, through the middle slit and to the small slit, the PSF is expected to decrease at each step. After all images were collected, the same analysis technique was used to produce a PSF for each of the three slits which is shown in Figure 4.18.

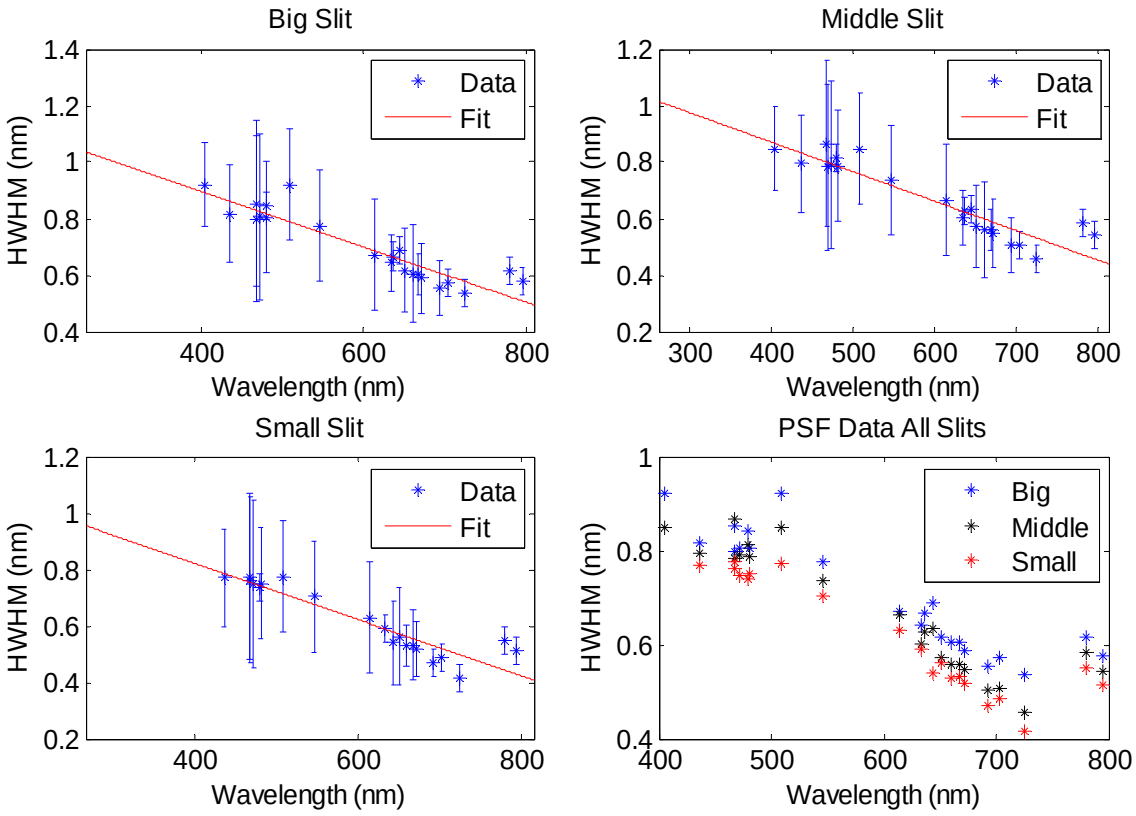

Figure 4.18: HWHM values for multi-slit analysis. Error bars were calculated using the previously described error estimation method. Error bars are excluded from the bottom right plot intentionally for clarity.

The calculated values shown look similar in shape to the fitted values for the single slit. An attempt at fitting a linear equation to the HWHM values was done and is shown in red for each of the three slits. This line unfortunately does not quite fit all the values within error. The cause of this non-linear and non-constant trend is unknown.

The plot in the bottom right of Figure 4.18 shows the HWHM values for all three slits plotted together without error bars. This demonstrates two outcomes that were predicted to occur. First, the overall value for the HWHM is smaller than it was in the single slit measurement which was expected due to the smaller slit sizes. Secondly, at all wavelengths shown, the big slit has the largest values and the small slit has the smallest values with the

middle slit values lying in between. Therefore, this plot verifies the prediction that smaller the slit size, the smaller the resultant point spread values.

4.4.4 Results Post Installation of Front End Optical System

Similar to the wavelength registration, the installation of the front end optical system requires a recalibration of the PSF using the new system to acquire measurements. To show how the HWHM values changed, Figure 4.19 shows the values post system minus the values pre system for each slit as well as a plot overlaying the new values of all three slits (bottom right).

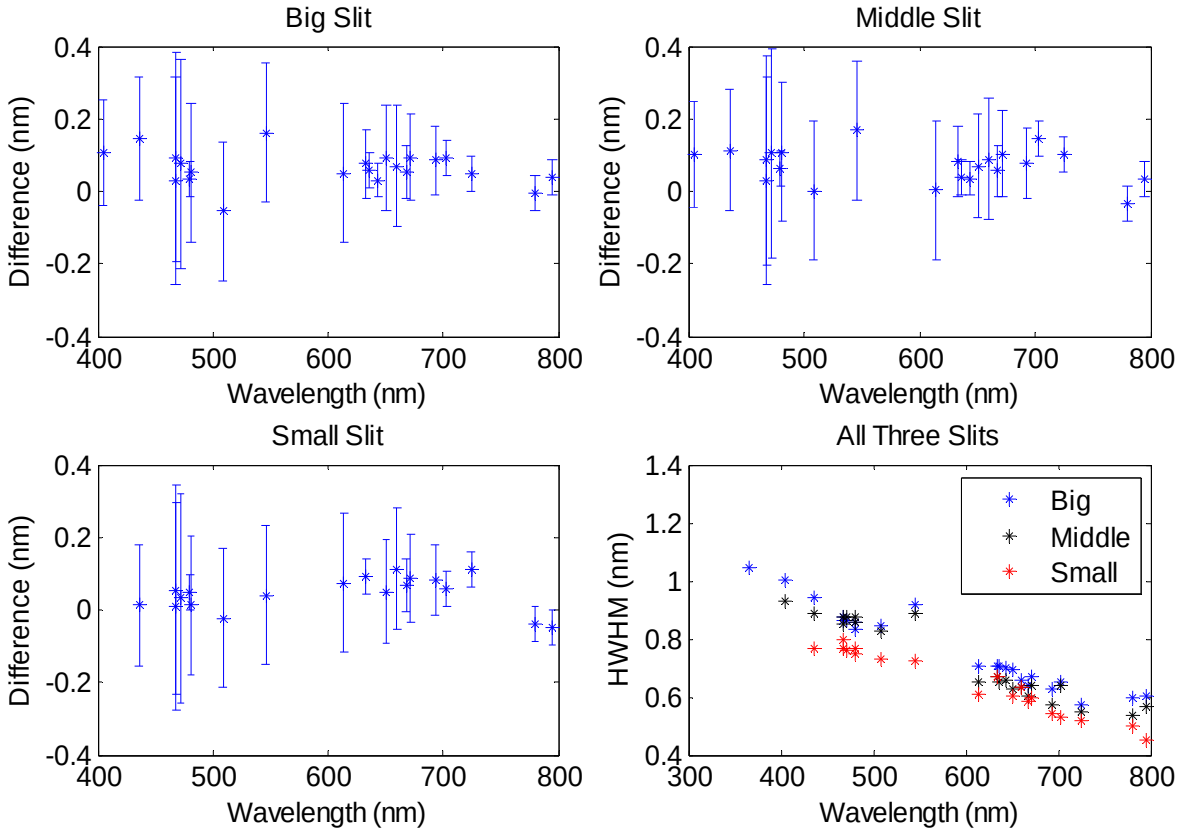

Figure 4.19: Difference of HWHM values between pre and post system installation analysis (post system values – pre system values). Error bars are an average of the errors from the two analyses. Error bars are excluded from the bottom right plot intentionally for clarity.

The results of this analysis show that the HWHM values for all slits are slightly higher with the new system in place. However, from viewing the plots of the individual slits, it can be seen that

almost all of the difference values are 0 within error even if they are all generally higher. Therefore, it can be concluded that the PSF has not changed within error. The second conclusion to draw from Figure 4.19 is shown in the bottom right plot where all three slits are shown without error bars. This plot shows that the big slit still has the highest value at all wavelengths and the HWHM decreases in moving to the middle and small slits as expected. Therefore, the relative trend of the three slits is unaltered with the addition of the front end system.

4.4.5 Results Post Installation of New Aperture Stop

As with the wavelength registration, the addition of the new aperture stop to the system requires the PSF to be reanalyzed with measurements acquired by the new system. The first step is to check the difference between the HWHM values found before and after the aperture stop installation. The results of this difference (before – after) are shown in Figure 4.20.

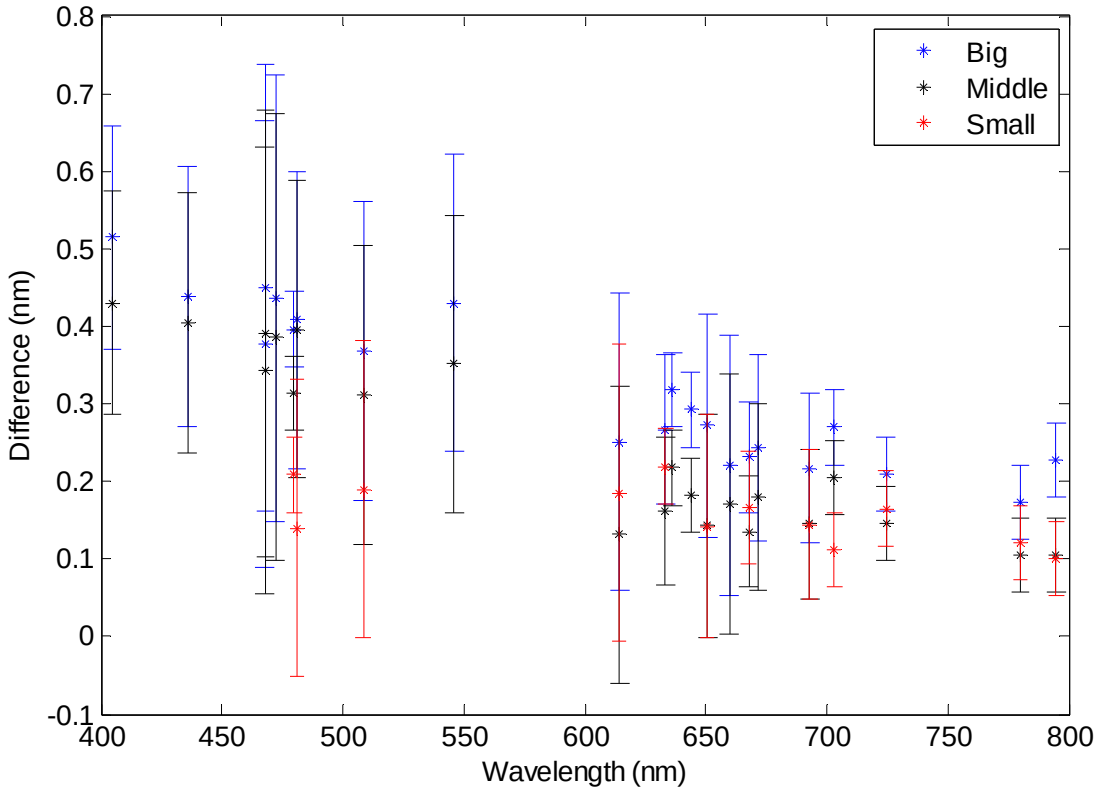

Figure 4.20: Difference of HWHM values between pre and post aperture stop installation (pre – post) for all three slits. Error bars are an average of the errors of the two analyses.

This figure shows that none of the new HWHM values for any of the slits agrees within error with the values found before the installation of the aperture stop. The other point to notice from this figure is that the new HWHM values have decreased by 0.2 to 0.5 nm which is a substantial change. The reason for this is not known. For more information on the effects of the new aperture stop on the PSF and system in general, see *Kozun* (2015). The new values for the HWHM for each slit are shown in Figure 4.21 where the blue points are the measurements and the red line is the average value.

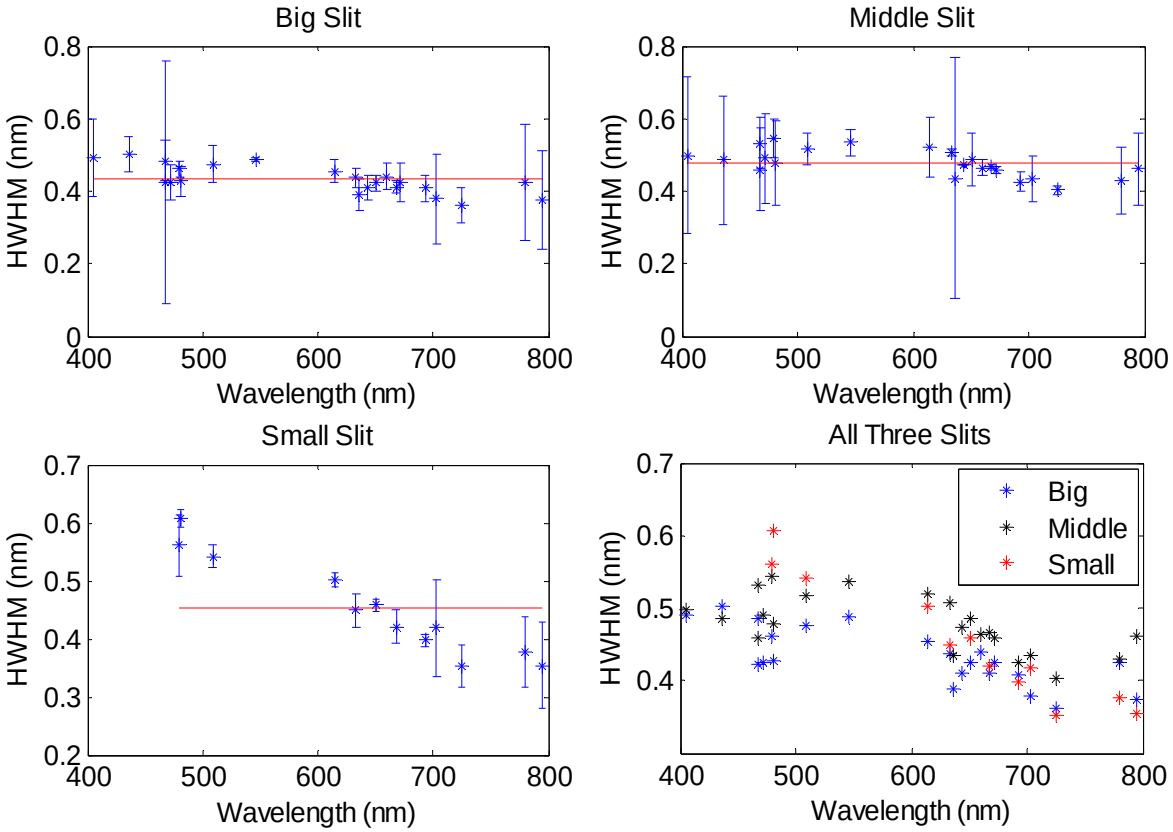

Figure 4.21: Post aperture installation HWHM values for final PSF. Error bars were calculated using the described error estimation method. Error bars are excluded from the bottom right plot intentionally for clarity.

These plots show that the HWHM values are now much closer to a constant value within error and so an average value for all HWHM values in each slit was taken and is plotted over top in

red. This is the result that was initially expected. The bottom right plot shows that the relative relationship between the slit sizes and the PSF values no longer holds. The reason for this effect is also unknown but the results imply that a different optical element, such as the new aperture stop, has becoming the new limiting element or factor in terms of the PSF. Even with the loss of this relationship, the average HWHM value has been determined from this analysis and is used for future data analysis.

4.5 Relative Calibration

The relative calibration is calculated by measuring a broadband source of known spectral response and comparing it to the resulting measured response. In order for this to work properly, the broadband source must be able to fill the entire aperture of the instrument with uniform light. The other requirement of the source is that it must be able to produce measureable signal at all of the wavelengths measured by the CCD. If this is not possible, multiple sources may be able to be implemented and have their results combined into one final calibration. This latter case was performed in this work.

4.5.1 Development of the Relative Calibration Analysis

To relatively calibrate the DM, a National Institute of Standards and Technology (NIST) calibrated Tungsten bulb that is available in the laboratory was measured and the resulting spectrum was compared to the known spectrum. The signal measured from this bulb becomes very low in the UV spectral range because the UV light from the Tungsten filament is absorbed by the glass casing. This means that for wavelengths below 400 nm there is not enough measured signal present to be used in a relative calibration. In order to increase the signal in this region so that a relative calibration can be performed below 400 nm, a second Tungsten bulb was used. The casing of the second Tungsten bulb is quartz glass that is transparent to the UV spectral range. Therefore this bulb will provide stronger signal below 400 nm than the calibrated bulb.

However, the second bulb is not calibrated, i.e. it does not have a known spectrum. In order to develop a known spectrum, the Tungsten bulb was modelled as a black body radiator as follows.

The starting equation is the equation for the spectral emittance ($E_{ph}(\lambda, T)$) of a blackbody radiator in SI units (photons/s/m^2/m) which will produce the reference curve for the second bulb.

$$E_{ph}(\lambda, T) = \varepsilon(\lambda, T) * \frac{2\pi c}{\lambda^4} * \frac{1}{e^{hc/\lambda kT} - 1} \tag{4.22}$$

In this equation, $\varepsilon(\lambda, T)$ is the wavelength and temperature dependent emissivity of the material, in this case Tungsten, c is the speed of light, λ is wavelength, T is temperature, h is Planck's constant, and k is the Boltzmann constant all in SI units. In order to apply this equation to the bulb used for the UV side of the relative calibration, the operating temperature as well as the emissivity of Tungsten at all measured wavelengths must be known. There was no direct method available to measure the operating temperature of the bulb, and so the temperature used for this model is 3300 K which is a standard operating temperature for a Tungsten bulb. The emissivity function for the wavelengths measured by the DM is fitted to a data set reported by *Forsythe et al.* (1925) and used by *Kosch et al*. (2003) to perform similar calculations. This data set and fitted function is shown in Figure 4.22 in the top left plot. With this curve and the operating temperature known, they can be used with Equation 4.21 to produce a known blackbody curve for the Tungsten bulb that is shown in Figure 4.22 in the top right plot.

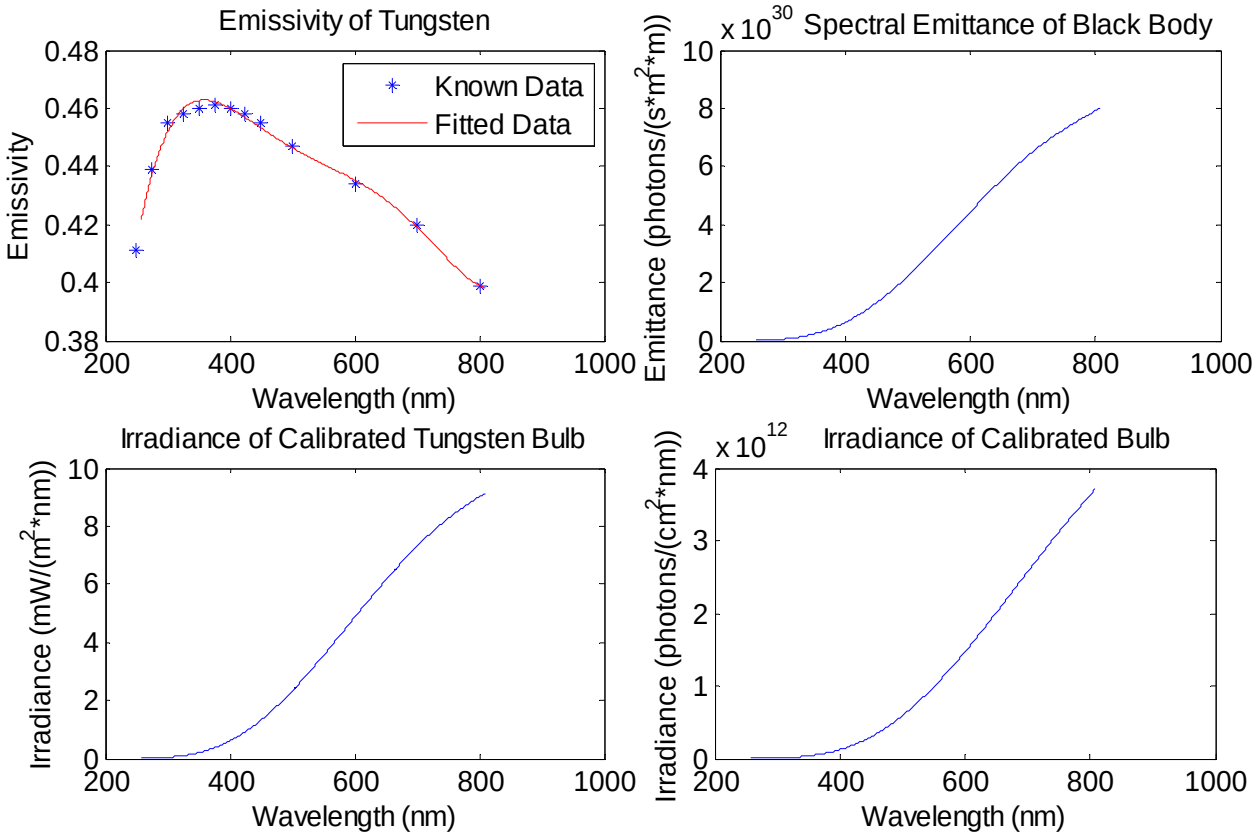

Figure 4.22: Development of the known spectral curves for the two Tungsten bulbs. Top left is fitted function for emissivity of Tungsten, top right is the blackbody curve for Tungsten at an operating temperature of 3300K, bottom left is the given irradiance curve for the calibrated Tungsten bulb and bottom right is the calibrated Tungsten irradiance curve in desired units.

Figure 4.22 also shows the given curve for the calibrated Tungsten bulb used for the relative calibration above 400 nm in the bottom left. This curve is given in units of $mW/m^2/nm$ and was converted to the units that are used for this instrument calibration which are $photons/cm^2/nm$. This converted curve is shown in the bottom right of Figure 4.22 and will be used for the relative calibration for images acquired with the calibrated bulb. This curve is still slightly different than the calculated blackbody curve in that the calibrated curve is an irradiance curve and the blackbody curve is an emittance curve. The difference between these two curves is insignificant for a relative calibration as it is only the relative spectral response that matters and this attribute

is the same for the two curves. This is because both curves are in units of photons/nm which is the defining unit in terms of spectral response. These curves can now be normalized to 1 at any pixel required to show relative growth of the spectrum and be used as the known curves in the relative calibration.

4.5.2 Relative Calibration Measurement Collection

With the known curves developed, the next step is to image the two bulbs and extract a single spectrum for each slit from the image using the usable pixel averaging method. Unlike the wavelength registration and PSF, the relative calibration was not performed on the single slit system or the multi-slit system without the front end system. The first relative calibration measurements and analysis are performed for the multi-slit system with the front end optical system attached. To ensure that the incoming light from the Tungsten bulb is uniform and fills the entire aperture, the Tungsten bulb is measured through a diffusing plate in front of the DM. It is assumed that the spectral transmission of the diffusing plate is constant over all desired wavelengths. Both Tungsten bulbs were placed 50 cm away from the DM aperture and were measured using the same technique as the previous calibrations. Any measurement that is used for a calibration is the average of ten images that are corrected by the removal of a dark image acquired directly after the illuminated image. Figure 4.23 shows a Tungsten spectrum from the big slit along with the known calibrated bulb spectrum. Both curves are normalized at 400 nm. The big slit spectrum is representative of the spectra in the middle and small slit and so the spectra for these slits are not displayed.

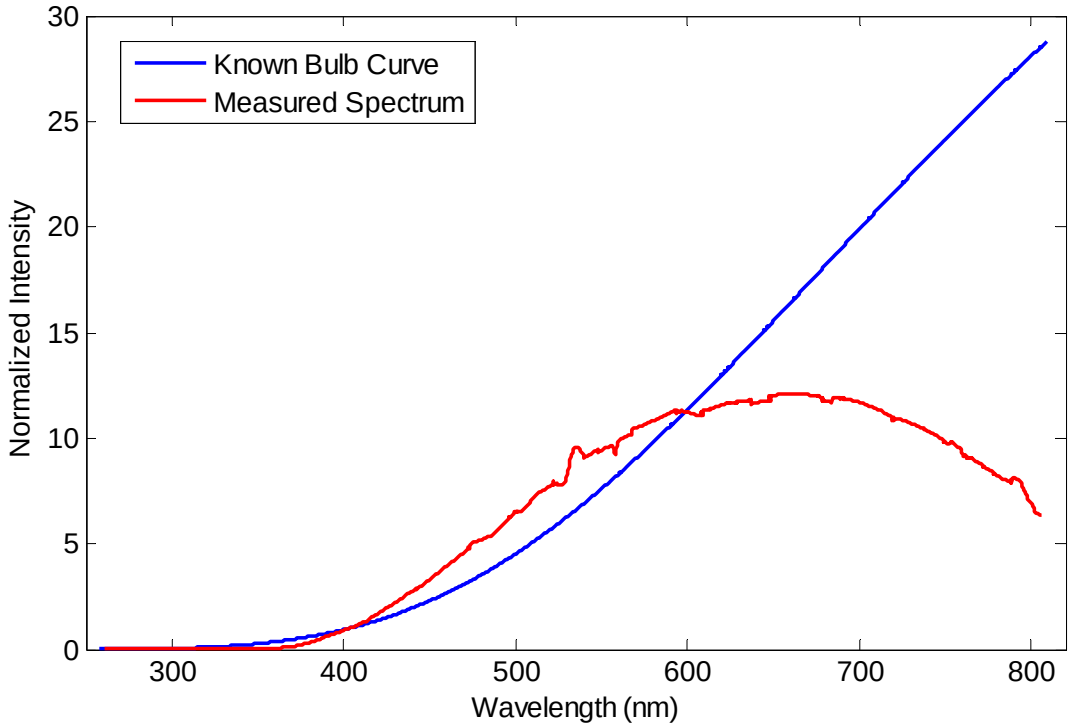

Figure 4.23: Calibrated Tungsten bulb measured spectrum and known curve both normalized at 400 nm.

The features in the measured spectrum shown in Figure 4.23 above 550 nm are due to the discrete nature of the usable pixel averaging method and are not a concern as they will be calibrated out of the final data product with the relative calibration. The other noticeable feature in the data is the curved feature just below 550 nm. This is due to the positioning of the order sorting filter in front of the CCD. It is around this wavelength where the order sorting filter, which is physically glued onto the FOP, begins. Therefore, there are known issues that exist here due to the dramatic change in the FOP surface. Recall that the purpose of this order sorter is to block higher order diffracted light from below 550 nm from interacting with the CCD pixels corresponding to wavelengths above 550 nm. Again, this feature will be calibrated out, or at least reduced, with the relative calibration.

The blue line in Figure 4.23 is the known spectral response of the calibrated bulb obtained from the product data sheet. Therefore, this is what the measured response (red line in Figure 4.23) should produce in a perfect system. The relative correction is used to correct for this difference in the measured response by applying a multiplicative factor to the measured spectrum. To achieve this correction factor, the ratio of the known curve to the measure curve is taken on a pixel by pixel basis and this becomes the relative calibration. Figure 4.24 shows relative calibration curves achieved from only the calibrated bulb measurements for all three slits at varying exposure times in each slit. The reason for plotting multiple curves at varying exposure times together is to ensure that the relative calibration curves are independent of exposure time. If they are independent, all pixels at any exposure time that do not saturate the CCD should overlap.

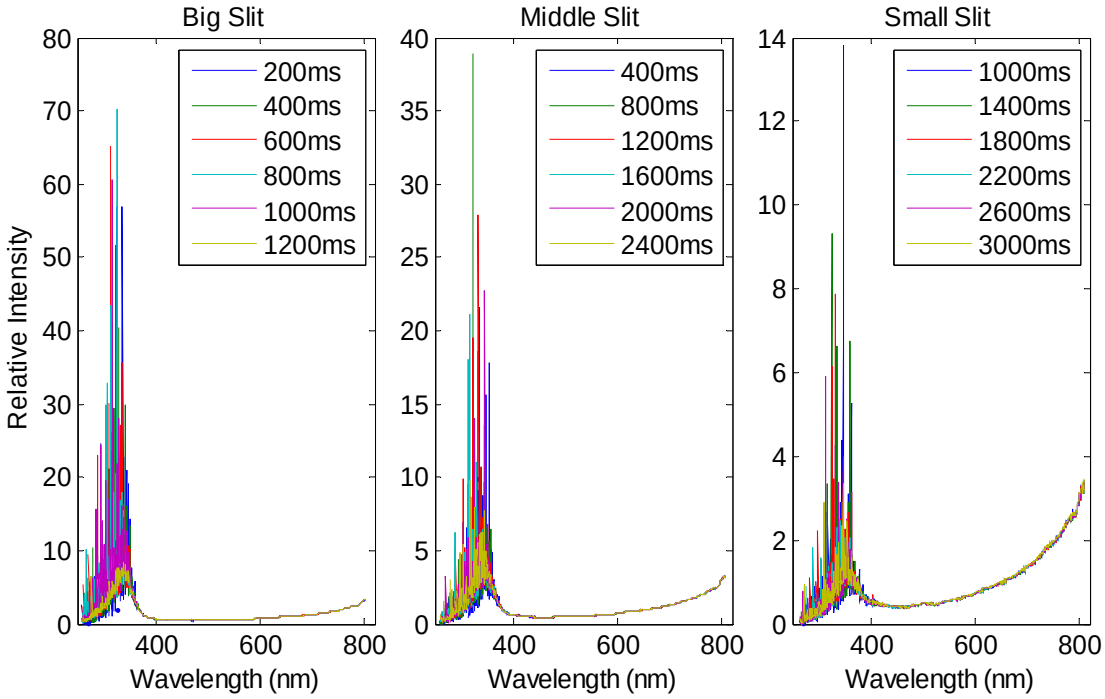

Figure 4.24: Relative calibration curves using the calibrated bulb measurements for all three slits at varying exposure times to demonstrate that the calibration is independent of exposure time.

Two main conclusions can be drawn from Figure 4.24. First, below 400 nm, the curves exhibit a large amount of noise. This is because the calibrated bulb signal becomes very low in this spectral range which lowers the signal to noise ratio. This is the reason that a second bulb was used to get better results below 400 nm. The second conclusion is that for data above 400 nm the relative curves land essentially right on top of one another which is the expected result. A close up of the data past 400 nm is shown in Figure 4.25 to better illustrate the agreement of the curves and thus the exposure time independence. Therefore, the relative calibration is indeed independent of exposure time. Besides verifying that the relative calibration can be applied to measurements recorded at any exposure time, the exposure independence allows the use of two different calibration spectra to be used and merged together even if they are measured at different exposure times. As long as the measurements being used do not saturate the CCD in the desired region, the relative calibration will be valid.

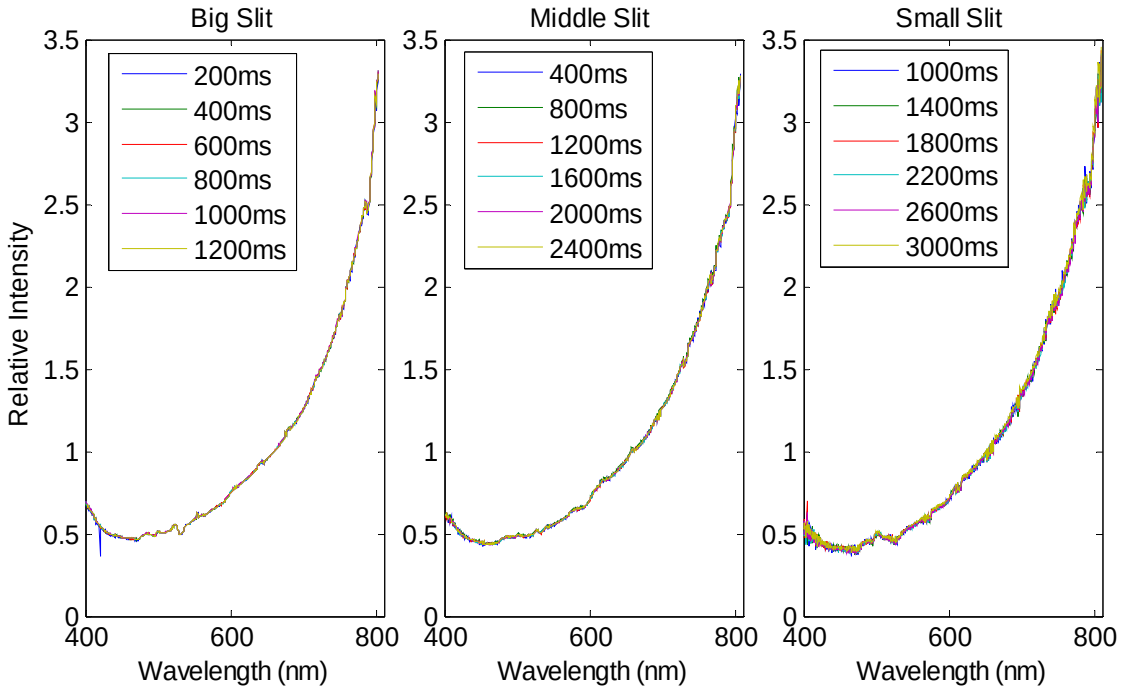

Figure 4.25: Close up of Figure 4.24 to clarify the illustration of the agreement of the relative curves past 400 nm for varying exposure times to exhibit exposure time independence.

4.5.3 The Relative Calibration Curves

With the independence of exposure time verified, the next step is to produce two relative calibration curves for each slit: one for each bulb. These two curves can then be normalized to a common point around 400 nm and joined together to create one relative calibration curve for each slit. Even with the increased signal levels below 400 nm due to the UV bulb, the signal levels were still too low below 300 nm. Therefore, the relative calibration is only valid above 300 nm for all three slits and all further analysis will only deal with wavelengths above 300 nm. The final relative calibration curves are shown in Figure 4.26.

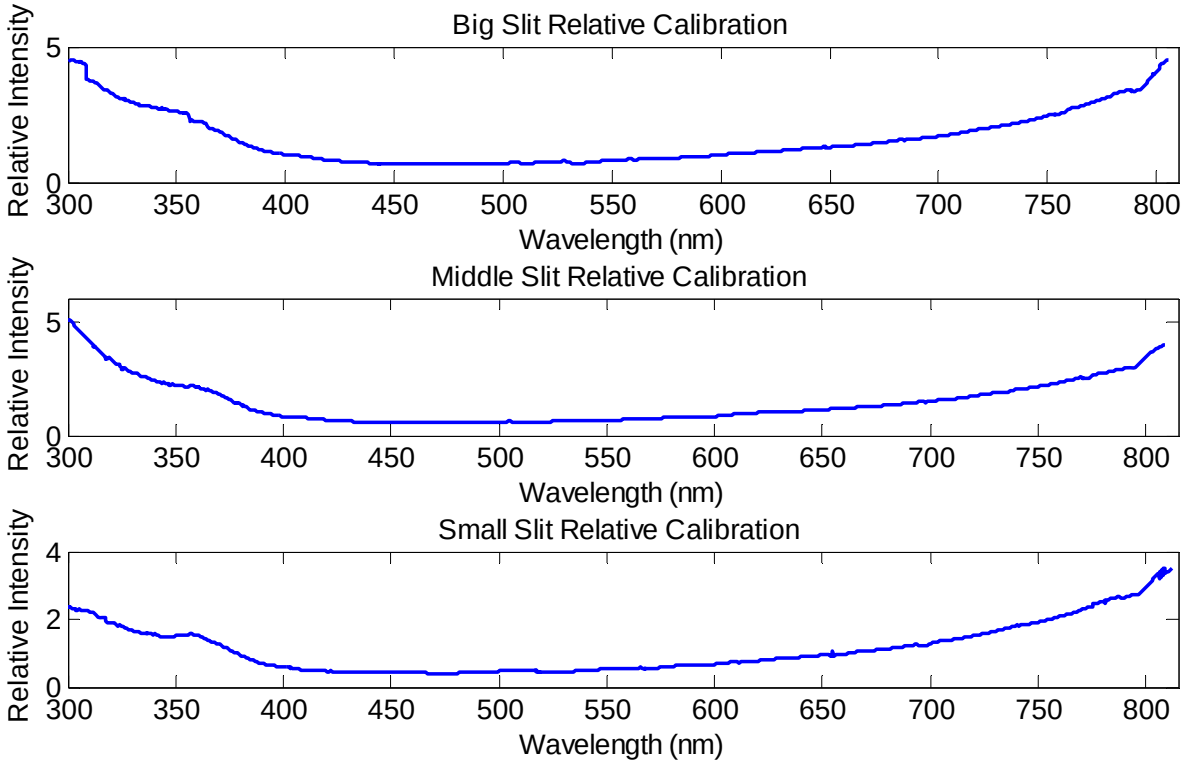

Figure 4.26: Final relative calibration curves after the removal of data below 300 nm for each slit.

All of the relative curves are fairly similar to each other in shape which was expected as all of the CCD pixels should behave similar to each other. Also, the light from each slit travels through the exact same optical chain and thus encounters the exact same optical effects. The square like

features in the curves are due to the discrete nature of the usable pixels and are there to compensate for the similar features observed previously in the measured Tungsten spectrum.

4.5.4 Effect of New Aperture Stop on Relative Calibration

As before, the introduction of the new aperture stop to the system requires recalibration or verification of the current calibration. The installation of the new aperture stop is not expected to make any changes to the relative calibration. In order to verify this, measurements were taken of the same bulbs in order to redo the calibration and show that it is unchanged. However, two issues were encountered in attempting to retrieve these measurements with the new system. The first issue that developed was the appearance of a fringing pattern on the relative calibration curve and in the Tungsten image itself. This high frequency wave-like pattern was most dominant above 700 nm. Figure 4.27 shows a Tungsten image before and after the installation of the new aperture.

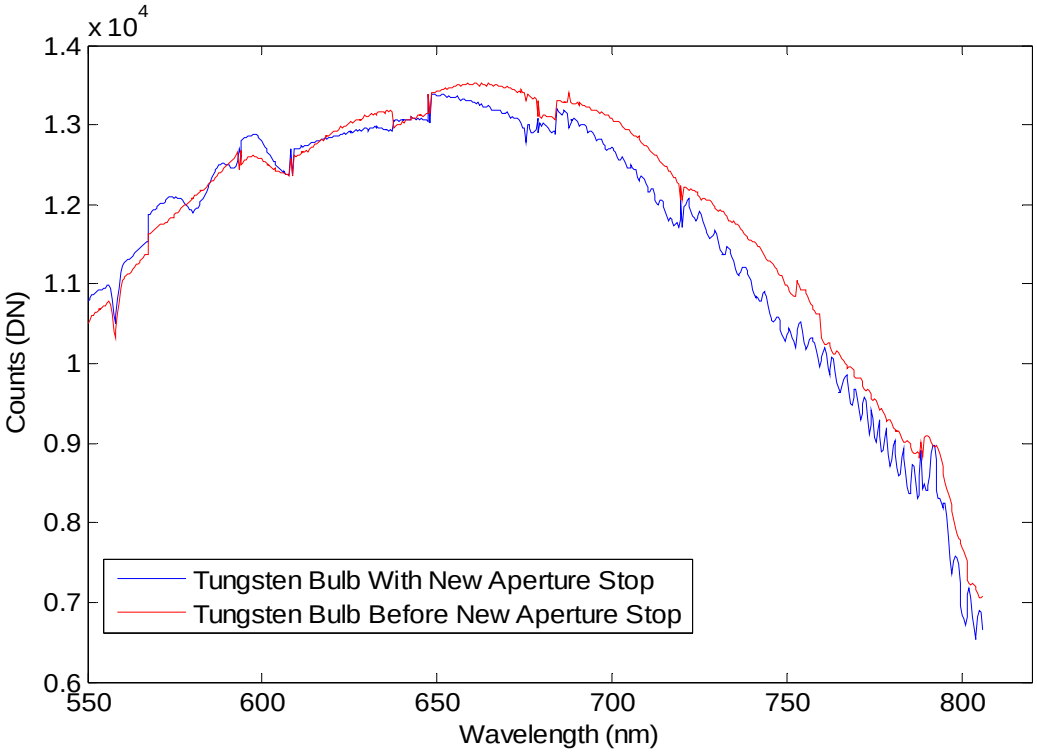

Figure 4.27: Measured Tungsten spectra with and without the new aperture stop in place to display the appearance of the fringing pattern.

As can be seen, this fringing pattern is quite obvious in the blue curve. The question is whether or not this pattern existed previously but is more prevalent now with reduced incoming signal angles (and thus levels) or is the pattern caused by the new aperture stop itself? If a closer look is given to the Tungsten curve in red in Figure 4.27, a very small, but noticeable, wave-like pattern similar to the one in the blue curve is seen. This suggests that this effect existed previously but was not a concern to calibration or operation. The reason for this fringing pattern is not known for sure but is suspected to be an effect of the CCD itself simply called CCD fringing and may have been enhanced by the smaller aperture decreasing the range of angles incident on the CCD. This effect has been documented in *Howell* (2006). Sources like this suggest that it is an effect that can be calibrated but a detailed analysis of this effect is beyond the scope of this project. For more information on the effect of the new aperture stop in regards to fringing, see *Kozun* (2015). The second issue that developed was that the reduced signal levels drastically decreased the signal to noise ratio in the regions that already had a low signal and ratio. Therefore, the produced curves were much noisier and less reliable than they were without the aperture stop at lower wavelengths. Due to these two issues, and the fact that fringing can be ignored for analysis purposes, as it is present in the FM data and is ignored without major negative impact, it was concluded that a reliable relative calibration could not be performed on the new measurements. Therefore, the assumption that the relative calibration should not change was implemented and the calibration from before the aperture stop will be used as the final relative calibration.

4.5.5 Mirror Angle Dependence

The above calibration measurements and results were performed on the system with the mirror at a position of 0°. It is assumed that as the mirror changes angle, the relative intensities of the pixels will not change, but this needs to be verified. To perform this verification, a set of

Tungsten images are acquired at varying mirror angles at a constant exposure time. These images are then averaged into a single spectrum for each mirror angle and are then normalized at the same pixel for all angles. The normalized spectra are then plotted on top of each other as shown in Figure 4.28. This figure again shows only the big slit results which serve as a representation of the middle and small slit results. If the calibration is to be independent of angle, the spectra should be close to identical.

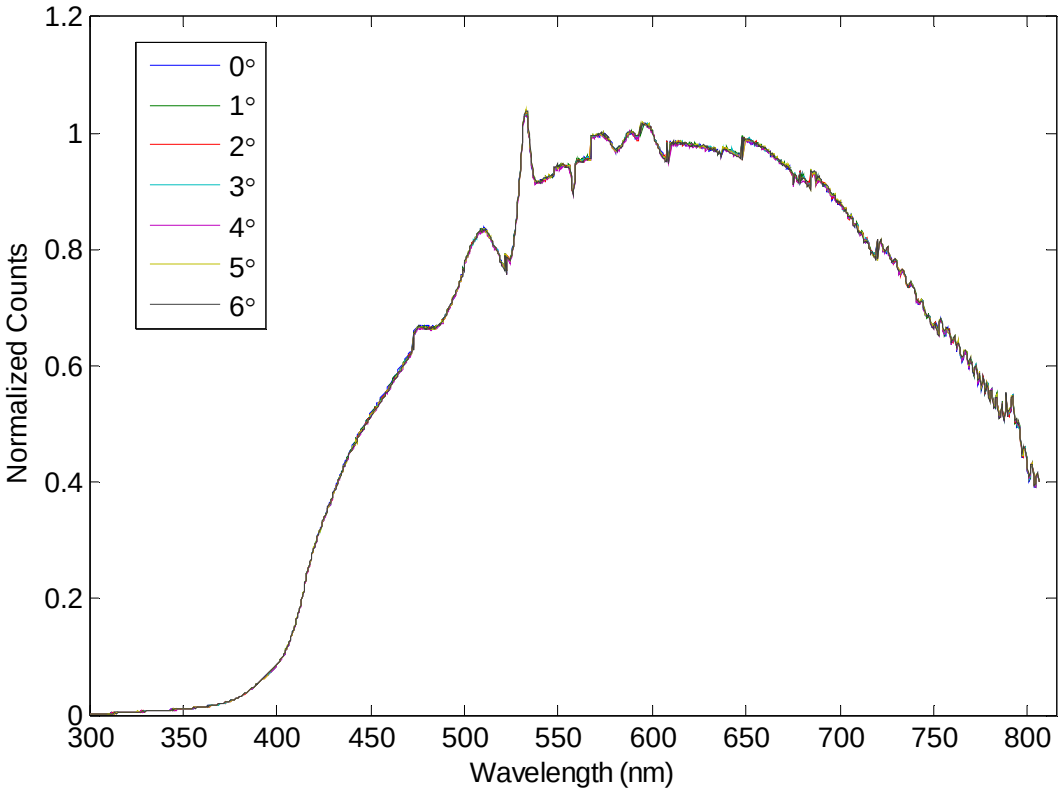

Figure 4.28: Big slit Tungsten spectra at varying mirror angles normalized at 600 nm to show relative intensity independence of mirror angle.

The spectra at different angles do indeed lie on top of each other as expected. This result shows that the relative calibration will be independent of mirror angle which means the results for the 0° calibration can be applied to all images regardless of mirror angle.

4.5.6 Application and Verification of the Relative Calibration

The relative calibration was applied to new measurements and the results were compared to known and expected results in an attempt to verify the accuracy of the result. The curves were applied to a Tungsten image acquired from the calibrated bulb at a different exposure time and different temperature than the calibration measurements were acquired at. A second verification measurement was acquired by performing a ground based sky measurement. This measurement was collected by taking the instrument on to the roof of the Physics building at dawn and imaging the clear sky for several hours. These measurements served as a test run for the system before the balloon flight and also provided measurements that could be calibrated and compared to SASKTRAN simulations to test accuracy of the calibration. The spectrum before and after the calibration is applied to both the Tungsten measurement and the ground based sky measurement are shown in Figure 4.29.

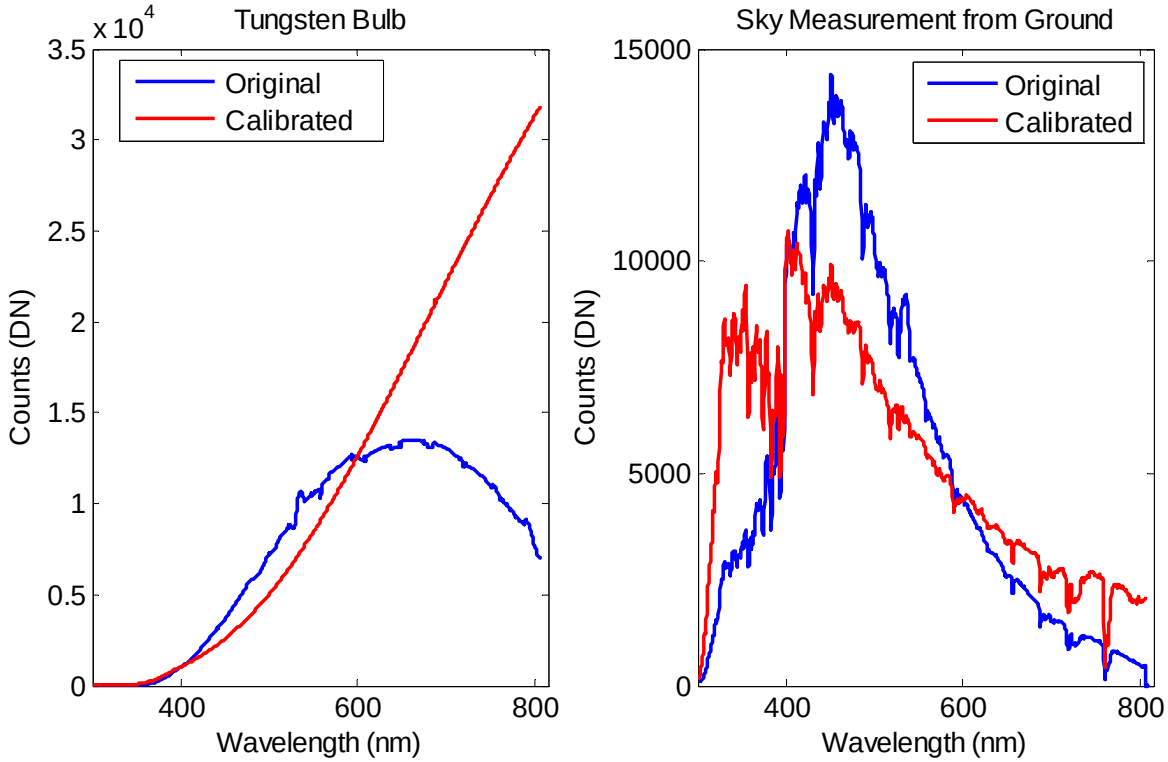

Figure 4.29: A Tungsten spectrum (left) and a ground based sky spectrum (right) before and after the application of the relative calibration.

The plot on the left of Figure 4.29 shows a measurement from the big slit of a Tungsten bulb in blue and the resulting spectrum after the relative calibration is applied in red. Two conclusions can be drawn from this plot. First, the calibrated curve looks to have the proper spectral response that was expected and second, the calibrated curve is smooth and free of averaging features that exist in the measurement which shows how the relative calibration removes these effects. The plot on the right of Figure 4.29 shows a measured and calibrated sky spectrum from the big slit. This calibrated curve can then be normalized and compared to a SASKTRAN simulation spectrum normalized at the same wavelength as shown in Figure 4.30.

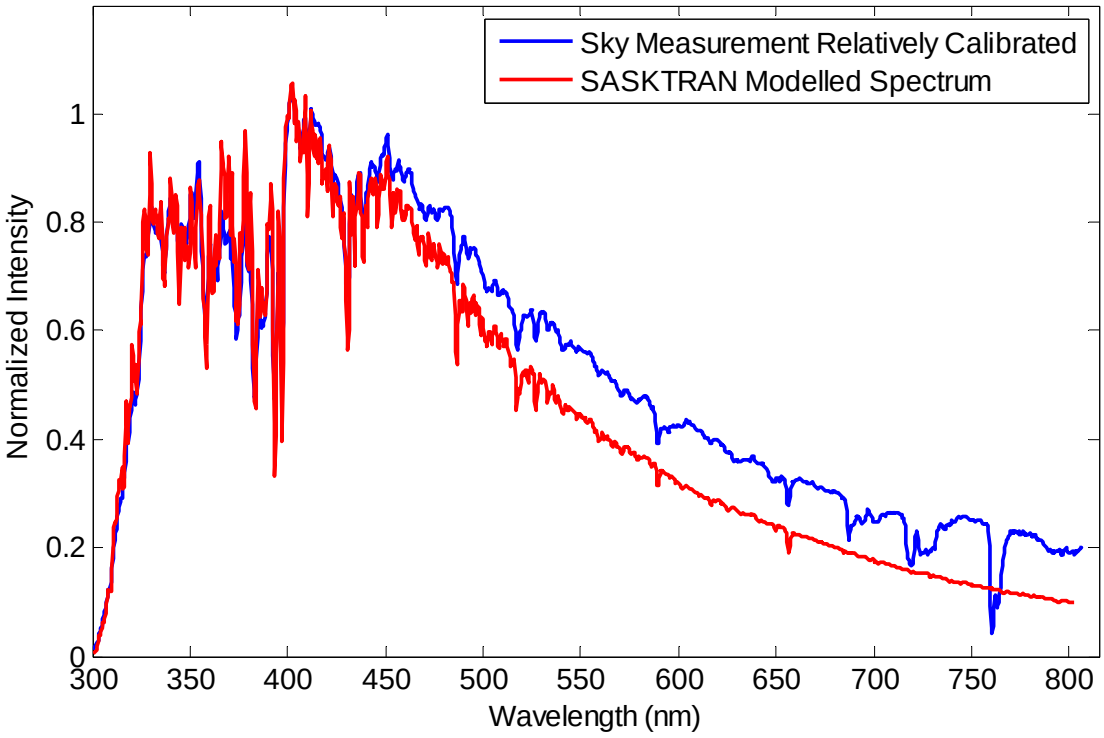

Figure 4.30: Ground based measured sky spectrum that has been relatively calibrated and normalized at 415 nm compared to a SASKTRAN simulation of the measurement also normalized at 415 nm.

The two spectra which are both normalized at 415 nm appear to agree very well below around 450 nm. Above 450 nm, the two start to diverge from each other a bit even though they both

maintain a similar shape. The reason for this may be that the SASKTRAN model used to generate this curve is only an approximation of the sky spectra as the model run did not contain absolute accurate representations of the atmospheric state. This includes parameters like ozone and aerosol concentrations required to perform a highly accurate simulation that were only approximated based on average concentrations. This is most evident in noticing the lack of features, such as the water and molecular oxygen absorption bands, that are present in the measured curve but absent in the simulated curve above 700 nm. The broadband divergence of the spectra is likely due to scattering by tropospheric aerosol not included in the model simulation. However, the general agreement of the two spectra is reasonable and supports the validity of the relative calibration.

4.5.7 Comparison of Calibration to OSIRIS-FM Calibration

With the relative calibration verified, a final comparison and verification was performed by comparing the correction curves to the correction curve used for the OSIRIS-FM. Figure 4.31 shows the three correction curves for the DM and the FM relative curve all normalized at pixel 1353 which corresponds to a different wavelength for all three slits due to the offsets. This figure shows that the relative calibrations agree fairly well at all wavelengths but especially above 400 nm. This result makes sense as it was known that the calibration measurement below 400 nm was not the most reliable due to the low signal levels. Therefore, the calibrations above 400 nm, where there is ample signal, should produce the best results for all curves and in turn should give the best agreement between all curves. This was also a limitation for the FM calibration as a different bulb was used below around 375 nm. Overall, the curves exhibit the same shape including the increase on the edges of the spectral range.

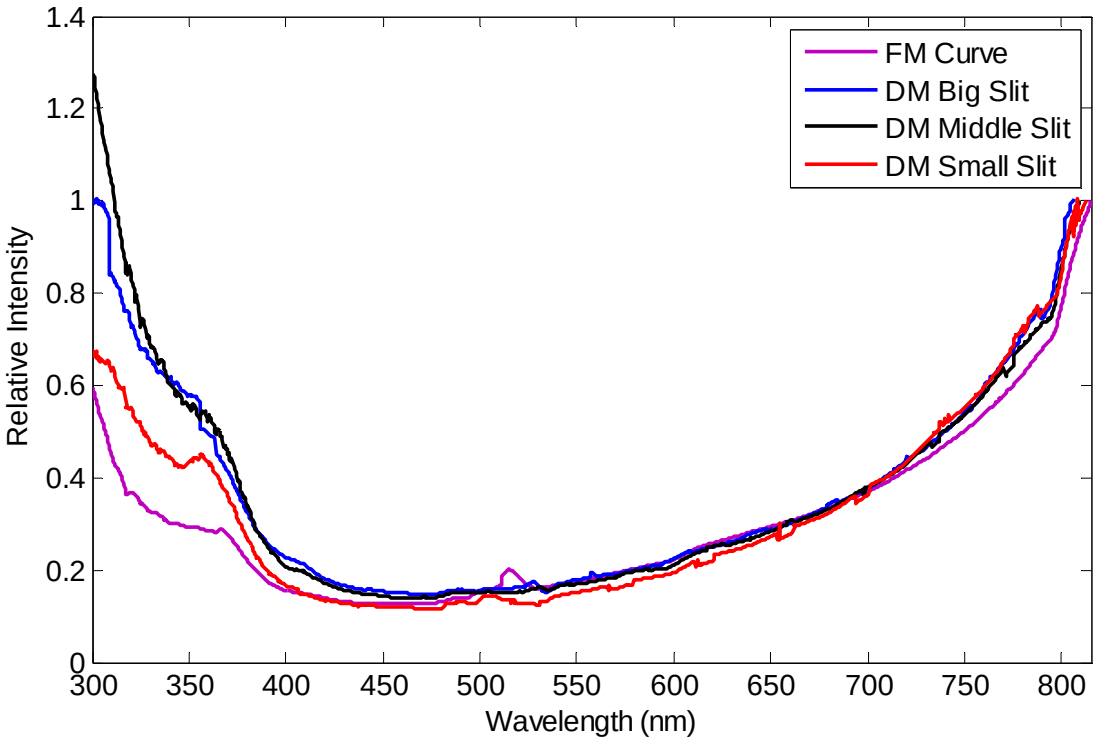

Figure 4.31: Relative correction curves for the OSIRIS-DM and FM normalized at pixel 1353 for each curve which is a different wavelength in each.

4.5.8 Error Analysis

The previous results of the relative calibration in all previous plots have been presented without error bars for clarity of the plots. An error analysis was performed on the final calibration curves and the percent error curves are shown in Figure 4.32. These errors are random errors due to counting error or noise. To calculate the error, the error in the measurements used to develop the calibration was calculated and divided by the total signal at each pixel to retrieve a percent error. The error in the measurement is assumed to be the square root of the counts as the accumulation of counts in a single pixel is assumed to be a Poisson distribution.

$$\delta Relative\ Calibration = \frac{\sqrt{counts}}{counts} \tag{4.23}$$

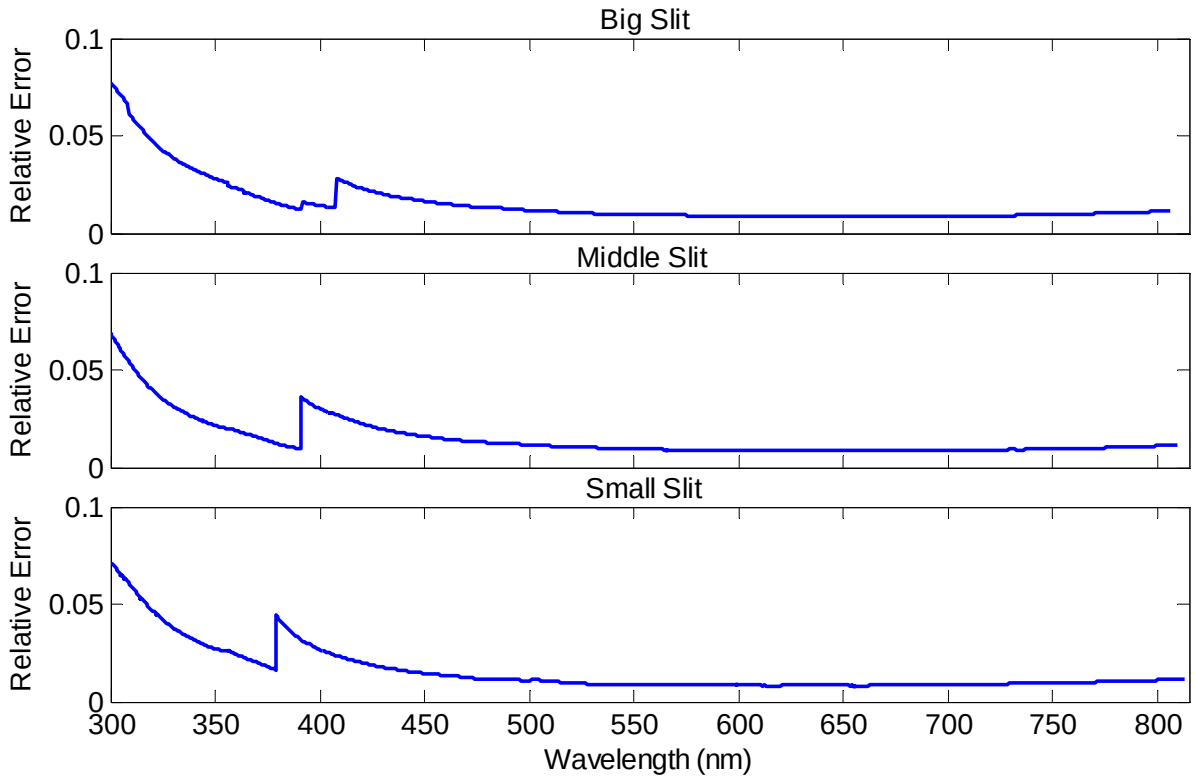

Figure 4.32: Relative calibration relative error curves for all three slits.

These figures illustrate that the relative error of the relative calibration is at worst about 0.08. The second point to notice is that the percent error is less than 0.05 for most of the CCD and grows with decreasing pixel number. This trend is expected as at lower pixel numbers the signal was lower and thus will provide a higher percent error. The last point illustrated by these curves is the sharp change in error curve. This is the point on the CCD where the curves from the two calibration bulbs were normalized and joined together for each slit.

4.6 Absolute Calibration Description

The classic method to perform an absolute brightness calibration is to use a broadband source, such as Tungsten, with a known, calibrated spectrum in absolute radiance units. The source is then used to illuminate the entire entrance aperture at all acceptance angles of the instrument. The measured response is used along with the known bulb brightness to develop the absolute

calibration for all pixels. The main issue with this approach is how to get the light from a Tungsten bulb to fill the entire aperture of the DM with all possible entrance angles. The classic solution to this problem is to use an integrating sphere with an exit aperture larger than the entrance aperture of the instrument being calibrated. The entrance aperture to the DM is 36x36 mm and thus requires quite a large integrating sphere which was not accessible. Therefore, a different method for an absolute calibration needed to be developed.

4.6.1 A New Approach to Absolute Calibration

In 2003, the theory behind a new absolute brightness calibration method using common place optical laboratory equipment was proposed by *Harang, Kosch* (2003). The experimental setup was then described in a second paper by *Kosch et al.* (2003) along with results that support the validity of the method. The following is a summary of the theory and experimental method that they proposed.

The general experimental setup is to illuminate a piece of white card, which serves as a Lambertian surface (S), with a Tungsten bulb placed a distance L away from the card to produce a large and uniform source of light. The light coming off of the card (B_{ph}) is dependent on the albedo of the screen (α). As long as the card is larger than the field of view of the instrument, the Lambertian screen will provide uniform light at all angles to fill the aperture. The theory presents a method that can be used to take any Tungsten bulb and turn it into an equivalent blackbody radiator as was done in Section 4.5.1 for the relative calibration to calculate the irradiance of the bulb. Once the bulb irradiance is known, the radiance of the Lambertian screen can be determined and used to perform an absolute calibration. The bulb that was be used for the DM calibration is the NIST calibrated Tungsten bulb whose irradiance spectrum is already known as it is supplied with the bulb from the manufacturer. Therefore, the portion of calculating the irradiance of a Tungsten bulb can be skipped. The experimental setup is shown in Figure 4.33.

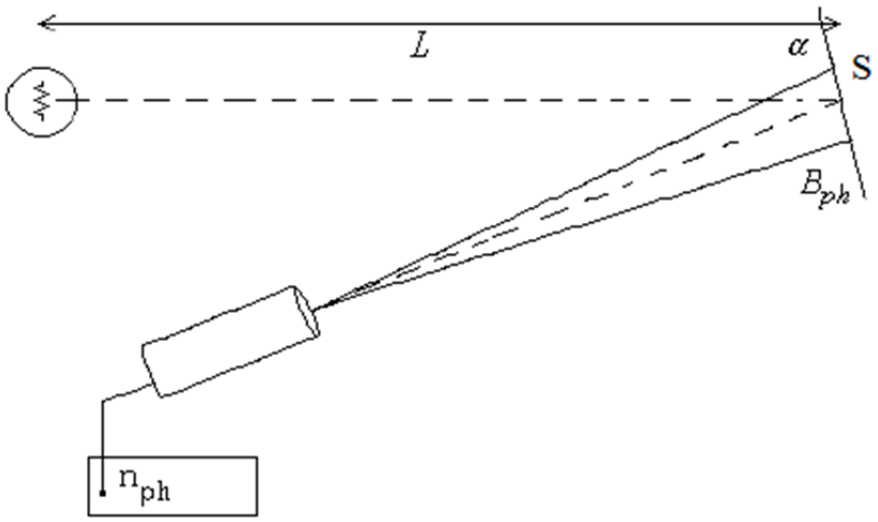

Figure 4.33: Experimental setup for proposed absolute calibration measurement technique. Some labels and dimensions are not used in this implementation as they are only required if the irradiance of the source is unknown. Image adapted from *Kosch et al.* (2003).

With the irradaince (I) of the bulb already known, the radiance (B) of the screen can be determined using Equation 4.24 once the albedo (α) of the screen is determined.

$$B = \frac{I * \alpha}{\pi} \qquad \left[\frac{photons}{s * cm^2 * sr * nm}\right] \tag{4.24}$$

The albedo of the screen can be determined using a new experimental set up which is shown in Figure 4.34.

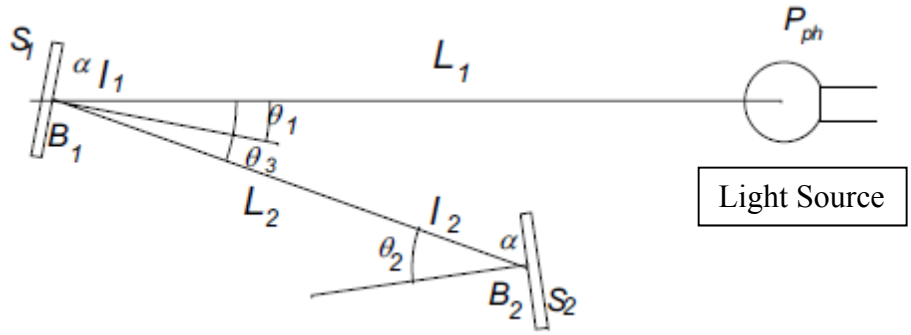

Figure 4.34: Experimental setup for the albedo measurement of the white screen. All labelled parameters need to be known or measured to determine the albedo. Image adapted from *Kosch et al*. (2003).

A second screen of identical material to the first screen is required for this method. The general idea is if the radiance of the first and second screens can be measured then a ratio of the two can be used along with some geometrical factors to find the albedo of the screens. The light source, labelled P_{ph}, illuminates one of the Lambertian screens labelled S_1. Assuming that the photon output rate P_{ph} [photons/s] is constant and omnidirectional, the intensity or irradiance (I_1) is calculated as shown in Equation 4.25.

$$I_1 = \frac{P_{ph}}{4\pi}\cos(\theta_1)\frac{1}{L_1^2}\ \left[\frac{photons}{cm^2 * s}\right]\left(\text{Assuming}\frac{S_1}{L_1^2} \ll 1\right) \tag{4.25}$$

S_1 is the area of screen 1, L_1 is the distance between the light source and the first screen, and θ_1 is the angle between the direct line from the source to S_1 and the normal of S_1. The radiance observed from screen 1 (B_1) is found by integrating over all solid angles. The result is 4.26.

$$B_1 = \frac{I_1 * \alpha}{\pi}\ \left[\frac{photons}{s * cm^2 * sr * nm}\right] \tag{4.26}$$

Next, at a distance of L_2 away from S_1 a second screen of area S_2 is illuminated by the light coming off of S_1 which has an irradiance of:

$$I_2 = \cos(\theta_2)\cos(\theta_3)\,B_1\frac{S_1}{L_2^2}\left[\frac{photons}{cm^2 * s}\right] \tag{4.27}$$

where θ_2 is the angle between the direct line from the center of S_1 to the center of S_2 and the normal of S_2, and θ_3 is the angle between the direct line from the center of S_1 to the center of S_2 and the normal of S_1. Finally, the radiance observed from S_2 can be calculated.

$$B_2 = \frac{I_2 * \alpha}{\pi} = \frac{\alpha}{\pi}\cos(\theta_2)\cos(\theta_3)\,B_1\frac{S_1}{L_2^2}\ \left[\frac{photons}{s * cm^2 * sr * nm}\right] \tag{4.28}$$

The last step is to take this equation and solve for the albedo term which produces a method to calculate the albedo based on radiance measurements that can be made with the DM.

$$\alpha = \frac{B_2}{B_1}\frac{\pi L_2^2}{S_1}\frac{1}{\cos(\theta_2)\cos(\theta_3)} \tag{4.29}$$

With the albedo term calculated, everything is known to be used with Equation 4.26 to calculate the reference spectrum for the absolute calibration.

4.6.2 Implementation of Albedo Measurement Experimental Setup

The two Lambertian screens are constructed out of 2 layers of plain white paper on top of a piece of cardboard to provide stability to the screen and to help make it opaque. The specific size of screen 1 is arbitrarily selected but the general idea is to have it be as large as possible to collect lots of light while allowing L_1 to be around 1 m and still satisfy the $S_1/L_1^2 << 1$ condition. The size of screen 2 is chosen to be small so that L_2 could also be small and still satisfy the $S_2/L_2^2 << 1$ condition but be large enough to fill the field of view of the DM. The final choice for the size of screen 2 is to be twice the size of the field of view of the DM at 50 cm away from the entrance aperture to make positioning adjustments easier. With the screen this size, it ensures that the field of view will be filled even if alignment is not 100% precise; it leaves ample room for error without effecting results. The last setup design choice made is to make the screens be parallel to each other so that angles θ_2 and θ_3 are 0. This eliminates having to carry through two of the angle dependencies as the cosine of these angles will be 1 or close enough to 1 that they can be considered 1 without introducing significant errors to the results.

The final screen sizes used were 15.8 cm x 23.5 cm +/- 0.1 cm for S_1 and 9.1 cm x 8.2 cm +/- 0.1 cm for S_2. The Tungsten bulb was at a distance, L_1, of 93.2 cm +/- 0.3 cm from S_1, the screens were a distance, L_2, of 38.3 cm +/- 0.3 cm apart and the screens were parallel to each other. These sizes ensure that the required ratios mentioned are below 0.05 which is considered to be adequate for the much less than one constraint. Angle θ_1 was 21° +/- 2° and because the screens are parallel, angles θ_2 and θ_3 are 0° +/- 2°.

4.6.3 Albedo Measurements and Calculated Results

The above described setup was implemented and images of the two screens were acquired. As with the relative calibration, this calibration was not performed on the single slit system or the multi-slit system without the front end system attached. As always, 10 images are acquired to be averaged together with a dark image collected after each of the illuminated images to correct for dark current, DC offset, and background noise. The next step is to measure the radiance of just the first screen without changing any of the angles. This is achieved by moving the DM to the location and orientation of screen two and acquiring an image set in this configuration. With the radiance measurement for each screen obtained, a calculation of the albedo was performed and the results for each pixel along with a fitted curve are shown in Figure 4.35.

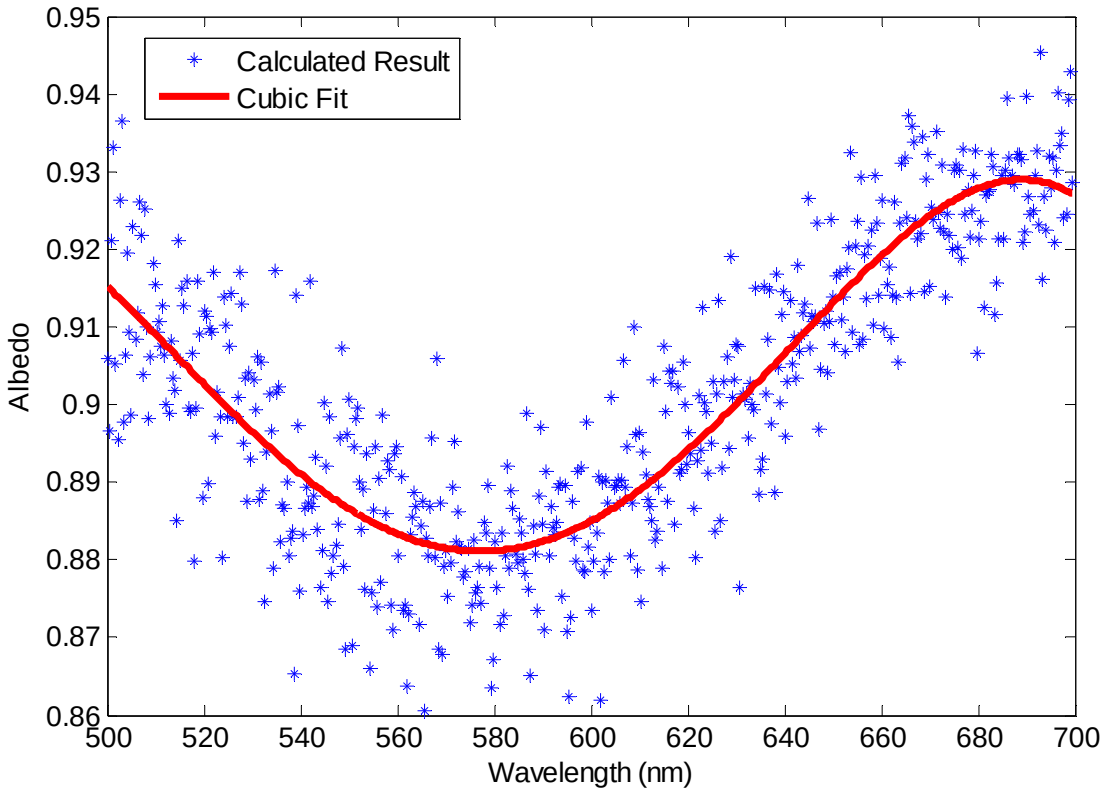

Figure 4.35: Calculated albedo measurement results with a cubic fitted function.

The albedo results are calculated from a pixel by pixel calculation and then the results are averaged into a single 'spectrum' of results using the usable pixels. These results are then fitted to the cubic function shown to serve as the final albedo result. The results are only shown from 500 nm to700 nm because the signal measured in the two screen method was too low outside of these wavelengths to yield reliable results. Therefore, an absolute calibration will be performed on these wavelengths and the rest of the CCD will be absolutely calibrated by applying the relative calibration with respect to these known wavelengths.

4.6.4 Required Calibration Measurements and Setup

With everything available to determine the brightness of the reference spectrum, the next step is to determine the measurements required to perform the calibration and the experimental setup required to obtain these measurements. The goal of the absolute calibration is to be able to take a measurement in DN from the CCD in a known amount of time and determine the radiance of the source. In order to achieve this, the charge generation as a function of exposure time for each pixel being absolutely calibrated needs to be determined when imaging the calibrated source. The charge generation should be a linear function with a y-intercept of zero. Therefore the slope of this line can be determined and used to generate a proportionality constant (k). The slope is then divided by the known radiance for that pixel to produce the proportionality constant.

$$k = \frac{slope}{Known\ Radiance} \tag{4.30}$$

The slope of the line will give units of DN/s. Therefore, when the calibration is applied, it will need to be multiplied by the exposure time (t) of the measurement. In the end the absolute calibration is of the following form.

$$Radiance = \frac{Measured\ DN}{kt} \tag{4.31}$$

The required measurements to produce to the final calibration are images of the calibrated bulb illuminating the single screen as shown previously in Figure 4.33 at varying exposure times. The chosen exposure time range is 100 ms to 2000 ms in 50 ms steps. The setup parameters include the bulb placement at 50 cm +/- 0.3 cm away from the screen with the screen being perpendicular to the line of sight of the DM. The angles are arbitrary as the screen is a Lambertian surface. The same imaging technique of ten images with corrective dark images taken to be averaged into a single image is employed.

This method produces a range of pixels (or wavelengths) that can have the absolute calibration applied to them and then the rest of the pixels can be absolutely calibrated relative to the one by implementing and scaling the relative calibration. Therefore, a choice of which pixel to use as the calibrated pixel has to be made. The choice for this calibration was to use all of the pixels individually and develop a set of absolutely calibrated curves. Then, this set is averaged together to produce the final result.

4.6.5 Mirror Position Correction Factor

The previous results and measurements for the absolute calibration were done with the scanning mirror being at a position of 0°. Unlike the previous calibrations where the mirror position had no effect on the application of the calibrations, the mirror position changes the absolute calibration. This is because at different mirror positions, the amount of light that enters the system in a given exposure time changes and thus changes the DN. This effect is caused by some form of angular dependence of the scan mirror and baffle system. This may be an angular dependence in the reflectance of the mirror or an angular dependence of the baffle system. The evidence of this effect is shown in Figure 4.36 where multiple Tungsten images at varying mirror angles are plotted together. These spectra were obtained by imaging a white Lambertian screen illuminated by a Tungsten bulb at a constant exposure time and varying mirror angle.

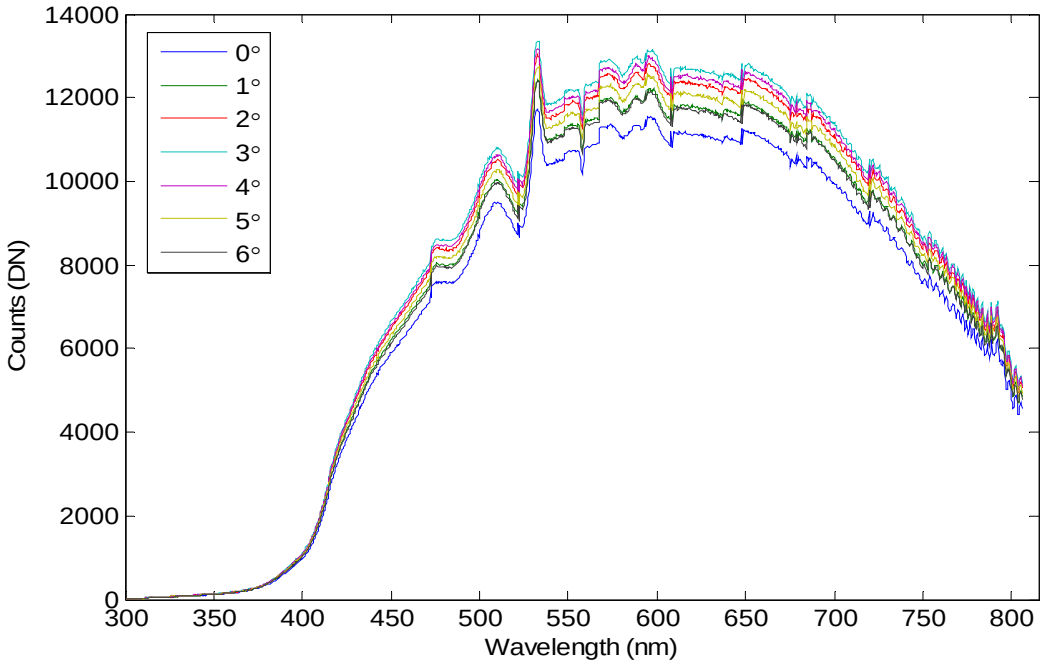

Figure 4.36: Tungsten spectra at a constant exposure time and varying mirror angle to show intensity change with changing angle in the big slit.

Rather than perform an entirely new calibration for each mirror position, a correction factor can be determined for each pixel based on the data set shown in Figure 4.36. To develop this correction factor, a function of DN versus mirror position was determined for each discrete wavelength and is normalized to 1 at a mirror position of 0°. A representative resulting curve for one wavelength is shown in Figure 4.37. The application process of this correction factor is to first perform the absolute calibration as previously described and in the end divide by the correction factor for the corresponding mirror position and wavelength. This will correct for the extra amount of light coming into the system and reference it to the calibrated amount at 0°.

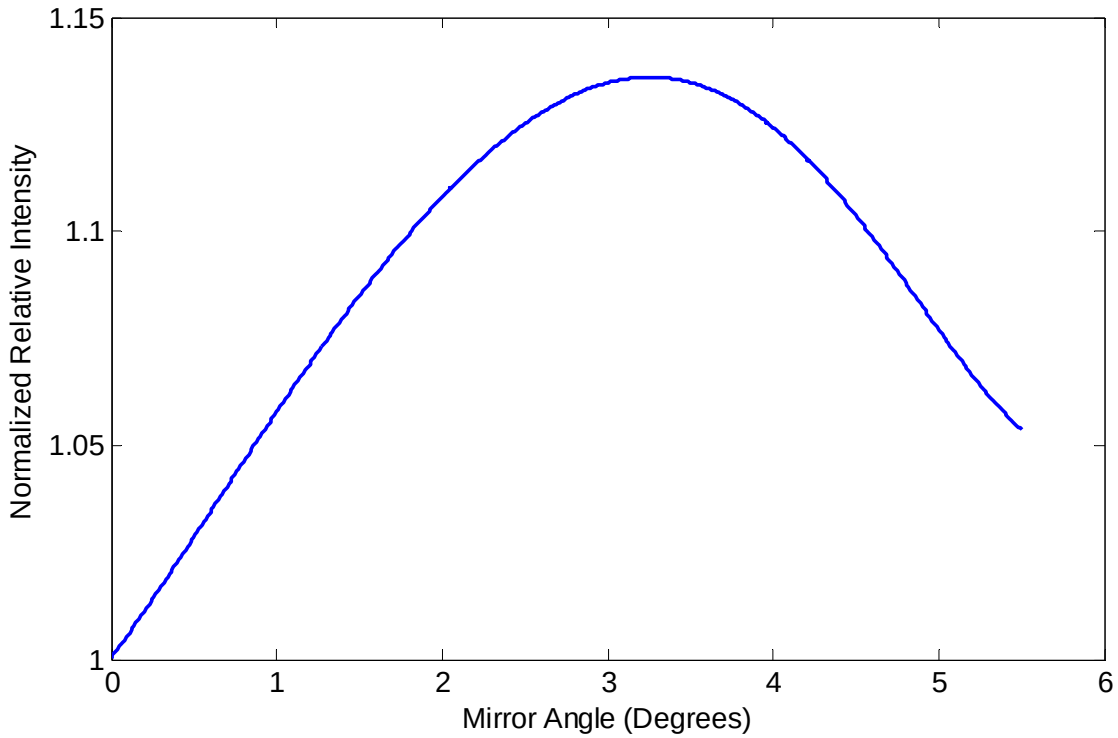

Figure 4.37: Representative relative correction curve for mirror angle dependence for 577.3 nm.

4.6.6 Aperture Stop Correction Factor

With the installation of the new aperture stop decreasing the amount of signal that enters the DM in a given exposure time, the absolute calibration obviously changes. Rather than redo the entire calibration with measurements from the new system, a correction factor for the new system will be determined. Similar to the correction for the mirror angle dependence, a ratio for the amount of light that enters the system with the new aperture stop to the amount of light that entered previously can be determined and used as a correction factor. These measurements are acquired by imaging a white screen illuminated by a Tungsten bulb with and without the new aperture stop installed in identical configurations for a variety of exposure times. The ratio for each slit was found to be constant in exposure time as was expected. To retrieve a final correction factor for each pixel, the correction factors for all exposure times used were averaged together. The

results for all three slits were fairly constant across the spectrum until below 400 nm due to low signal levels. Because the rest of the spectrum was essentially a constant value, the ratio between 300 and 400 nm was extrapolated to be the average of the correction ratio above 400 nm. This resulted in an average correction ratio of 0.24, 0.26, and 0.22 for the big, middle and small slit respectively. Due to the fact that the new aperture stop should reduce the amount of light that enters each slit in the same ratio, these three ratios were averaged together to produce one final ratio for the CCD as a whole. This final ratio is 0.24 +/- 0.02. The application of this correction factor is to perform the entire absolute calibration as described and in the end, divide by this factor to produce the final product. Results of the absolute calibration applied to measurements and evaluation of its performance is shown in Chapter Five when the calibrations are applied to flight measurements.

4.6.7 Calibration of the Middle and Small Slits

Due to the low signal levels in the middle and small slits, a reliable absolute calibration could not be performed using the above method. Instead, the big slit calibration was scaled and applied to these slits. The amount of light that enters any slit is directly proportional to the slit width. Since the slit widths are constants, a ratio of the big slit to the middle and small slit can be determined and will also be constant. Therefore, the absolute calibration for the big slit can be multiplied by this ratio and used as an absolute calibration for the other slits. This results in an absolute calibration equation of the following form.

$$Radiance = \frac{Measured\ DN}{kt} * ratio \tag{4.32}$$

The ratio for the middle and small slits to the big slit was determined by taking measurements of a white screen illuminated by a Tungsten bulb at varying exposure times. The ratio was calculated for each slit and each wavelength and the final ratio was an average of all the ratios

over all exposure times measured. A similar issue as with the correction factor for the new aperture was observed below 450 nm in that the signal was too low to provide a reliable ratio. The same solution was implemented in that the extrapolated ratio below 450 nm is an average of the ratios above 450 nm as this ratio should be constant over all wavelengths. The average ratio for the middle slit is 0.25 and the small slit is 0.06. With these ratios, the absolute calibration as presented can be applied to the middle and small slit measurements and then be multiplied by this ratio as shown in Equation 4.32.

4.7 Thermal Testing

The last issue to investigate before the balloon flight is to test how the system performs in different thermal environments, specifically colder temperatures. The theory is that colder temperatures may cause the optics to shift to new alignments that would alter the wavelength registration and PSF. To view the effects of lowering temperature, the system was taken into a cooler with an ambient temperature of 8 °C. The instrument was set up to continually collect measurements of a Neon spectral bulb as it cooled. It was desired to have a more drastic temperature change to test this issue but there were no options for colder temperatures in the time frame at hand. In order to check for changes in the above mentioned calibrations, a measurement acquired at about room temperature (23 °C) is compared to a measurement taken at the coldest temperature reached by the CCD (8 °C) with the same exposure time. Figure 4.38 shows a sample wavelength range of Neon from the big slit at these temperatures.

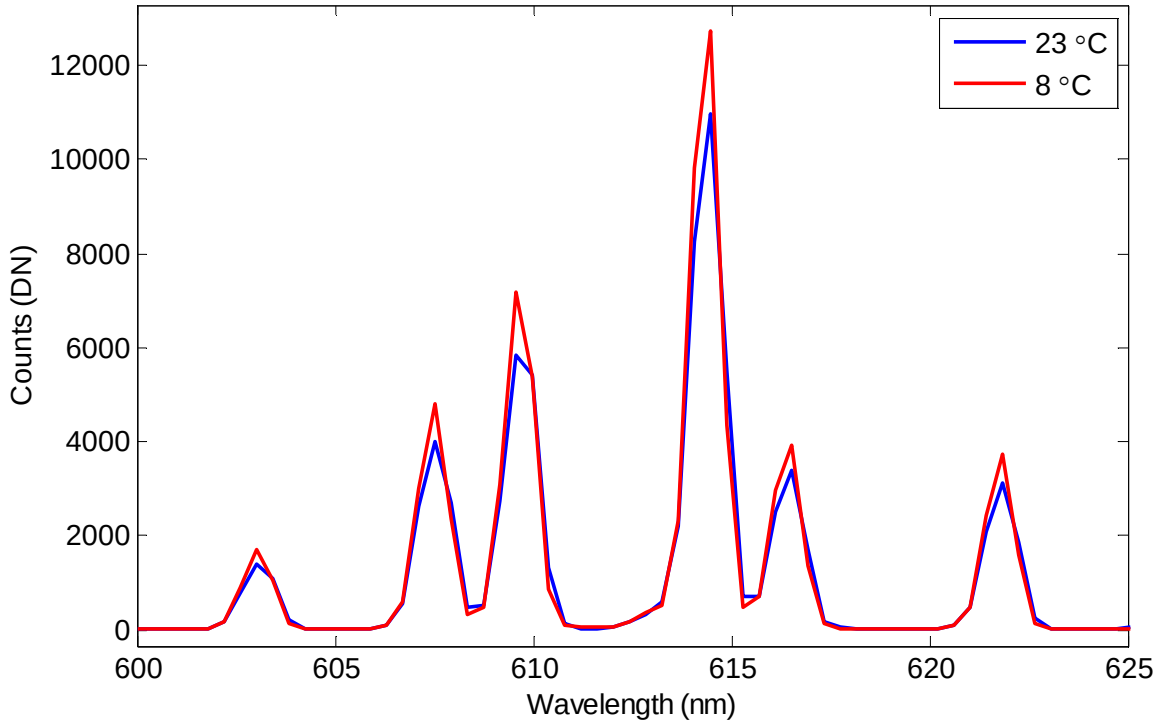

Figure 4.38: Comparison of Neon spectra measurements in the big slit at temperatures of 23 °C (blue) and 8 °C (red).

There is no evidence to suggest that the peak location or width of the peaks has changed by the changing temperature. The only difference is the small change in peak height which is insignificant for the purpose of this test. This is because the height difference is most likely do to experimental setup errors as the setup had to be moved and replicated in two different areas. Therefore it is concluded that over this temperature range, the wavelength and PSF are independent of temperature. These calibrations will be applied to the flight measurements and have their performance evaluated with comparisons to the solar spectrum and SASKTRAN simulations.

CHAPTER 5
POST FLIGHT ANALYSIS

The OSIRIS-DM instrument and support team arrived in Timmins, Ontario on August 24, 2014 for the start of the balloon campaign. Upon arrival, the instrument was set up on a bench in the integration hall at the balloon base. Here, the instrument underwent verification tests to ensure proper functionality and that no damage occurred to the instrument during transport. These verification tests involved imaging a Neon emission bulb and a Tungsten bulb through the same diffusing plate used to collect calibration measurements. The Neon measurements were used to verify the wavelength registration and PSF while the Tungsten measurements were used to verify the illumination of all three slits as well as the relative calibration. All verification tests yielded positive results and proper functionality of the DM was confirmed.

After the verification tests were completed, the instrument was set up in its flight configuration and was integrated onto the gondola. The balloon launch came in the morning of September 19, 2014 at 5:36 UTC (1:36 a.m. local time). The ascent of the gondola took just over 2.5 hours to reach a stable float altitude around 36.5 km and first light was not confirmed with the DM until almost 4 hours after launch at 9:33 UTC. During the ascent and float time in darkness, the DM collected dark images at varying exposure times over the temperature range experienced by the gondola and CCD as planned. The temperature profile of the CCD during flight is shown along with corresponding labels of major events during flight in Figure 5.1.

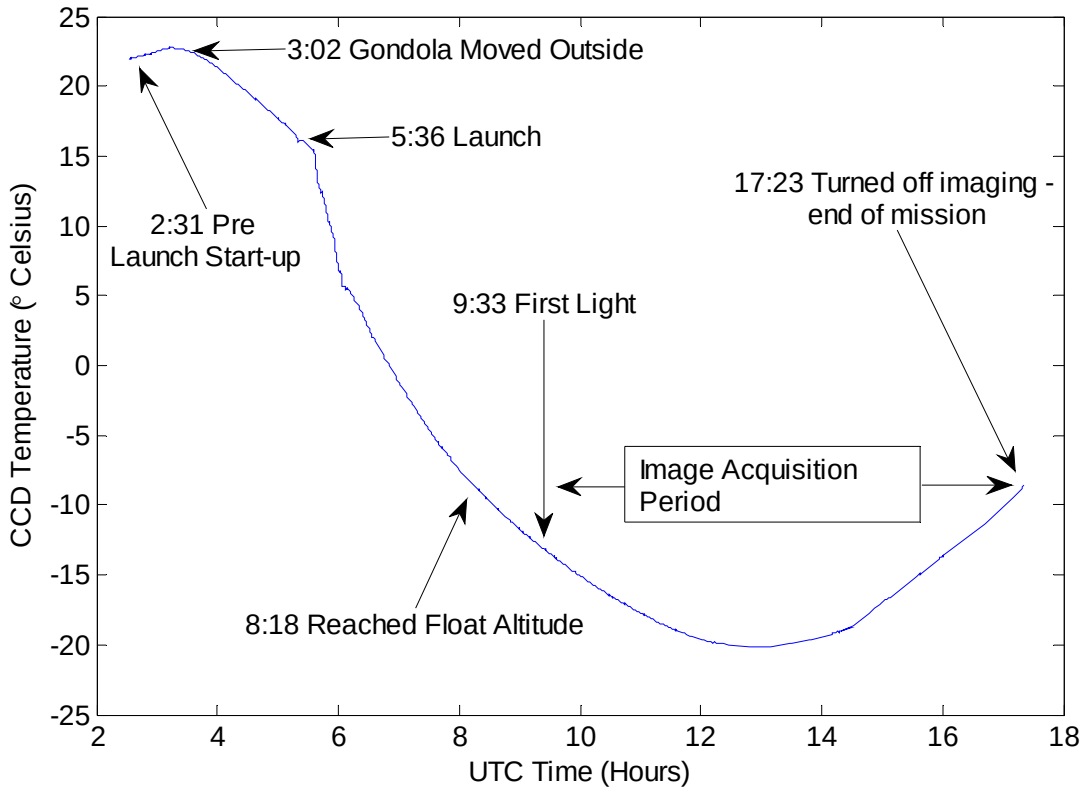

Figure 5.1: Temperature profile of CCD in Celsius of the balloon flight versus UTC time in hours. The labels show the times of major events in the flight.

During the image acquisition period between 9:33 and 17:23 UTC the DM acquired a variety of images over a range of altitudes, positions, and look directions. The altitude of the balloon during the flight is shown in Figure 5.2. As can be seen, once the balloon reached float altitude, it stayed essentially constant for the entire image acquisition period. Therefore the altitude variation between images is minimal. The measurements acquired during this period will be used to analyze and evaluate the performance of the instrument with respect to the laboratory calibrations and comparison to SASKTRAN simulations.

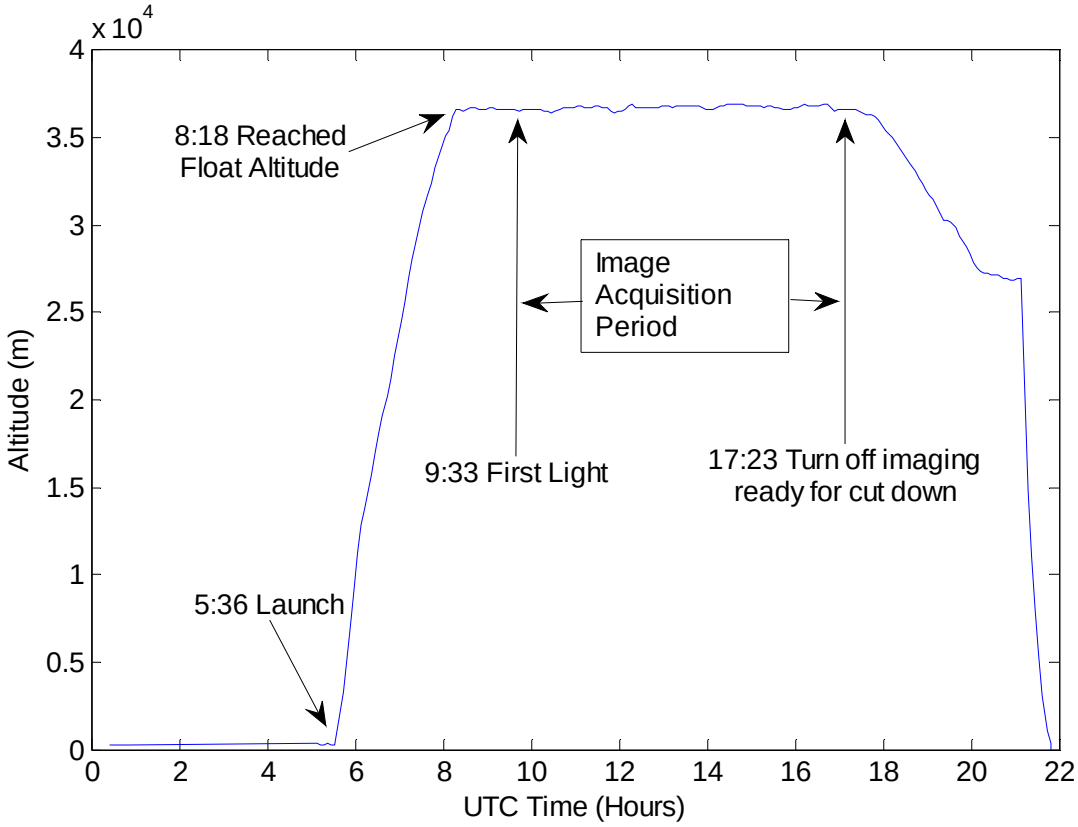

Figure 5.2: Altitude in meters of the balloon during flight versus UTC time in hours. The labels show times of major events during the flight.

5.1 Dark Current Calibration Results and Performance

5.1.1 Dark Current Measurement Collection

During the balloon flight, the ascent of the balloon was used for collecting dark current measurements. The measured temperature change during this time on the CCD was +23 °C to -15 °C, as shown in Figure 5.1, which is large enough to produce a robust temperature dependence of the dark current. Also, because of the slow ascent, the temperatures were relatively stable for each image set acquisition.

5.1.2 DC Offset Removal Results

The DC offset removal method of averaging the first and last eight DC offset pixels described in Section 4.1.4 was first applied to a measurement acquired at 22 °C just before launch during the

preflight window prior to leaving the integration hall. In order to verify the technique, the method was applied to a set of dark current images acquired over a range of exposure times at a constant temperature. If the method works, the resulting plot of DN due to dark current versus exposure time should be linear with a y-intercept of 0. The resulting plot for one pixel (92,800) is shown in Figure 5.3.

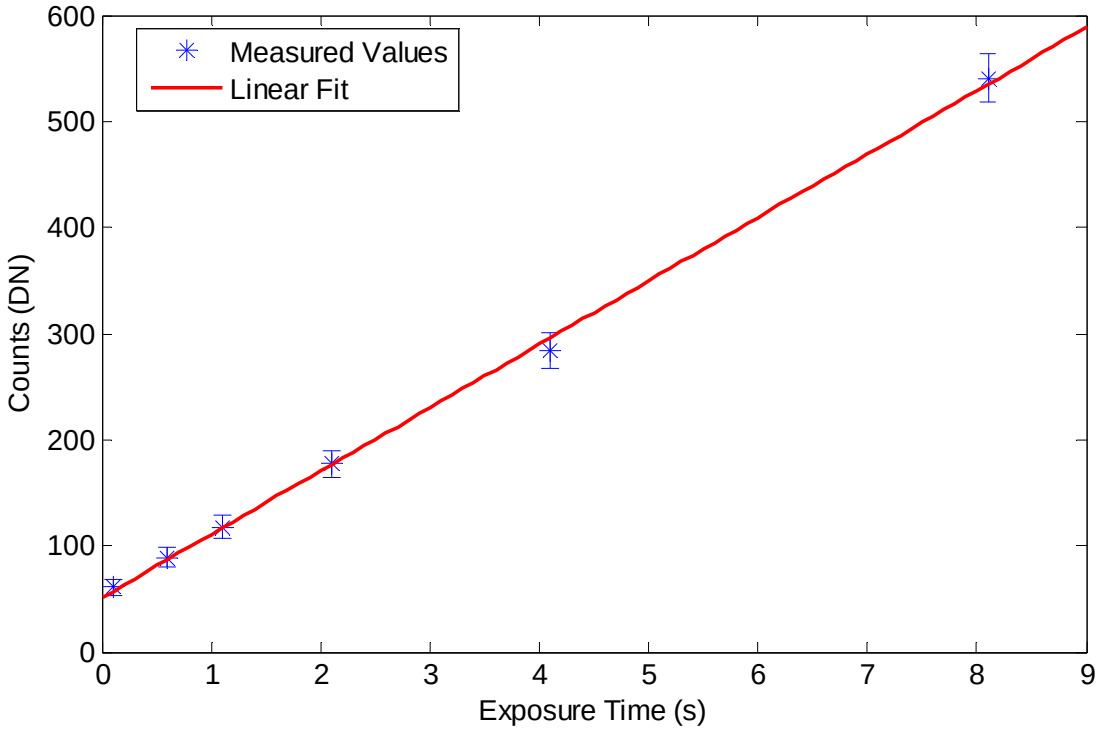

Figure 5.3: Representative plot of dark current signal with DC offset removed using averaging method on a pixel (92, 800) obtained at 22 °C.

The measured values with the DC offset removed are linear within counting error as expected but the y-intercept is definitely not 0 which shows an error in the DC offset removal method. Therefore, a second removal method was required to accurately remove the DC offset. The second method is to use the linearity of the dark current versus exposure time and the fact that the y-intercept of this linear function should be 0 if not for the DC offset to determine the value of the DC offset to be removed for a given temperature and pixel. A sample plot of this method

is shown in Figure 5.4 for one pixel (92,800) from an image acquired at 22 ° C just before launch in the preflight window prior to leaving the integration hall.

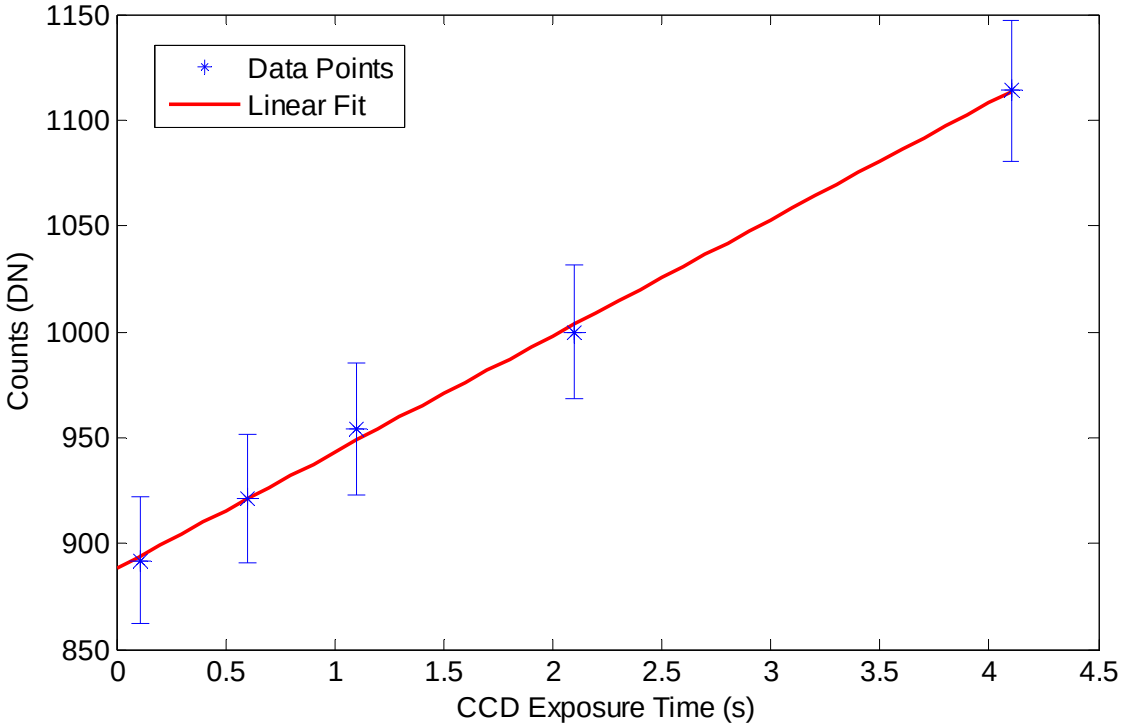

Figure 5.4: Representative plot of dark image signal versus exposure time at 22 °C for pixel 92, 800. This trend holds true for all pixels at any temperature.

This plot shows that the dark current signal does increase linearly with time within counting error as was expected. The figure also shows an extrapolation of the linear fit down to a 0 second exposure time where the y-intercept is not 0, but instead represents the DC offset. This removal method will obviously produce plots like Figure 5.3 but with a y-intercept of 0. The difference between these two methods is shown in Figure 5.5 where histograms of the resulting DC offset value for all pixels are plotted. The linear fit method (left histogram) requires five images to calculate one DC offset for each pixel whereas the averaging method (right histogram) calculates the DC offset on an image by image basis. The histograms show the results for all pixels in each method and thus the averaging histogram has more occurrences due to more calculated DC

offsets for the same set of five images. As can be seen, the two mean values do not agree at this temperature. It is also noticeable that the histogram displaying the results of the linear fit method does not exhibit an obvious Gaussian shape like the other histogram. The reason for this is not known, but the important fact is that the mean of this histogram is different than the mean of the averaging method histogram.

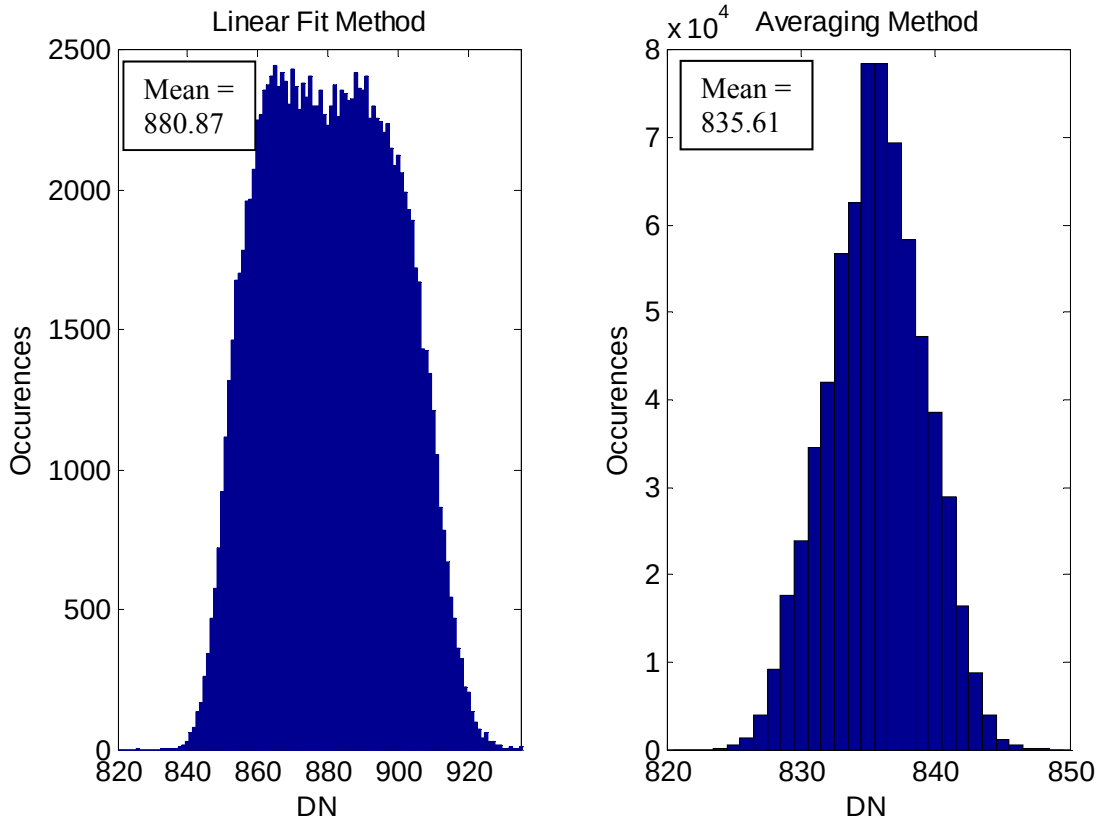

Figure 5.5: Histograms of resultant DC offset values for all pixels as determined by the two different removal methods at 22 °C. All bin sizes are 1 DN.

Apart from the issue of the slightly unexpected shape produced by the linear fit method, the main issue with this removal method is that it requires a dark image set at a constant temperature over a large range of temperatures to develop a temperature dependent method. Due to issues with the dark image set acquisitions during ascent, measurements below -6 °C were not

able to be used to generate a DC offset value using the second method. This means that this method cannot be accurately applied to flight measurements as all illuminated measurements are below -6 °C. However, it can be used as a comparison method to investigate the issues with the averaging of the DC offset pixels method. To investigate, both methods were first applied to an image at a different temperature, -6 °C. The two methods are compared by comparing histograms of the resulting DC offset values for all pixels. The resulting histograms of each method are shown in Figure 5.6. Again, the histograms have data sorted into 1 DN wide bins and the difference in occurrences is due to the difference in the methods as previously described.

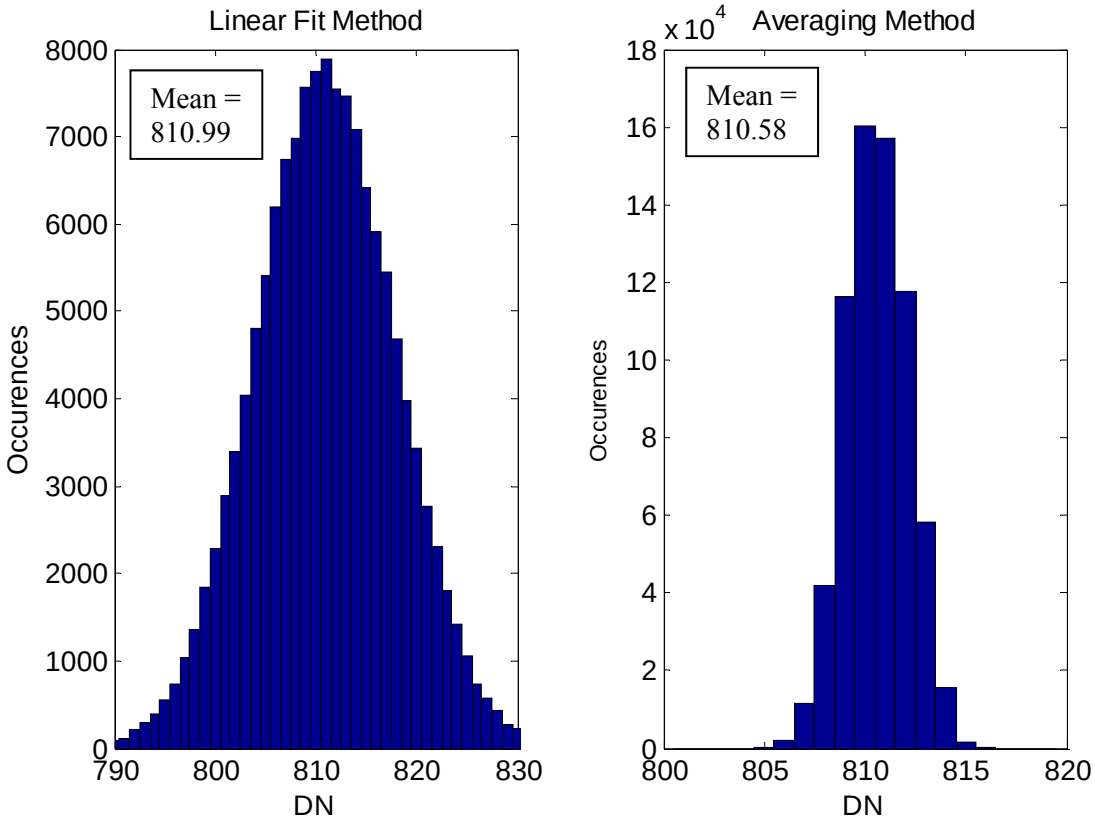

Figure 5.6: Histograms of resultant DC offset values for all pixels as determined by the two different removal methods at -6 °C. All bin sizes are 1 DN.

Comparison of these two histograms shows that the DC offset value determined by each method agrees with one another which suggests that both methods work equally well for this

temperature. This suggests that there may be a temperature dependence on the averaging method and that the accuracy of this method increases with decreasing temperature. Therefore, a temperature range may exist where the method is valid and thus can be implemented. To investigate this, a further comparison of the two methods was conducted at different temperatures and a plot of each method's mean DC offset value is shown in Figure 5.7.

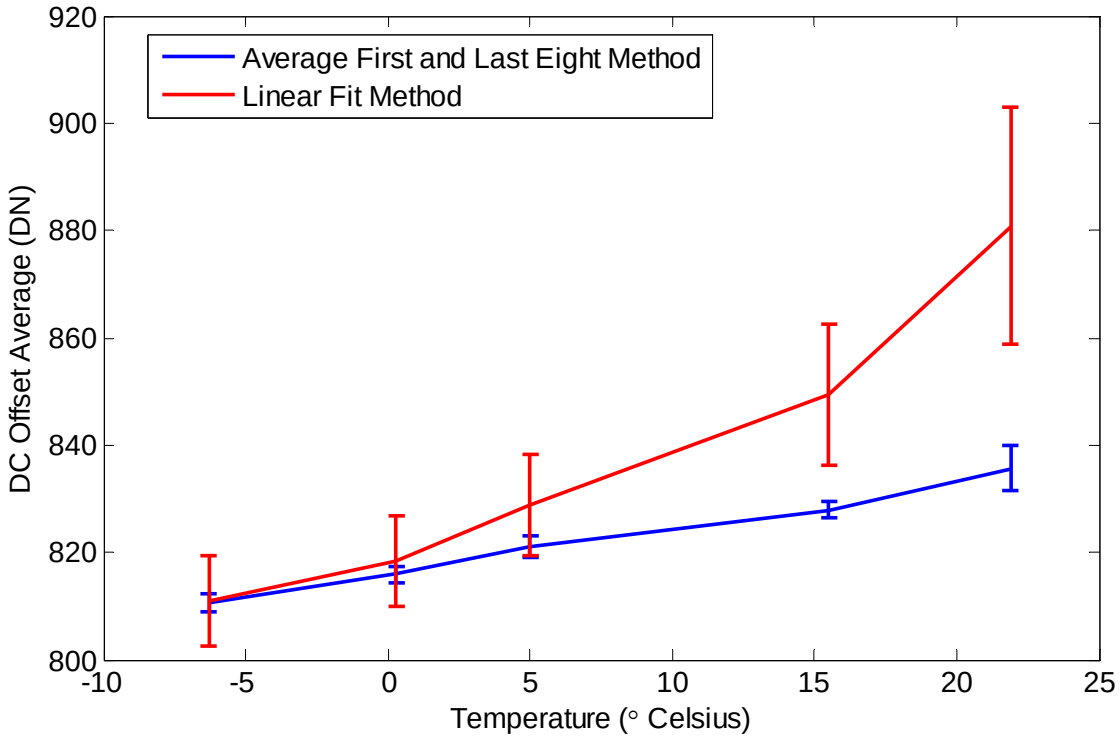

Figure 5.7: Average DC offset values as calculated by the two different DC offset determination methods versus temeprature.

The error bars in Figure 5.7 are the HWHM values calculated from the standard deviation of the histograms of the two removal methods. Based on these results, it appears that for temperatures above 5 °C, the methods do not agree within error. This suggests that the desired averaging method can be applied to measurements taken below 5 °C. It is assumed that below -6 °C, the two methods continue to converge. This could not be confirmed due to limitations in the measurement set. This constraint works well with the balloon flight measurements, as all spectra

were acquired below -5 °C and therefore this method will be used to remove the DC offset from all balloon measurements.

5.1.3 Dark Current Characterization and Removal Results

With the DC offset removal confirmed for flight measurements, dark images can be corrected to produce images with signal only due to dark current generation. The next step is to verify the behaviour predicted by Equation 4.2 i.e. is $\log(DN/s)$ vs 1/T is indeed linear for dark current as was predicted in Section 4.1.5. A sample plot of this relationship is shown in Figure 5.8.

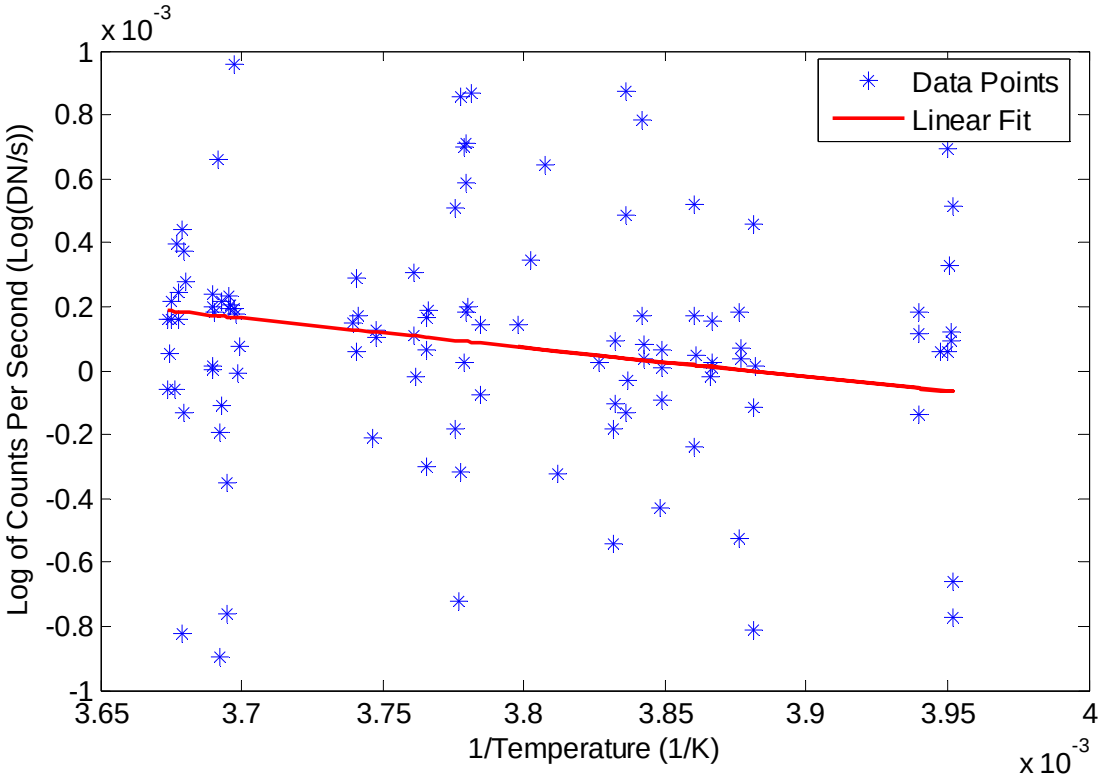

Figure 5.8: Plot of log(DN/s) vs 1/T for a set of dark current images to illustrate the linear relationship between these quantities. T = 0 °C to -20 °C. Outliers outside of the displayed region are omitted to illustrate linear fit properly.

From this plot, it is apparent that the measurements do not exhibit an obvious linear relationship as was predicted. This is due to the small temperature range of the measurements (0 °C to -20 °C) and that the dark current accumulated in this range is very close to 0. Therefore, any

noise in the system will be significant in comparison to the dark current measurement. The only conclusion of this figure is that the dark current exhibits the overall trend expected when a linear line is fit to the measurements. The slope of this line is determined from the linear fit and used along with Equation 4.3 to produce a dark current prediction equation for each pixel. This removal will be a small amount for the flight measurements as they are all acquired at low temperatures.

To verify the removal process, the removal technique is applied to a dark image from flight acquired at -10 °C that was not used to generate the calibration. A histogram of the resulting pixel values is shown in Figure 5.9. The results have been normalized with exposure time and sorted into 1 DN/s wide bins to match the removal method presented for the laboratory calibrations in Section 4.1.2.

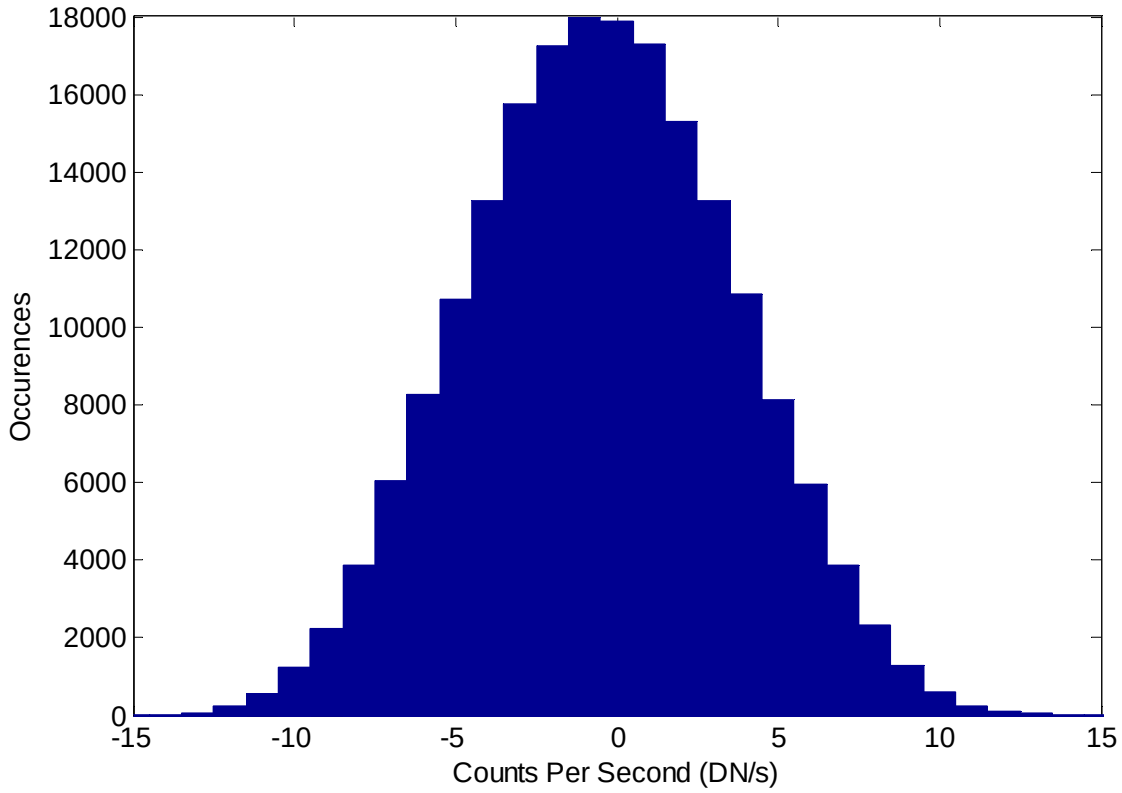

Figure 5.9: Histogram of the application of the DC offset and dark current removal method to a flight dark image at -10 °C to show performance. Counts have been normalized in exposure time to produce DN/s. Bin size is 1 DN/s.

The histogram shows how the distribution is centered near 0 DN as expected which verifies both the dark current removal process and the DC offset removal process used for flight measurements. This histogram also shows that the error in the removal method is about +/- 5 counts per second. This error is derived from the HWHM of the distribution and is very close to the same error that was discovered for the laboratory measurement removal technique.

5.2 Wavelength Registration and PSF Performance

The next step of analyzing flight measurements is to use the balloon measurements to evaluate the performance of the wavelength registration and PSF. This analysis will either verify the registration and PSF that were developed in the laboratory or illustrate changes due to the change of operating environment.

5.2.1 Development of the Reference Solar Spectrum

The simplest method to evaluate the performance of the wavelength registration is to apply it to balloon measurements and compare the resulting spectrum to the known solar spectrum. The solar spectrum contains many features at known wavelengths that will also appear in the scattered sunlight spectra measured by the DM during the flight. These features are called Fraunhofer features which are absorption lines in the solar spectrum due to a variety of gases in the sun itself like Iron, Magnesium, and Hydrogen to name a few. The first step is to develop the known solar spectrum for comparison with the balloon measurements. The known high resolution solar spectrum is shown on the left of Figure 5.10. This spectrum is obtained from a combination of results from *Colina et al.* (1996) and *Kurucz et al.* (1984).

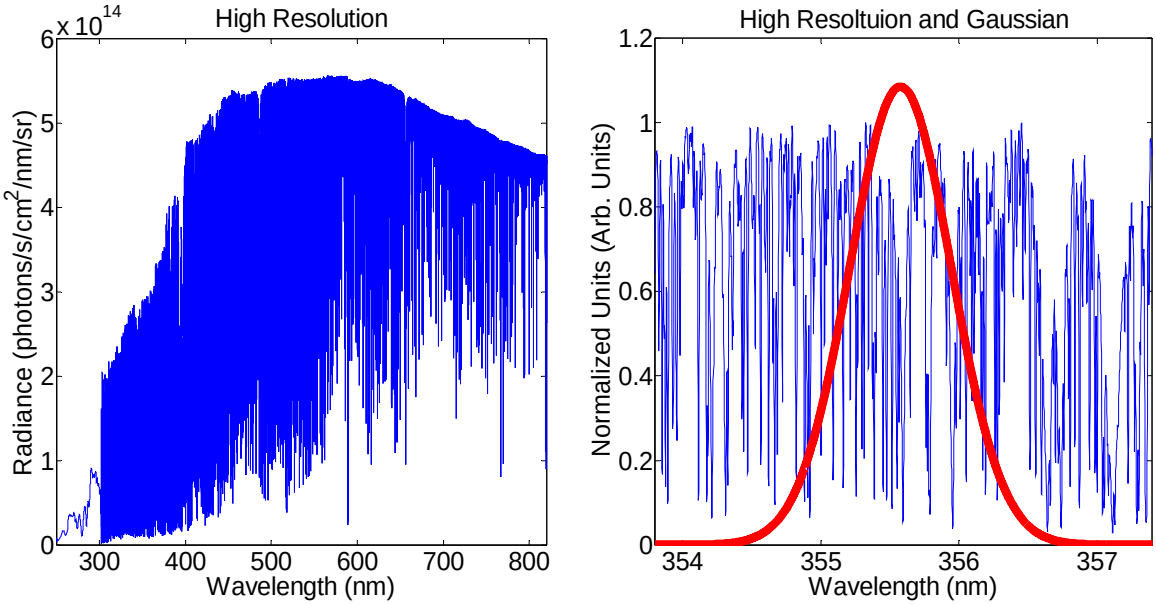

Figure 5.10: High resolution solar spectrum (left) and example of the Gaussian shape used in the weighted average of the high resolution to produce the DM resolution spectrum (DM wavelengths) on the right.

This spectrum needs to be reduced to the resolution of the DM so that the same wavelengths can be compared. This is where the PSF enters the analysis. The PSF describes the weighted average to be applied to the high resolution spectrum to produce a spectrum with the same resolution as the DM. Because of this, the performance of the PSF can be visually tested by comparing the existence and sharpness of features in the averaged solar spectrum to the measured spectrum. If both spectra have identical features, the PSF will be qualitatively verified. However, if there is a mismatch in the smoothness of the two spectra, then a too narrow or too wide PSF was used to develop the measured spectrum.

To produce a solar spectrum at DM resolution, the high resolution spectrum is used along with a Gaussian centered on the discrete DM wavelengths for each slit to calculate a weighted average of the solar spectrum. The Gaussian has a HWHM equal to the PSF for the desired slit and an integrated area of 1. The plot on the right of Figure 5.10 shows an example of the

Gaussian curve and the area of the spectrum it encompasses. Note that the solar spectrum has been normalized to 1 to be displayed on the same scale as the Gaussian. This provides a weighted average of all contributing wavelengths to each of the DM pixels and will produce a spectrum sampled at 1353 wavelengths as shown in Figure 5.11.

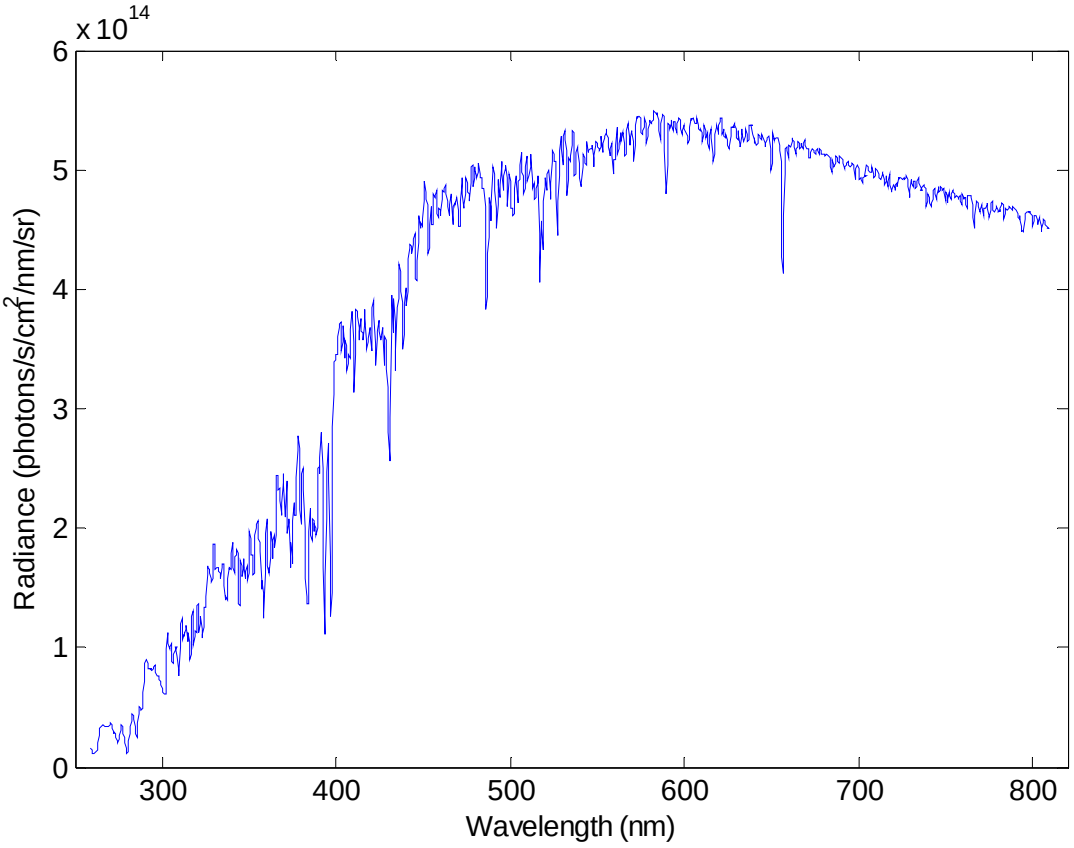

Figure 5.11: High resolution solar spectrum reduced to DM resolution.

This averaged solar spectrum is full of features that can be compared to features in the balloon spectrum to verify the wavelength registration and PSF. Two regions of the spectrum (350 – 390 nm and 635 - 675 nm) have been chosen to focus on for the verification process. These regions were chosen because they have well defined Fraunhofer features for the comparison and they are on opposite sides of the CCD.

5.2.2 Initial Comparison of Balloon Measured Spectrum to Solar Spectrum

For each wavelength range selected for comparison, it is desired to compare only the features themselves and not the overall structure of the spectrum as this requires application of the radiative transfer code as well as the relative and absolute calibrations. In order to remove the background structure, the data in these ranges are fit to a polynomial function. A quadratic fit was chosen for the 350 - 390 nm range and a linear fit was chosen for the 635 - 675 nm range based on the underlying structure in the wavelength ranges. An example of this process for the 350 - 390 nm range is shown in Figure 5.12 for a balloon measurement from the big slit. This is representative of the other slits and the solar spectrum results.

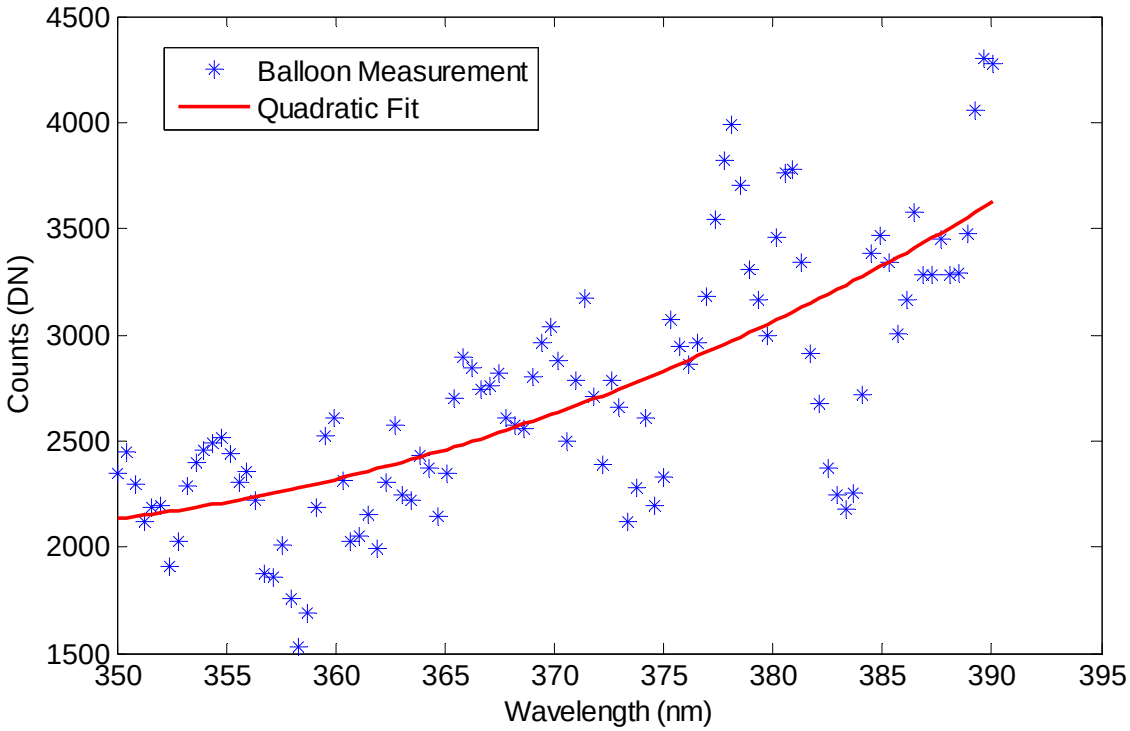

Figure 5.12: Representative plot of a big slit balloon measurement in the 350 - 390 nm range and the quadratic fit to the overall structure of the spectrum.

The quadratic fit is a good estimation of the overall structure of the spectrum which, when removed from the measurement points, leaves only the features desired for comparison. The

results for the same process for the 635 – 675 nm range are shown in Figure 5.13, again for a measurement from the big slit. As with the quadratic fit, the linear fit appears to be a good representation of the background structure which can be removed to leave the desired features.

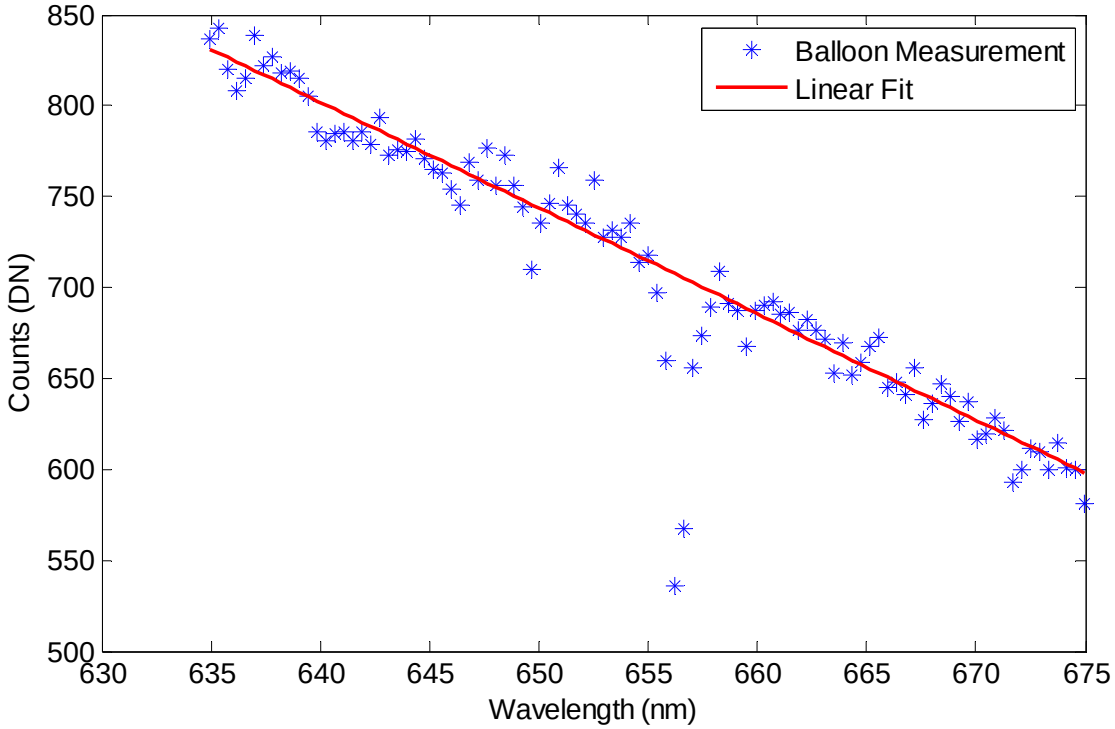

Figure 5.13: Representative plot of a big slit balloon measurement from 635 – 675 nm and the linear fit to model the overall structure of the spectrum.

The next step is to remove the background structure from all of the data sets and normalize to a common wavelength in each range. Then, the corrected balloon measurement and the corrected solar spectrum can be plotted together for comparison in each range. The comparison plots for each range are shown in Figures 5.14 and 5.15. Again, these plots show the results for the big slit only as the other slits exhibit the same trend. The first noticeable characteristic of Figures 5.14 and 5.15 is that the features in the balloon and solar spectra look similar but are offset in wavelength. This suggests that the operating conditions during flight

caused a shift in the wavelength registration that needs to be corrected. The second noticeable characteristic is that all of the features in both spectra appear to be the same in width and relative intensity. This characteristic is the same for the middle and small slit which is a validation of the PSF developed in lab.

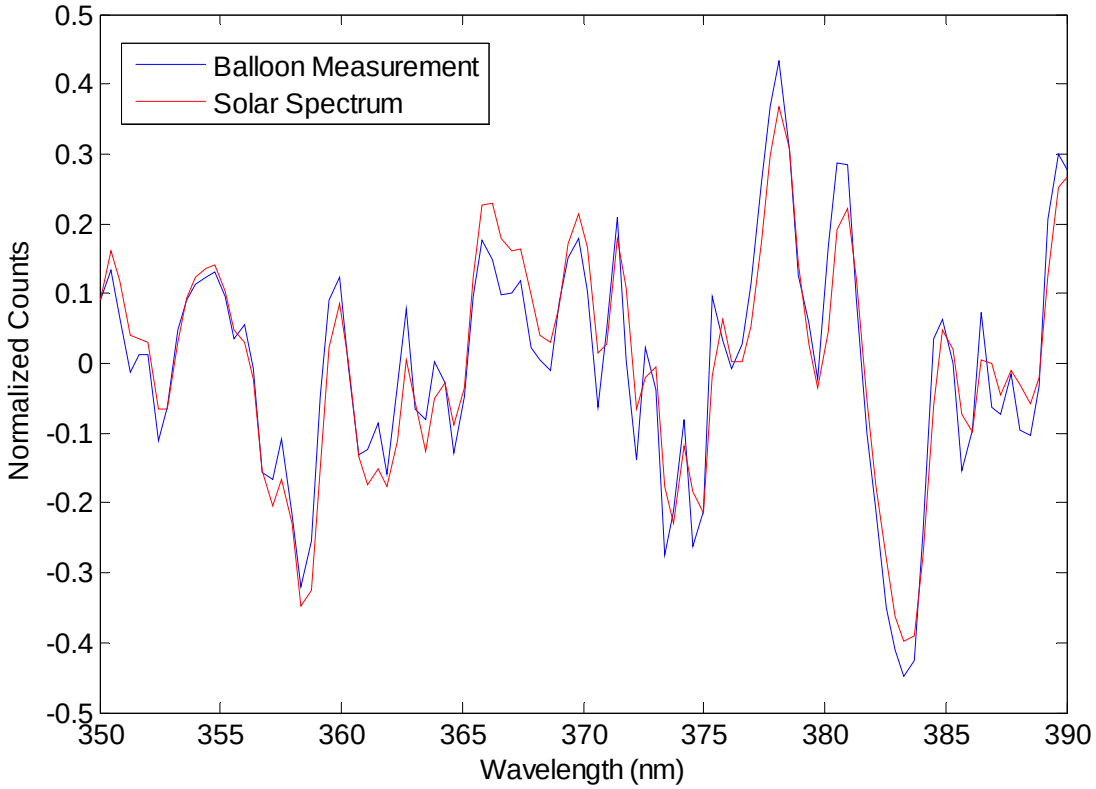

Figure 5.14: Comparison of balloon measurement features to solar spectrum features 350 – 390 nm. Features shown are normalized at 350 nm and then have the background structure removed.

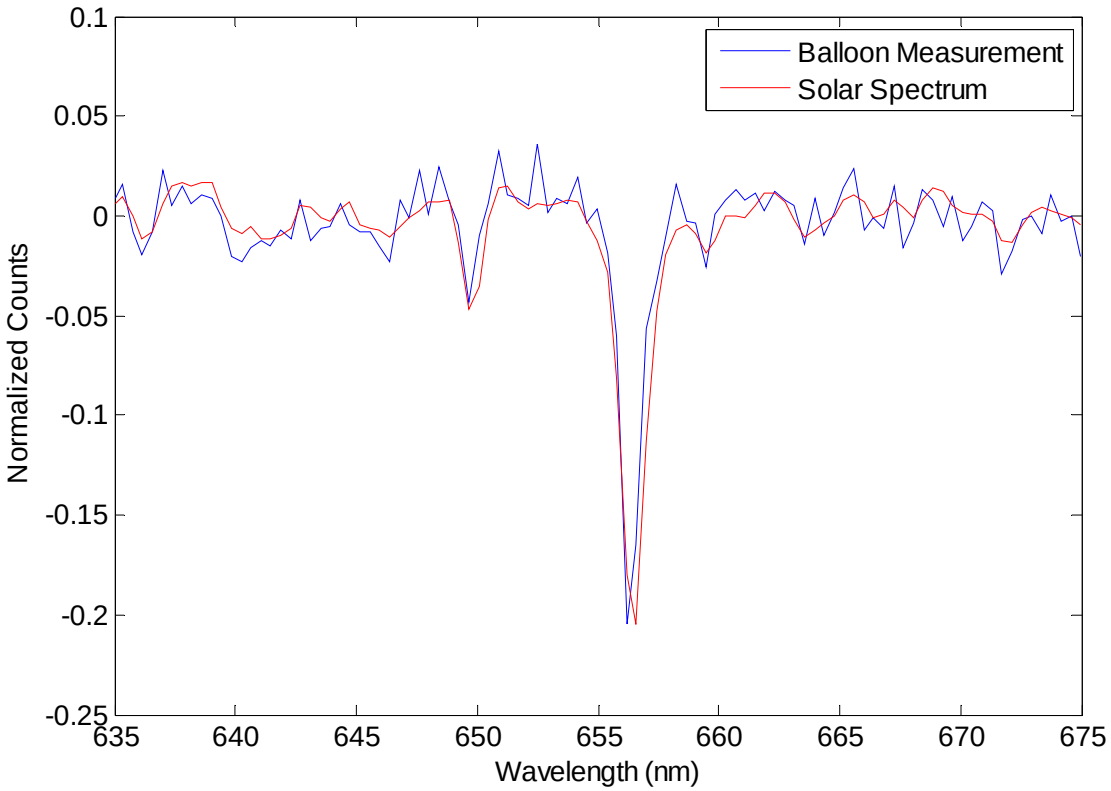

Figure 5.15: Comparison of balloon measurement features to solar spectrum Fraunhofer features 635 – 675 nm. Features shown are normalized at 635 nm and then have the background structure removed.

5.2.3 Wavelength Shift Technique and Results

Due to the apparent offset of the balloon spectrum from the known solar spectrum, a wavelength shift correction must be applied to the flight registration. This offset shows up in the middle and small slit as well but at different magnitudes. Therefore, each slit needs to be treated, and corrected, individually. To perform a wavelength correction shift, the data sets shown in Figures 5.14 and 5.15 will be reused. The implemented method is to take the balloon measurement and apply a small wavelength shift to it. Then, the difference between the two spectra will be measured using the least squares difference technique. This method will be repeated over a range of shift values which will continually shift the wavelength registration to larger values. If the range is sufficiently large, a plot of the least squares difference versus applied shift will produce

a curve that will allow a minimum value to be determined for each range. Figure 5.16 shows the result of this curve for both wavelength ranges being evaluated.

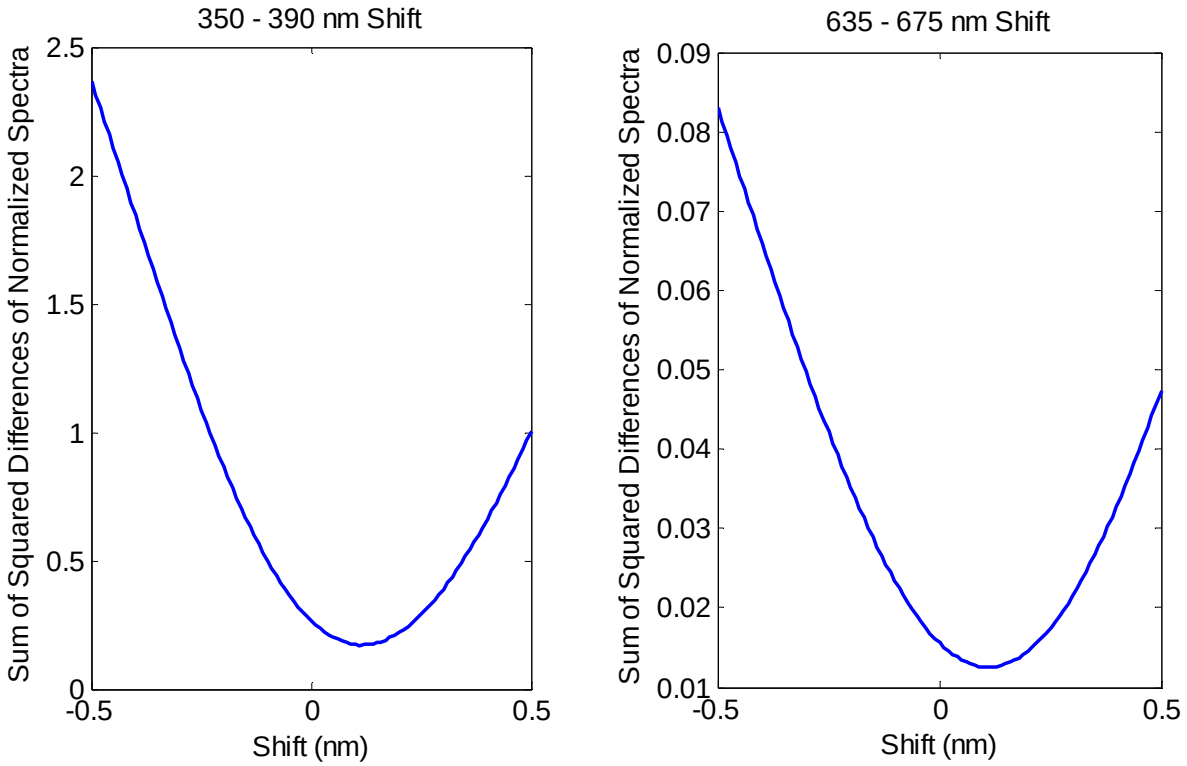

Figure 5.16: Wavelength shift analysis parabolas for the big slit. Left is the shift for 350 – 390 nm and right is the shift for 635 – 675 nm.

This produces two shift correction values; one for each range. A linear interpolation between these two points will be made across all 1353 pixels to provide a pixel by pixel wavelength correction. To achieve this, the shift values found are applied at the center of each wavelength region i.e. at 370 nm and 655 nm. This process is done for each slit and the results for all three are shown in Figure 5.17.

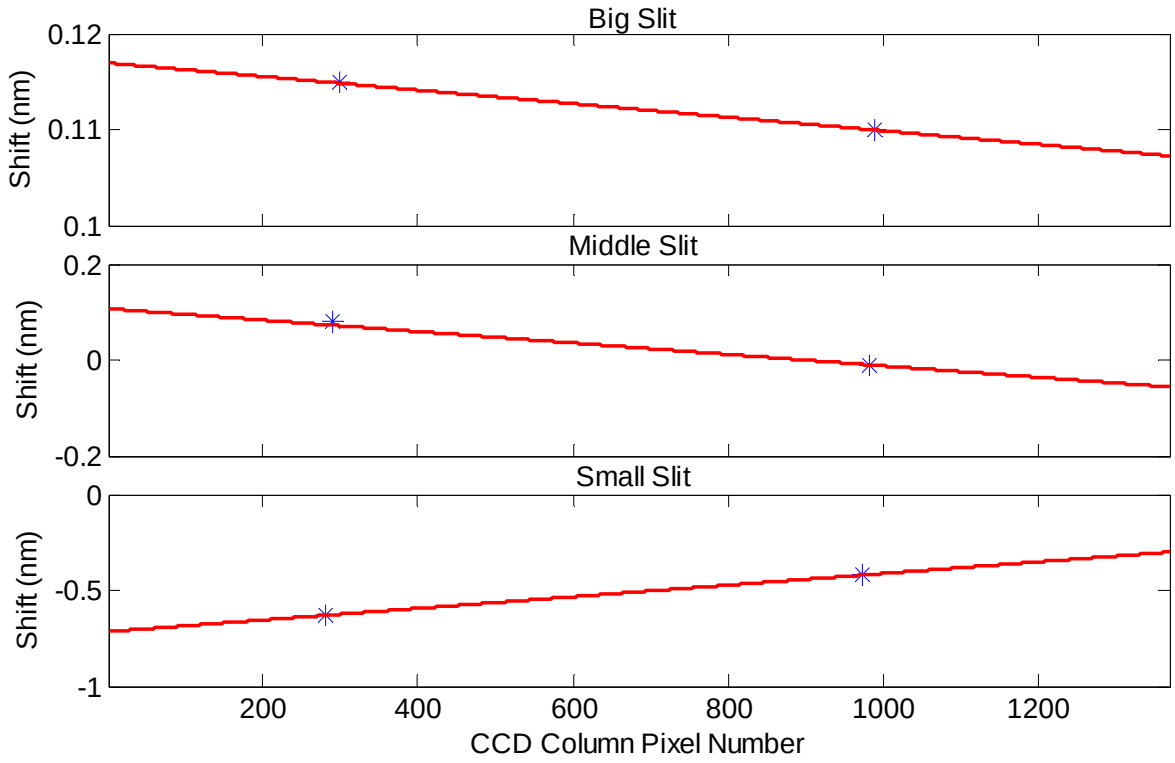

Figure 5.17: Wavelength shifts for each slit as a result of comparison with the solar spectrum data. In all plots, the blue points are the measured shifts for each range and the red line is the linear fit across all pixels.

The wavelength corrections shown can be added to the wavelength registration of each slit to produce a final set of 1353 wavelengths that the DM measures during flight.

5.2.4 Final Comparison of Balloon Measured Spectrum to Solar Spectrum

With the wavelength shift correction applied to the balloon measurements, a comparison of the balloon spectrum to the solar spectrum in the same wavelength ranges is shown in Figures 5.18 and 5.19. These plots illustrate the good performance of the final wavelength registration. As can be seen from these two figures, the features in both spectra are in better agreement with the wavelength shift applied. With the wavelength correction applied, these figures make it easier to see how well the features in the two spectra correspond to each other in structure and relative size. This serves as a further qualitative verification of the PSF.

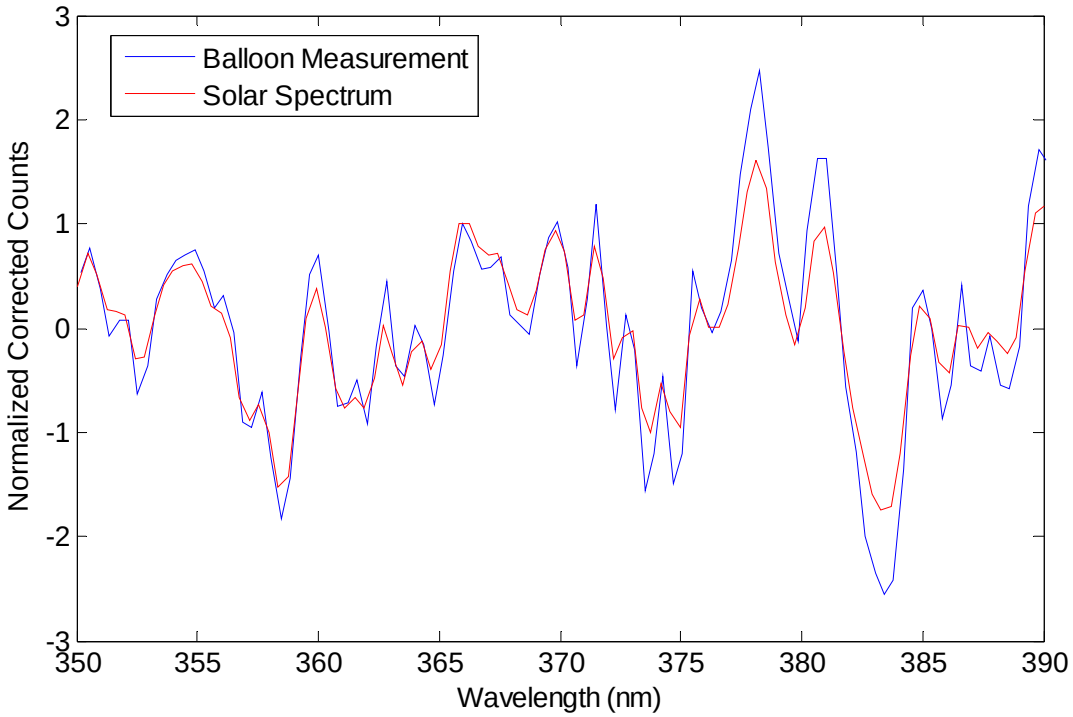

Figure 5.18: Comparison of normalized balloon features to normalized reference solar spectrum features between 350 – 390 nm after the wavelength shift has been implemented on the wavelength registration.

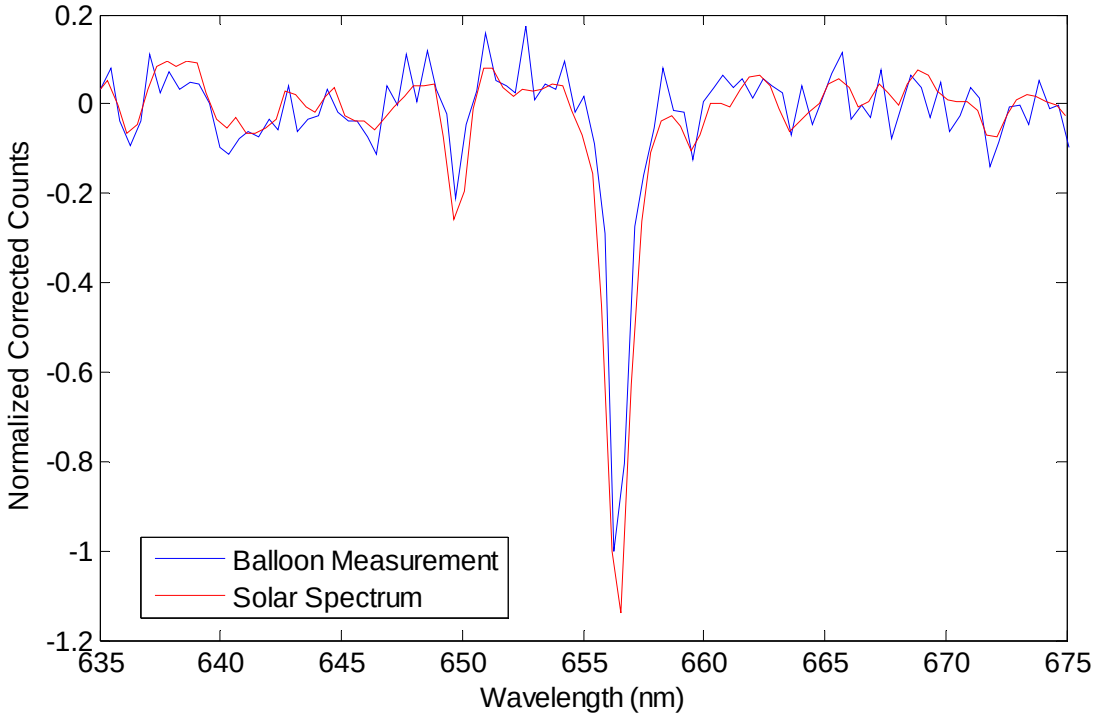

Figure 5.19: Comparison of normalized balloon features to normalized reference solar spectrum features between 635 – 675 nm after the wavelength shift has been implemented on the wavelength registration.

5.2.5 Verification of Shifted Wavelength with A-Band Comparison

The previous comparisons were limited to comparing the balloon measurement to the solar spectrum features. However, there is another set of features in the balloon measurement that can also be used for evaluating the wavelength registration performance. These features are atmospheric features and the feature that will be focused on for this verification is the O_2 absorption feature beginning at 759.37 nm more commonly known as the A-band (*Curico et al.*, 1964). The goal of this verification will be to compare the measured A-band to a scaled A-band absorption cross section to verify the corrected wavelength registration for flight measurements.

As before, the first step is to obtain a reference of the known feature, in this case, the A-band. The process starts with a high resolution model of the absorption cross section of the A-band obtained from HITRAN (*Rothman et al.*, 2009) shown in the left hand plot of Figure 5.20.

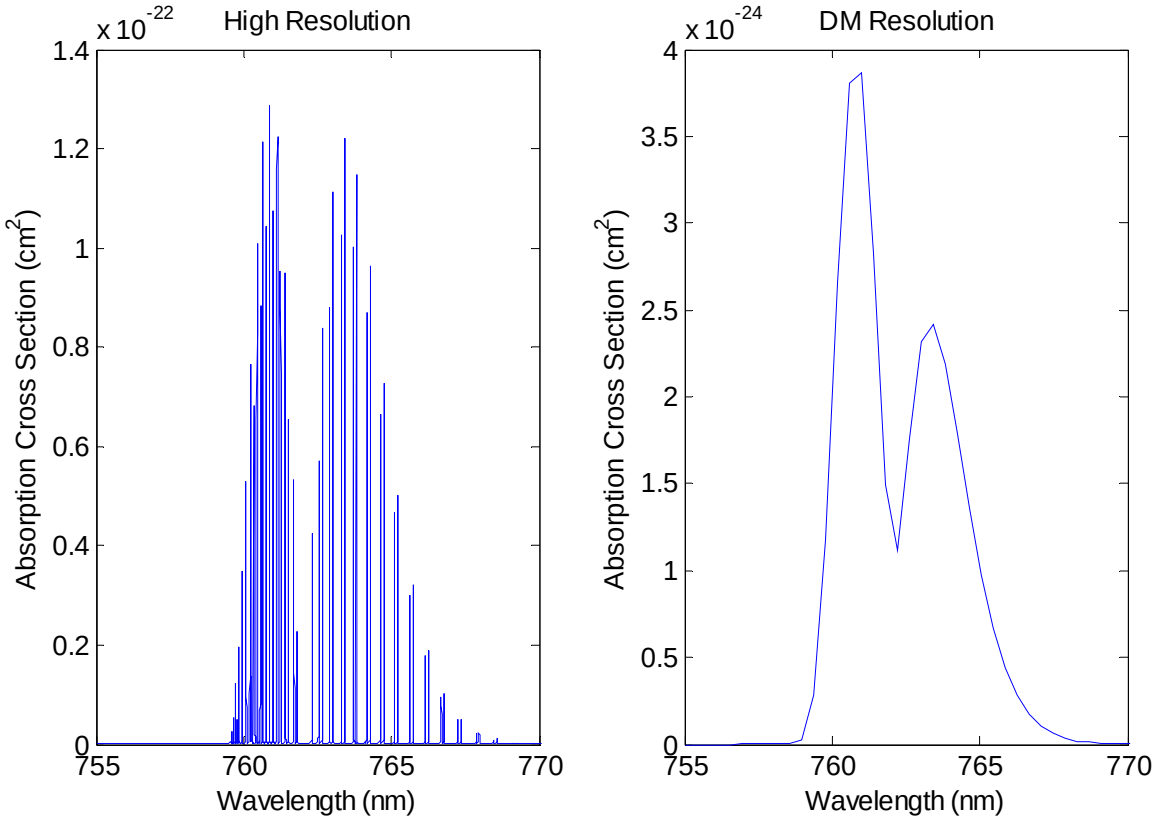

Figure 5.20: High resolution A-band absorption cross section (left) and the averaged absorption cross section at DM resolution (right).

As with the high resolution solar spectrum, the high resolution absorption cross section needs to be averaged with a Gaussian whose width is defined by the PSF and centered at DM pixel wavelengths. The averaged absorption cross section is shown in the right hand plot of right 5.20.

In order to produce a model of the A-band feature, the absorption cross section (σ) is used along with number density (n) to calculate the optical depth (τ) by integrating over all path lengths (s) as shown in Equation 5.1.

$$\tau = \int_0^s n\sigma \, ds \tag{5.1}$$

Once the optical depth is found, the A-band feature intensity (I) is modelled as:

$$I = I_0 e^{-\tau} \tag{5.2}$$

where I_0 is the original incoming intensity. Due to the fact that only the spectral structure of the A-band needs to be modelled, exact radiance values do not need to be calculated. Therefore, Equation 5.1 can have the integral removed and the number density and path length approximated as a constant value to determine the optical depth. With a value for the optical depth, the A-band feature can be modelled and normalized to produce a reference spectrum. This reference spectrum is plotted along with the balloon A-band feature measurement from the big slit as a representative plot for the other slits in Figure 5.21. In order to produce the balloon A-band feature, the same technique as in Section 5.2.1 is used where the background structure of the spectrum is modelled as a linear function and subtracted from the measured spectrum to produce only the A-band feature. The balloon measurement and the scaled A-band have both been normalized to illustrate feature position agreement. As can be seen, the A-band feature in both data sets line up with each other in terms of wavelength positioning as expected. This is especially true for the first valley and peak of the data sets. The second valley or minimum does not agree quite as well in terms of wavelength as this valley is off by one pixel in comparing the

two features but this small discrepancy is well within the noise. The fact that the two spectra have different shapes in terms of valley depth and feature widths is irrelevant for the purpose of this verification as only the wavelength positioning of the features was desired. Therefore, this plot serves as verification of the corrected wavelength registration.

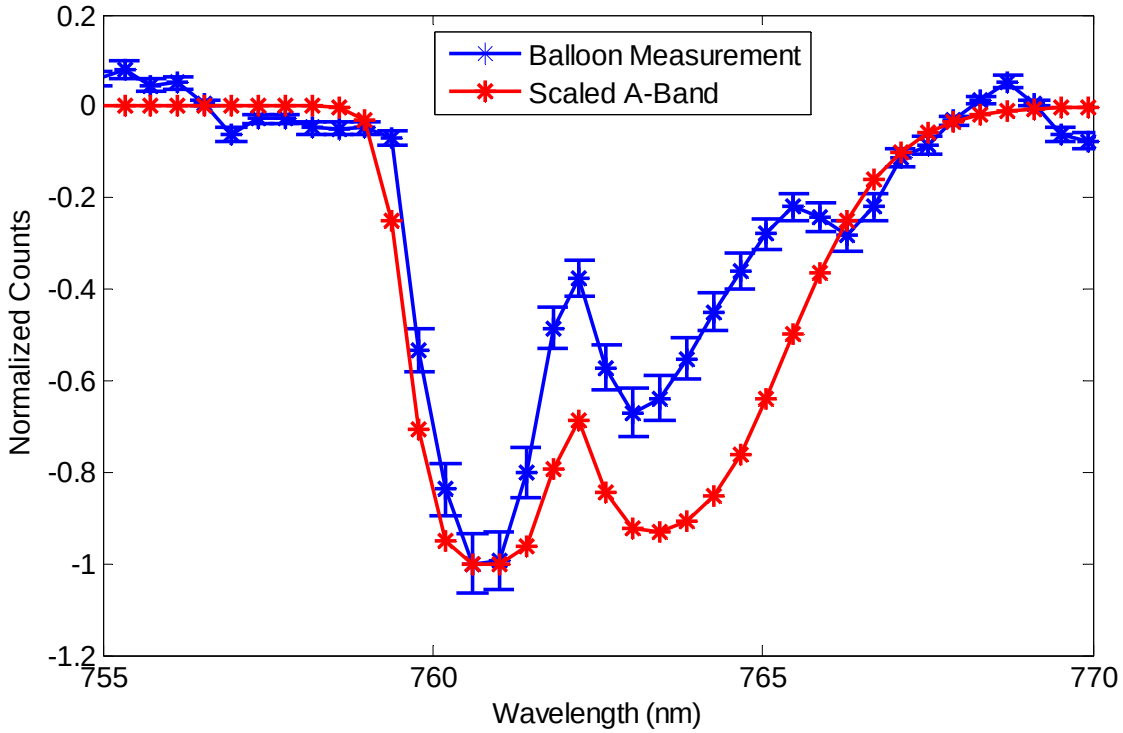

Figure 5.21: Comparison of A-band feature from balloon measurement with scaled A-band absorption cross section data.

5.3 Relative Calibration Performance

The relative calibration of the instrument is evaluated by comparing calibrated balloon flight measurements to simulated spectra calculated with SASKTRAN. Both the measured spectrum and the SASKTRAN spectrum are normalized to the same wavelength. One full limb scan during mid-morning at a stable float altitude was selected for this analysis. Figure 5.22 shows a comparison of the calibrated flight measurement to the corresponding SASKTRAN simulation

with both spectra normalized at 400 nm. This comparison serves as a representative comparison for all slits and images examined as they all yielded similar results.

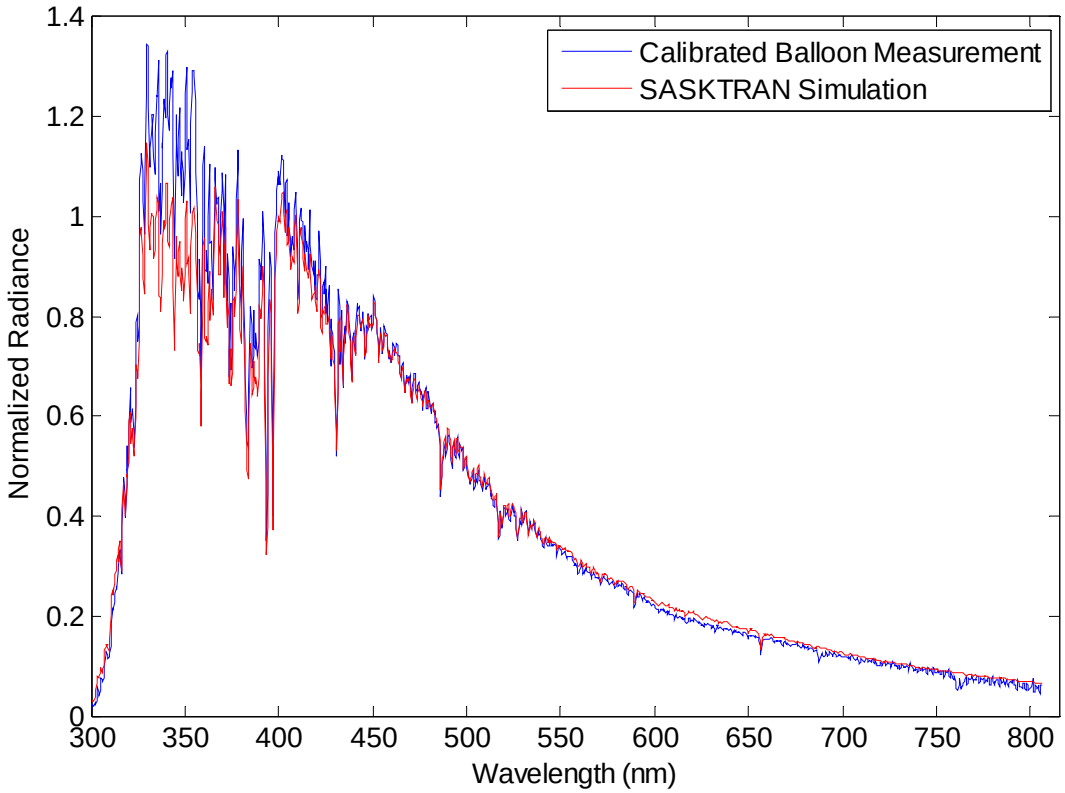

Figure 5.22: Relatively calibrated balloon measurement for the big slit compared to SASKTRAN simulation. Both spectra are normalized at 400 nm.

The two spectra agree very well with each other. The only major difference in the two spectra is around 350 nm where the calibrated spectrum is slightly higher than the simulation. This is most likely due to over scaling of the relative curve in this region but also may be due to an underestimate in the simulation as this is a spectral region that is known to be difficult to model with the successive orders of scattering technique due to the large number of scattering events (*Lloyd et al.*, 2011).

5.4 Absolute Calibration Performance

The first step in evaluating the performance of the absolute calibration is to apply the calibration to the balloon measurements and compare the resulting spectra to SASKTRAN simulations on an absolute scale. This is shown in Figure 5.23. This figure shows a calibrated spectrum from the big slit compared with the corresponding SASKTRAN simulation. The spectra were acquired and modelled with a mirror angle of 0° which is an approximate tangent altitude of 36.5 km. The SASKTRAN model used to generate all simulated spectra only includes climatological air pressure and temperature, a climatological ozone profile, and an assumed Earth albedo of 0.3. All other atmospheric species, like aerosols, were unaccounted for in the model. These two spectra agree fairly well. The most notable difference is observed in the blue end below 450 nm with the largest difference around 350 nm as with the relative calibration comparison spectra.

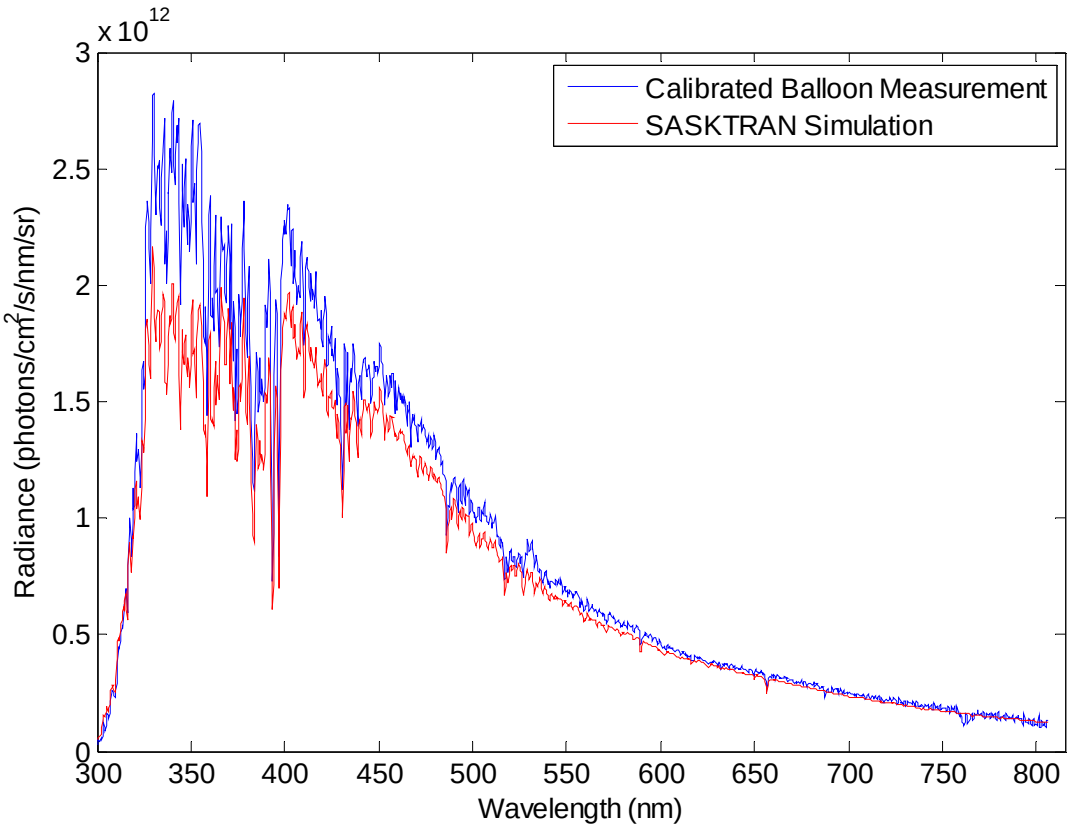

Figure 5.23: Absolutely calibrated balloon spectrum from the big slit compared to a SASKTRAN simulation at a mirror angle of 0°.

The absolute calibration is also applied to additional mirror angles, i.e. other tangent altitudes, and to the other slits. It is first applied to the big slit for mirror angles of 1.22°, 2.72°, 3.72°, and 4.72° which correspond to approximate tangent altitudes of 35.3 km, 29.5 km, 23.2 km, and 15.0 km respectively. The alignment of the mirror is such that the mirror angle defined by the system always corresponds to the angle observed by the middle slit. Therefore, with the designed vertical separation of the slits on the slit plate, which maps to an angular separation, this results in angles of 1.11°, 2.61°, 3.61°, and 4.61° for the big slit as it always views the highest point in the atmosphere of the three slits. These angles correspond to similar approximate tangent altitudes as those previously stated. The results of these comparisons are displayed in Figure 5.24.

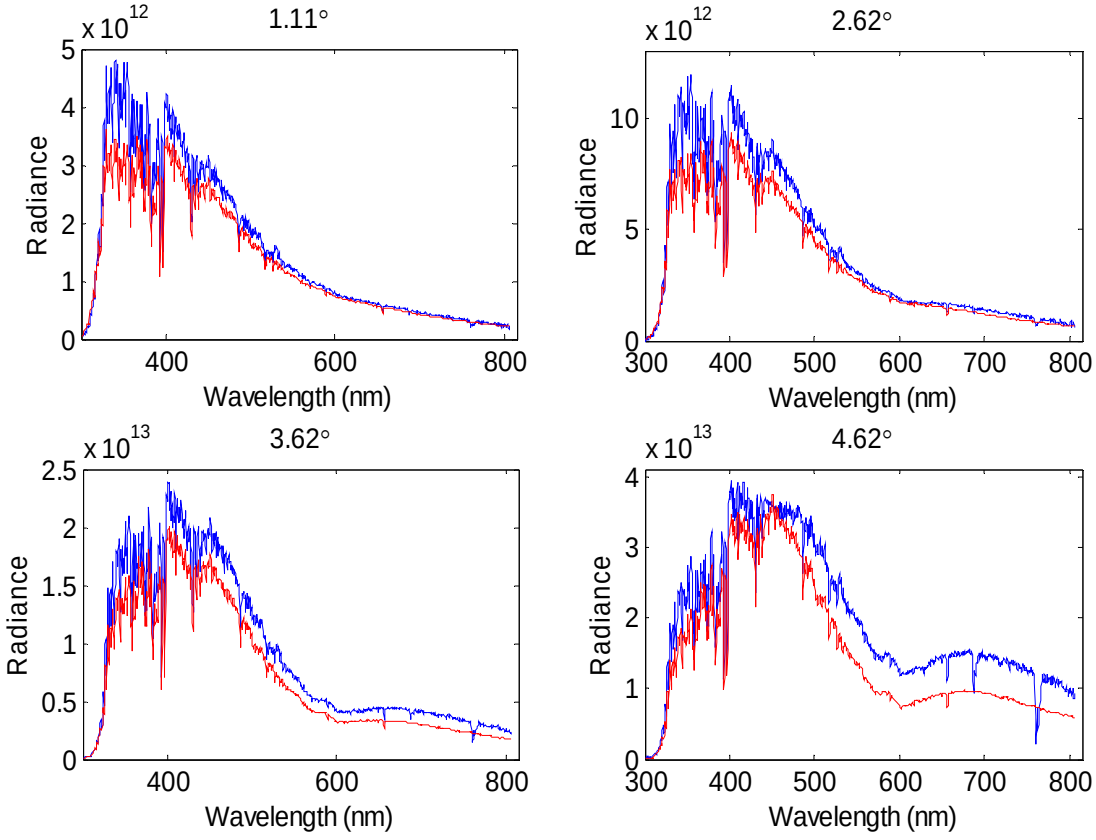

Figure 5.24: Absolutely calibrated balloon spectra from the big slit compared to SASKTRAN simulated spectrum at varying angles. In all plots, the blue line is the calibrated balloon measurement and the red line is the SASKTRAN simulation. Radiance is measured in units of [photons/s/cm^2/nm/sr].

As with the 0° comparison, the two spectra again agree fairly well although it appears that as the angle increases, i.e. that tangent altitude decreases, the agreement becomes worse. This is highlighted in the 4.62° plot where the two spectra are very different above 500 nm. This angular dependence may be due to a variety of causes. One of these potential causes is uncertainty in the SASKTRAN model at lower altitudes. This is because as the instrument looks lower in the atmosphere, the applicability of the climatological atmospheric state decreases. This is particularly due to the lack of aerosol and cloud in the model simulations. In the case of the 4.62° plot, it has been determined that the instrument was looking at a cloud top, which is the cause of the large difference between measured and modelled spectra. Other possible explanations for the overall difference in the modelled versus calibrated measurements include an angular offset of the balloon that is unaccounted for or slight changes in the optics of the system due to the cold operating temperatures. Given that the absolute calibration was performed with simple laboratory equipment as opposed to high end calibration equipment, the agreement level achieved is an acceptable result.

The absolute calibration can also be applied to the middle and small slit measurements using the equations developed in Section 4.6, specifically Section 4.6.7. The results for the middle and small slit with the mirror at 0° are shown in Figure 5.25.

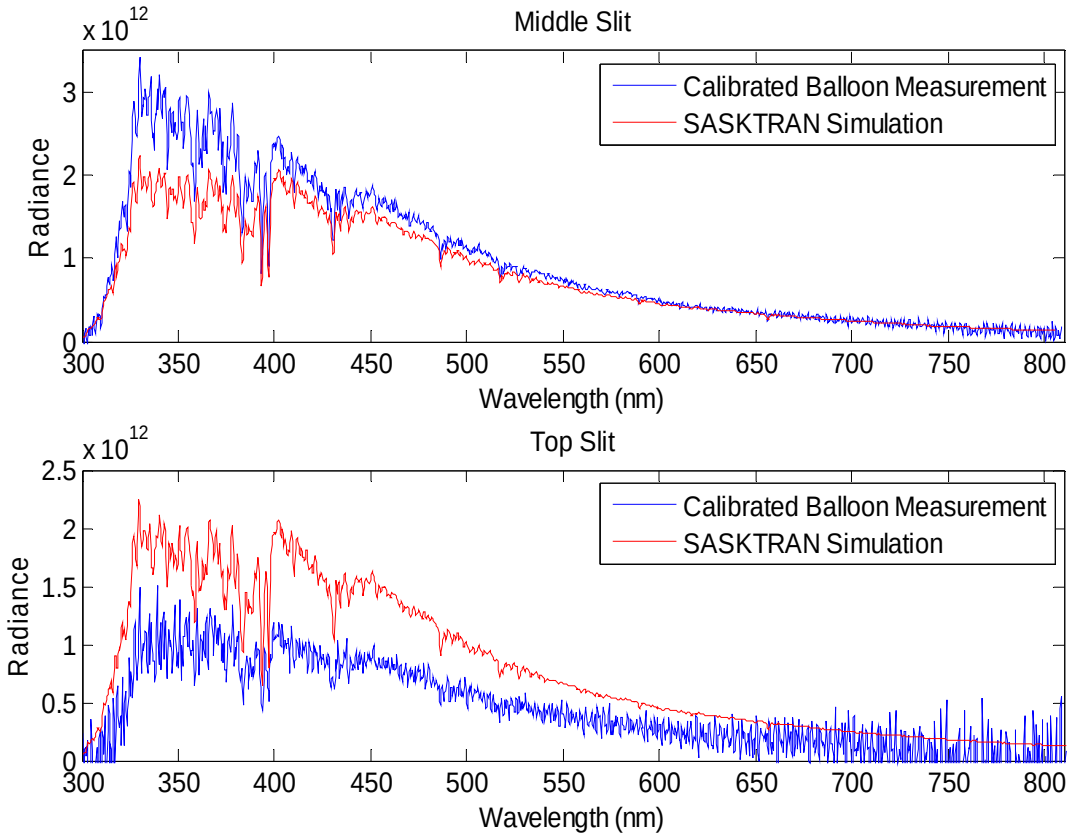

Figure 5.25: Absolutely calibrated balloon spectrum from the middle (top) and small (bottom) slits compared to a SASKTRAN simulation. All spectra are at a mirror angle of 0°. Radiance is measured in units of [photons/s/cm^2/nm/sr].

The middle slit agrees fairly well with SASKTRAN with the exception of around 350 nm as was observed in the big slit. This again may be due to an over scaling of the relative calibration in this region. The small slit does not agree as well. These measurements are very noisy due to low signal levels observed in this slit. However, the cause of the systematic low bias of the calibrated measurements remains unknown at this time. The calibrated balloon measurements for the middle and small slit can also be compared with SASKTRAN at different angles. These comparisons yield similar results to the big slit results for the middle slit, i.e. the two spectra agree fairly well for all angles but the agreement decreases with increasing angle or decreasing

tangent altitude. At the lowest tangent altitudes, the balloon measurement is higher than SASKTRAN in the red end of the spectrum due to the cloud top as was noticed in the big slit.

The results of the small slit are similar to the 0° results for the small slit. All angles for the small slit do not agree with SASKTRAN measurements and are very noisy due to low signal levels. The small slit measurements at all angles also display the systematic low bias in comparison to the SASKTRAN spectra. However, the small slit spectra do display a spectral shape that is similar to SASKTRAN and are on the same order of magnitude. The reason for the disagreement in the small slit is most likely due to the very low signal in this slit. This can be seen by the amount of noise present in these spectra. For the angles shown, the original counts in the small slit were only between 100 and 500 counts in comparison to 6000 to 10000 for the middle slit and 12000 to 15000 for the big slit. This is because the image acquisition program was designed to make sure the big slit would never saturate. This, along with the small angular separation in the atmosphere which creates only a small difference in radiance, means that the big slit will have the strongest signal and the small slit the least signal. This was a known design issue for a balloon based measurement but as the slit plate is a prototype for a satellite based measurement, the design was left as is and the consequences would be dealt with. The low signal levels in the small slit is one of these consequences. Therefore, the evaluation of the absolute calibration for the small slit is unreliable and this is accepted.

A few general trends in the calibrated measurements should be highlighted to provide confidence in the applied calibrations. First, in every slit, the magnitude of the radiance measured increases with increasing angle and thus decreasing altitude as is expected. This is due to the instrument looking lower in the atmosphere which contains a higher concentration of atmospheric species that can scatter the sunlight into the instrument. A second expected outcome

is that the middle slit always measures a slightly higher radiance than the big slit. This is illustrated in Figure 5.26 for four different mirror angles. This outcome is due to the slight angular offset of the slits and that the big slit looks higher in the atmosphere than the middle slit. This should also hold for the small slit. The small slit should actually see the highest radiance as it looks the lowest in the atmosphere. However, this is not the case. This is due to the low raw signals levels measured in this slit and is consistent with the systematic bias in the calibration results of the small slit.

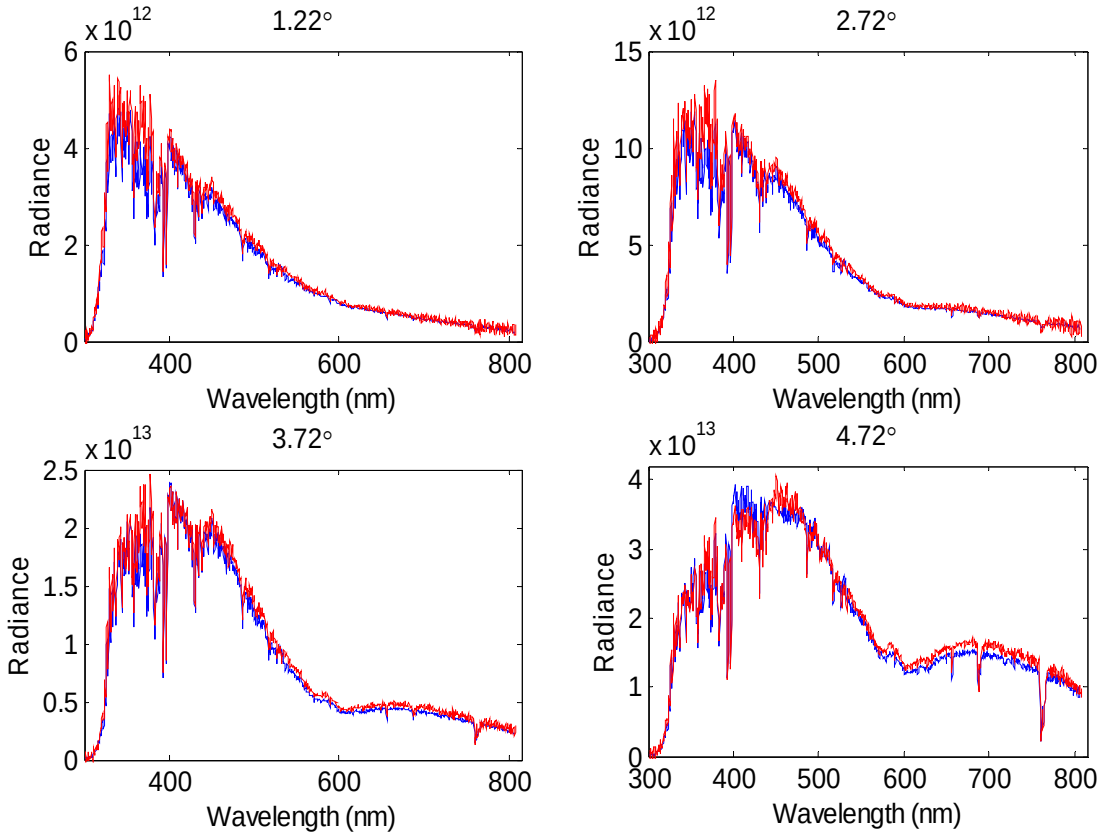

Figure 5.26: Comparison of calibrated big slit (blue line) and middle slit (red line) spectra to illustrate the slightly different radiance that each slit measures due to designed angular offset of the slits. Radiance is measured in units of [photons/s/cm^2/nm/sr].

As can be seen, the measured radiance from the middle slit (red) is consistently higher than that measured by the big slit (blue) as expected. This shows that the relative scaling between the different slits for the absolute calibration retains the expected outcome. A final verification of the relative radiance viewed by the big and middle slit can be performed by taking the ratio of the two calibrated radiances and comparing them to the ratio predicted by SASKTRAN. The average values of these ratios (big slit to middle slit) are 0.96 for calibrated flight measurements and 0.93 for SASKTRAN simulation data. These values do not match perfectly but they illustrate how close the calibration is in terms of absolute radiance observed by each slit.

CHAPTER 6
CONCLUSION

With the growing desire to produce higher quality and technologically advanced satellite instruments to study the Earth and its atmosphere, new instruments are continuously under development. These new instruments will be implemented to continue to develop our understanding of the atmosphere by providing measurements used to retrieve atmospheric species concentrations and unravel the mysteries of the atmosphere. One of these new instruments under development is CATS. This new instrument is based on the OSIRIS instrument model with some key modifications. One such modification is the addition of multiple slits to the instrument slit plate to allow multiple lines of sight to be measured simultaneously in one image. As with all new ideas and instrument modifications, this modification needed to be tested prior to use in the CATS instrument. The underlying primary goal of this work was to implement and test the multi-slit design with an essentially exact model of the OSIRIS, the OSIRIS-DM. This involved an upgrade of the DM including upgrading control electronics, installing a new slit plate and installing a new front end optical system for test flight on a stratospheric balloon. It also involved evaluation of the performance of the modified instrument in a laboratory setting in terms of calibrations and in the stratospheric balloon setting where the instrument could be used to collect atmospheric measurements for analysis.

6.1 Summary of Work

To achieve this primary goal, the original OSIRIS-DM, equipped with a single slit and connected to a laboratory computer and electronics system, needed to be upgraded to a standalone flight ready system. This involved reverse engineering of the system to enable selection of new components to be implemented in the system. These new components, primarily a new flight

computer and a series of interface electronics, then had to be configured to operate with the specific requirements of the DM. Although difficulties arose with replicating custom protocols, component operation, and interfacing of components, a new and reliable flight control system was developed to operate the DM during the balloon mission. Along with the new control system, the DM was calibrated throughout both an internal and external optical system upgrade.

The original single slit DM was first used to collect a baseline set of calibration measurements to be used for a wavelength registration and a PSF analysis. Both calibrations were very successful for a start to the calibration process. It was during this time that many of the final calibration techniques and definitions were developed. The new slit plate containing multiple slits was installed in the DM in October of 2013 at COM DEV in Ottawa, Ontario, Canada. The new multi-slit system was then used to develop a new wavelength registration and PSF for each of the three slits which again produced good results. The next step of the DM optical evolution came with the installation of the front end optical system designed and built by *Kozun* (2015). This new system consisted primarily of a front end baffle system, a scan mirror and a shutter system. The installation of this system brought the DM to a near final flight configuration. Therefore, all calibrations were performed on this system. This began with a repeat of the wavelength and PSF calibrations. Both calibrations yielded reliable results within reasonable error limits. Along with these calibrations, the relative calibration and absolute calibrations were also performed on the system. Due to a lack of high end calibration equipment available, a few manipulations were required to be implemented to complete these two calibrations. This involved the use of two different bulbs to produce enough signal at all wavelengths for the relative calibration and implementing the method developed by *Kosch et al.* (2003) for the absolute calibration. This led to the production of a relative calibration that

performed well with laboratory and ground based sky measurements. It also produced reasonably good agreement with the relative calibration of the OSIRIS-FM.

The final addition to the flight optical system came with the installation of a new aperture stop to decrease the amount of light that enters the system to allow for exposure times that could be implemented with the shutter system and not saturate the CCD. This addition required recalibration of the system for the wavelength registration and the PSF. The resulting calibrations again produced positive results. The relative calibration was unaffected by the aperture stop and thus was not required to be repeated. The absolute calibration required two final correction ratios to be applied; one due to the aperture stop and one due to the mirror that was unaccounted for in the original calibration. The correction for the aperture stop was a simple ratio of the light entering the system before the aperture stop installation to light entering the system after the aperture stop to account for the decreased charge accumulation rate observed in the CCD. The correction factor for the mirror was required due to a change in signal strength with mirror angle. Again, a simple ratio was developed in reference to a zero degree mirror angle to correct for changes in charge accumulation rates.

On September 19, 2014 at 5:36 UTC a fully operational and calibrated instrument was launched on board the Carmen gondola from the CSA balloon launch facility in Timmins, Ontario. During the ascent of the balloon, the temperature change experienced by the CCD was utilized to measure dark current generation over the temperature range at varying exposure times. These measurements were used to generate a temperature and exposure time dependent dark current calibration or removal process. These measurements were also used to verify a DC offset removal method for CCD operating temperatures below 5 °C. With the ascent completed, the balloon had reached a float altitude of approximately 36.5 km and remained around this altitude

for about nine hours. During this time, multiple images of the limb were collected and stored for later analysis. A selection of these images was analyzed to verify the developed laboratory calibrations.

The evaluation of the wavelength registration was performed by comparing Fraunhofer features in the balloon measurements to Fraunhofer features of a high resolution solar spectrum averaged to DM resolution using the developed PSF. The initial comparisons were implemented in two regions: 350 – 390 nm and 635 – 675 nm. These comparisons revealed a slight wavelength shift in each range that was most likely due to a shift in optical components due to the change in operating temperature. The shift was determined in each slit and a correction factored was applied to the registration. This new registration produced good agreement within the selected ranges. A final verification of the corrected registration was performed with comparison of the balloon measurement A-band feature to a scaled A-band scattering cross section feature. This measured feature corresponded very well with the modelled feature to provide a final verification of the wavelength registration.

The PSF was evaluated using the same measurements as were used for the wavelength registration evaluation. The measured balloon Fraunhofer features were compared with the solar spectrum Fraunhofer features averaged to the DM wavelengths with the PSF. The measured features agreed very well with the modelled features in terms of shape and relative intensities. This provided a verification of the PSF.

The performance of the relative calibration was evaluated by comparing a calibrated balloon measurement normalized at 400 nm to a SASKTRAN simulation also normalized at 400 nm. This was performed for all three slits and all calibrated spectra agreed very well with SASKTRAN spectra. The only major disagreement was between 320 nm and 370 nm where the

calibrated measurement was consistently higher than the simulation in all data sets evaluated. This is most likely due to an over scaling of the relative calibration in this region due to low signal levels used in this region to generate the calibration. General disagreements in the spectra can be attributed to an incomplete estimate of simulation parameters as these differences are minor. Overall, this calibration performed very well in comparison with the simulated spectra.

Finally, the absolute calibration was evaluated by comparing calibrated balloon measurements with SASKTRAN simulations in terms of measured radiance. This was done for all three slits at five different mirror angles. The calibrated measurements from the big and middle slit agreed reasonably well with SASKTRAN except in the 320 nm to 370 nm range where the balloon measurement was again higher than SASKTRAN. Due to the same occurrence in the relative calibration evaluation, this difference is attributed to an over scaling of the relative calibration curve in this region. The other discrepancy in the calibrated balloon measurements is noticed with increasing mirror angles which maps to images of lower altitudes. At these altitudes, the SASKTRAN model used becomes less reliable due to incomplete assumptions of atmospheric concentrations. It was also determined that at the lowest altitudes examined, the instrument was looking at a cloud which was not included in the model. This explains the differences observed in the red end of the spectra and illustrates how inaccuracies in modelled atmospheric concentrations can alter the simulation. The measurements from the small slit did not agree with the simulation very well other than in order of magnitude. These measurements were very noisy and contained low signal in the raw measurement. Therefore, the results from this slit are considered unreliable. It is not anticipated that this will be an issue for the CATS instrument on a satellite as the increase in altitude will produce a large enough variation in the signal measured by each slit to equalize the counts recorded on the CCD in each slit. Overall, the

absolute calibration worked very well for the middle and big slits especially when considering the simple laboratory equipment available.

6.2 Conclusions

The primary conclusion that should be retained from this work is that the addition of the new slit plate with multiple slits into the system created an instrument with multiple lines of sight that could be accurately calibrated and implemented to collect measurements of atmospheric limb scattered sunlight. The calibrations performed were completed with the use of available laboratory equipment and produced accurate results for the wavelength registration, PSF, and the relative calibration. The results for the absolute calibration were not as accurate as the other calibrations but were still reasonably accurate within expectations given the available equipment. The multiple slits did not introduce any unexpected behavior, such as internal stray light, that created drastic problems in calibrating the system. The new slit plate design also allowed the collection of atmospheric measurements at three different tangent altitudes simultaneously in one image without introducing any stray light or bleeding issues that would complicate analysis of the measurements. The main issue with the design when implemented on a stratospheric balloon was that the slits were not separated enough to image altitudes far enough apart in the atmosphere to provide equally strong signal in all three imaged slits. The project was successful at illustrating that a multi-slit design can be accurately calibrated and used to collect atmospheric measurements simultaneously in multiple slits.

6.3 Future Work and Recommendations

The primary goal of this project was to demonstrate acceptable performance as a proof-of-concept for the multi-slit design of the CATS instrument. This involved being able to demonstrate that the implementation of the new slit plate design would produce an instrument that could be calibrated and used to collect atmospheric measurements in a limb scatter

geometry. This goal was achieved. However, the process performed in this work, the lessons learned, and the issues encountered may be able to be applied to the calibration of the CATS instrument in the future. The following highlights some future work and recommendations for calibration of CATS or a similar instrument.

- Although the absolute calibration method implemented worked fairly well for the big and middle slit, it is quite challenging to produce a highly accurate calibration with this method. Therefore, for the CATS calibration, it is not recommended to use this method. Instead, a higher accuracy absolute calibration procedure using proper equipment that can illuminate the entire entrance aperture and provide ample signal across the wavelength range should be used. If performed correctly, this will also eliminate the need for an independent relative calibration as both calibrations can be achieved in the same measurements and analysis if sufficient equipment is implemented.
- Although the appearance of the fringing pattern with the introduction of the smaller aperture stop did not affect calibration or analysis and although the pattern most likely existed but went unnoticed in the system before the aperture stop, a study on the cause of the fringing should be conducted. This effect should be able to be calibrated and removed from the images with enough time and resources which would produce an overall higher quality image.
- Thermal tests at lower temperatures closer to operating temperatures should be conducted to evaluate potential shifting of the optics resulting in changes to the wavelength registration and PSF.
- Perform a study to find an experimental laboratory configuration that allows the illumination of each slit individually with a broadband or spectral emission source. This

should be able to be implemented with a collimator and changing the angles of light incident on the entrance aperture. This would allow for each slit to be characterized at proper signal levels independent of other slits and any potential effects of these other slits like bleeding of over saturated slits to produce enough signal in smaller slits. Calibrations with all slits illuminated should still be performed to ensure there are no stray light or smearing issues or to find limitations on pixel bleeding. However, a method to calibrate each slit independently would drastically increase the accuracy of the calibrations performed, especially in the smaller implemented slits.

- Further analysis on balloon measurements with the aid of SASKTRAN to retrieve atmospheric particle concentrations like ozone as a further evaluation of the instrument performance with the multi-slit design.

Overall, the future work on multi-slit instruments, such as CATS, should be fairly straight forward in terms of the calibration process. The presence of multiple slits does not appear to create unresolvable issues that would prevent proper calibration of such instruments.

LIST OF REFERENCES

Bourassa, A. E., Degenstein, D. A., & Llewellyn, E. J. (2008). SASKTRAN: A spherical geometry radiative transfer code for efficient estimation of limb scattered sunlight. *Journal of Quantitative Spectroscopy and Radiative Transfer*, *109*(1), 52-73.

Bourassa, A. E., Degenstein, D. A., Randel, W. J., Zawodny, J. M., Kyrölä, E., McLinden, C. A., ... & Roth, C. Z. (2014). Trends in stratospheric ozone derived from merged SAGE II and Odin-OSIRIS satellite observations. *Atmospheric Chemistry and Physics Discussions*, *14*(6), 7113-7140.

Colina, L., Bohlin, R. C., & Castelli, F. (1996). The 0.12-2.5 micron absolute flux distribution of the Sun for comparison with solar analog stars. *The Astronomical Journal*, *112*, 307.

Degenstein, D. A., Bourassa, A. E., Roth, C. Z., & Llewellyn, E. J. (2009). Limb scatter ozone retrieval from 10 to 60 km using a multiplicative algebraic reconstruction technique. *Atmospheric Chemistry and Physics*, *9*(17), 6521-6529.

Degenstein, D. A., Llewellyn, E. J., & Lloyd, N. D. (2003). Volume emission rate tomography from a satellite platform. *Applied optics*, *42*(8), 1441-1450.

Forsythe, W. E., & Worthing, A. G. (1925). The properties of tungsten and the characteristics of tungsten lamps. *The Astrophysical Journal*, *61*, 146.

Grahn, H.T., *Introduction to Semiconductor Physics*, (World Scientific Publishing Co. Pte. Ltd., Singapore, 1999).

Harang, O., & Kosch, M. J. (2001). Absolute optical calibrations using a simple tungsten bulb: theory. In *28th Annual European Meeting on Atmospheric Studies by Optical Methods* (pp. 121-123).

Holst, G. C. (1998). *CCD arrays, cameras, and displays*. JCD publishing.

Howell, S. B. (2006). *Handbook of CCD astronomy* (Vol. 5). Cambridge University Press.

Janesick, J. R. (2001). *Scientific charge-coupled devices* (Vol. 83). SPIE press.

Kosch, M. J., Mäkinen, S., Sigernes, F., & Harang, O. (2003). Absolute optical calibration using a simple tungsten light bulb: Experiment. In *Proceedings of the 30th Annual European Meeting on Atmospheric Studies by Optical Methods*(pp. 50-54).

Kozun, M. N. (2015). Optical Pointing System for Stratospheric Balloon-Borne Multi-Slit OSIRIS-DM. Thesis for the degree of Master of Science, Department of Physics and Engineering Physics, University of Saskatchewan.

Krueger, A. J., Walter, L. S., Bhartia, P. K., Schnetzler, C. C., Krotkov, N. A., Sprod, I., & Bluth, G. J. S. (1995). Volcanic sulfur dioxide measurements from the total ozone mapping spectrometer instruments. *Journal of Geophysical Research: Atmospheres (1984–2012)*, *100*(D7), 14057-14076.

Kurucz, R. L., Furenlid, I., Brault, J., & Testerman, L. (1984). Solar Flux Atlas from 296 to 1300 nm. *National Solar Observatory Atlas, Sunspot, New Mexico: National Solar Observatory, 1984*, *1*.

Lamb, David Robert & Benyon, J. D. E. (John D. E.) (1980). *Charge-coupled devices and their applications*. McGraw-Hill, London; New York.

Llewellyn, E. J., Lloyd, N. D., Degenstein, D. A., Gattinger, R. L., Petelina, S. V., Bourassa, A. E., ... & Sjoberg, F. (2004). The OSIRIS instrument on the Odin spacecraft. *Canadian Journal of Physics*, *82*(6), 411-422.

Lide, D. R. (Ed.). (2004). *CRC handbook of chemistry and physics 85th Edition*. CRC press.

Lloyd, N. D., Bourassa, A. E., & Degenstein, D. A. (2011, December). Modelling the Limb Radiance Measured by Odin-OSIRIS at 350 nm with SASKTRAN and a Simplified Tropospheric Aerosol Contribution. In *AGU Fall Meeting Abstracts* (Vol. 1, p. 0087).

McCormick, M. P., Zawodny, J. M., Veiga, R. E., Larsen, J. C., & Wang, P. H. (1989). An overview of SAGE I and II ozone measurements. *Planetary and Space Science*, *37*(12), 1567-1586.

Murtagh, D., Frisk, U., Merino, F., Ridal, M., Jonsson, A., Stegman, J., ... & Oikarinen, L. (2002). An overview of the Odin atmospheric mission. *Canadian Journal of Physics*, *80*(4), 309-319.

Nett, H., Frerick, J., Paulsen, T., & Levrini, G. (2001). The atmospheric instruments and their applications: GOMOS, MIPAS and SCIAMACHY. *ESA bulletin*, *106*, 77-87.

Rothman, L. S., Gordon, I. E., Barbe, A., Benner, D. C., Bernath, P. F., Birk, M., ... & Vander Auwera, J. (2009). The HITRAN 2008 molecular spectroscopic database. *Journal of Quantitative Spectroscopy and Radiative Transfer*, *110*(9), 533-572.

SAGE 3 on ISS. (n.d.). Retrieved November 24, 2014, from http://sage.nasa.gov/SAGE3ISS/

Sioris, C., Piekutowski, T., Nilssen, C., Degenstein, D., Murtagh, D., Solheim, B., … & Adamovic, M. (2014 Sept 23 – Oct 3). *The Atmospheric Limb Sounding Satellite (ALISS)*. Paper presented at the 65th International Astronautical Congress, Toronto, Canada.

Solomon, S. (1999). Stratospheric ozone depletion: A review of concepts and history. *Reviews of Geophysics*, *37*(3), 275-316.

Stoicescu, M. B. (2006). Development and characterization of the OSIRIS USASK observatory. Thesis for the degree of Master of Science, Department of Physics and Engineering Physics, University of Saskatchewan.

Thomason, L. W., & Taha, G. (2003). SAGE III aerosol extinction measurements: Initial results. *Geophysical research letters*, *30*(12).

Warshaw, G., Desaulniers, D. L., & Degenstein, D. (1996). Optical design and performance of the Odin UV/visible spectrograph and infrared imager instrument.

Wilcox, B. A. (2002). Ground validation of OSIRIS scattered sunlight measurements. Thesis for the degree of Master of Science, Department of Physics and Engineering Physics, University of Saskatchewan.

APPENDIX A
FLIGHT SOFTWARE DESIGN AND SIGNAL FLOW

The entire communication chain and software design from the Ocelot sending commands to the Launchpad, the Launchpad sending to the ROE and the ROE sending images back to the Launchpad and the Ocelot is as follows. First, the Launchpad powers on and goes into an idle state to wait for commands to come in from the Ocelot. The Ocelot receives user defined commands entered manually or automatically with a script and sends these commands to set up the image acquisition to the Launchpad one at a time. The Launchpad echoes each command back to the Ocelot to ensure the proper command was received. While the command is being echoed back, the received command is stored on the Launchpad waiting to be sent to the DM. If Ocelot receives the proper echo, it sends the next command. If it does not, it resends the previous command and continues until all commands are sent and received properly. This sequence has a timeout counter on it that if it is exceeded will produce an error that is sent to the user and causes an automatic system reset to attempt to alleviate the problem for the next run. The last command that Ocelot sends is a start imaging command. Once the Ocelot has sent this command, it enters a receive/waiting state that will continuously receive data from the Launchpad when prompted until the Launchpad signals that there is no more data to receive. When the Launchpad receives the start command, it sends it along with all previously stored set up commands to the ROE over an SSI module and then enters a waiting state to wait for the receive FIFO to fill so it can trigger and service the DMA interrupt. When the DM receives the start imaging command, it tells the CCD to stop flushing and acquire an image. Once image acquisition is complete, the DM starts to send the data back to the Launchpad until all data is sent out. When the DMA interrupt is triggered, it transfers the data from the FIFO into the primary buffer and then puts the Launchpad back into its waiting state. When the DMA transfer occurs, it counts how many words were

received and since a full image is the same number of words every time, the Launchpad waiting state continues waiting until the counter hits its full value. Due to the fact that if even one word is missed from the DM the Launchpad will be stuck in an infinite waiting state, the retrieval of the start imaging command from the Ocelot also enables a timeout timer on the Launchpad. When the pixel counter reaches its full value, this timer is disabled. However, if the counter does not reach full value in the allotted time, the Launchpad is reset and the stop code is sent along with an error code to the Ocelot. While waiting and servicing the DMA interrupts, the Launchpad continues to receive data from the DM and send data from the filled ping pong buffers to the Ocelot. Once the proper number of words has been received from the ROE, a stop code is sent to the Ocelot which signals that an entire image was received. Finally, as the Launchpad is servicing the DMA, it calculates a running Cyclic Redundancy Check (CRC) value on the received data that it sends to the Ocelot after the stop code. After the Launchpad has sent out the entire image, the stop code, and the CRC value to the Ocelot, it clears out the communication buffers and goes back into the original idle state to wait for commands from the Ocelot. When the Ocelot receives the stop code, it checks if a timeout error code was also sent. If it was, it discards the image as it is incomplete. If it was not sent, a full image was received and so it calculates its own CRC value on the data and compares it to the received CRC value. If the values match, the image is marked as a good image and if they do not match, an error occurred somewhere in the system and the data is flagged with a CRC error. Once the data has been received and error checked, it is processed and saved in a file on a solid state hard drive. The Ocelot then goes back to the top of the program and sends commands again to the Launchpad when prompted by the user or automated program.